Influence of Material Structure on Thermoelectric Properties of Atomic Scale Systems

by

Janakiraman Balachandran

A dissertation submitted in partial fulfillment
of the requirements for the degree of
Doctor of Philosophy
(Mechanical Engineering)
in The University of Michigan
2014

Doctoral Committee:

Associate Professor Vikram Gavini, Co-Chair
Associate Professor Pramod Sangi Reddy, Co-Chair
Assistant Professor Emmanouil Kioupakis
Assistant Professor Donald Jason Siegel

To my wife Archana

&

To my son Dhruva

ACKNOWLEDGEMENTS

I would like to thank my advisors Prof.Vikram Gavini and Prof.Pramod Reddy for providing me an opportunity to come to Michigan and work on interesting problems in nanoscale transport. Their constant guidance and support has helped me to learn a lot on how to approach a new research problem. Working with them was a truly rewarding experience since it gave me a first hand knowledge of how to do good academic research.

I would like to thank Prof. Barry Dunietz of Kent State for helping me learn *ab-initio* modeling of organic systems. I would like to thank my other committee members Prof. Manos Kioupakis and Prof. Don Siegel for guiding me to think more deeply about my doctoral research. I would like to thank Prof. Krishna Garikipati for teaching me finite element modeling and guiding me in various academic and non-academic issues. More importantly I want to thank him for those great thermodynamic discussions that we had towards the end of my degree. I would like to thank Prof. Robert Blumenthal of University of Toledo for his support and mentoring during the course of my degree. I would like to thank the ever youthful Ms.Brenda Imber of English Language Institute for teaching me to give good presentations.

I would like thank my colleagues Bala, Mrinal, Woochul, Bikash and Sambit for providing me a great lab experience. I would like to thank my age old friends Karthik, Sathya and Aditya who had always been there for me. I would like to

specially thank my dear friends Phani and Shiva. They had been one of the greatest source of strength to me. Their incredible support and humor kept me going through the seemingly hopeless times. The wonderful discussions that we had over the course of my degree enabled me to gain a wide range of scientific knowledge.

I would also like to thank my parents, my brother and my in laws for their constant encouragement and support. I have to thank my cute son Dhruva who made me feel happy and special during those final grueling months of dissertation. Finally the most important of all, I'm greatly indebted to my wife Archana. Words can't express the support, encouragement and patience she showed towards me. Without her motivation and inspiration, it would have never been possible for me to have completed my degree.

TABLE OF CONTENTS

LIST OF FIGURES

Figure

LIST OF TABLES

Table

LIST OF APPENDICES

Appendix

ABSTRACT

Influence of Material Structure on Thermoelectric Properties of Atomic Scale Systems

by

Janakiraman Balachandran

Co-Chair: Vikram Gavini

Co-Chair: Pramod Sangi Reddy

Developing high efficiency ambient temperature thermoelectric devices has huge potential in transforming electronics and biomedical device industries. The efficiency of a thermoelectric device is quantified by its figure of merit ZT. The ZT value of a device in turn is determined by its material properties such as thermopower (S), electrical conductivity (σ) and thermal conductivity (k). One of the major challenges in improving the ZT values is the simultaneous maximization of thermopower and electrical conductivity – which is possible only in zero dimensional nanoscale materials with discrete energy levels. To develop thermoelectric devices employing these nanoscale materials, we need to understand the electronic transport in nanometer length scale systems which is dominated by quantum mechanical effects. Heterojunctions where atomic-scale single molecules are placed in contact with metal electrode atoms (Au in this case)—commonly referred as metal-molecule-metal heterojunctions (MMMJs) are an excellent test system to understand

the electronic transport in nanoscale systems.

In this work, we develop *ab-initio* based computational models to quantitatively predict the thermopower (S) and the injection barrier (Δ) for numerous Au/aromatic molecule based MMMJs. The predicted values match very well with the experimentally measured values. Further, when a molecule is brought into contact with Au atoms, these computational models also enable us to understand the influence of molecular structure (end-groups in particular) on the molecular energy level reorganization. Our analysis elucidates that the energy level reorganization depends on two important factors namely (i) the stabilization effect — due to the physical contact between the molecule and Au atoms, and (ii) the charge transfer effect — due to the chemical interactions between the molecule and Au atoms. In charge gaining molecules, these effects are competing with one another resulting in a small total-shift of the energy levels. However in case of charge losing molecules, these effects are complementary, resulting in a large total-shift towards lower energies. This mechanism and its influence was computationally demonstrated on various MMMJs. This mechanism provides a simple unified explanation of experimentally measured thermopower values in these heterojunctions. Finally, this mechanism also enabled us to develop very efficient computational strategies to compute the sign of the thermopower and in turn the nature of transport (p-type or n-type). This computational approach can potentially be used to analyze a very large set of MMMJs made from different molecules/metal systems to identify the heterojunctions with very high thermoelectric efficiency.

CHAPTER I

Introduction

1.1 The Energy Challenge

The ability to produce and consume energy determines the aspirations and limitations of a society. Energy is the prime mover of an economy that determines the agriculture, manufacturing and technological output from a society or a country. Today, most of the energy is produced from the conventional fossil fuels such as coal, natural gas and petroleum. The chemical energy stored in these molecules is converted into heat through the combustion process. The heat produced by this process in turn is used by thermo-mechanical devices such as turbines and IC engines to produce mechanical work. The mechanical work in turn is used to create electricity or to power transportation vehicles. As an example, United States consumed 97 quadtrillion BTUs in 2011 of which more than three-fourth of the energy came from conventional fossil fuels[(1)]. Unfortunately, the combustion process creates carbon-di-oxide (CO_2) as by-product which is a green-house gas. The current CO_2 levels are about 400ppm[(47)] — the highest ever experienced by humans. Further advanced natural gas extraction technologies like hydraulic fracturing also possess inherent dangers of leaking methane — an extremely strong green-house gas into the atmo-

sphere. These green house gases have major influences on increasing global temperature which in turn is expected to affect all major ecosystems on the earth and the livelihoods of over 3 billion people worldwide[47].

Hence the goal of the current energy research is to create adequate, affordable and sustainable energy with minimal influence on the global climactic conditions. An important research direction which can help us to reach the aforementioned objectives is to improve the efficiency of the energy conversion process. For example more than 50% of the total energy usage in USA, in 2011, was released into atmosphere as waste-heat energy. In particular, gasoline powered automobiles converts only 25% of the combusted energy into vehicle operation with the rest being rejected as waste-heat. Tapping into this waste heat and converting it into electricity can help us to improve the efficiency of the energy-conversion process and in turn reduce the greenhouse gas emissions.

1.2 Thermoelectric Device

Thermoelectric devices offer great potential in converting this waste-heat into electricity. Thermoelectricity is the process of directly converting heat into electrical energy through solid-state heat engines. Due to this direct conversion, thermoelectric devices possess no moving parts which improve the reliability of these devices. The thermoelectric effect of directly converting heat into electricity was first discovered by John Seebeck in 1823, when he observed the deflection of a compass needle when it was placed near a closed loop formed from two dissimilar metals maintained at different temperatures. The complimentary effect of converting electrical energy into temperature differentials was observed by Jean Peltier in 1834. The development of thermodynamics enabled Lord Kelvin to provide a consistent explanation to

relate the two effects observed by Seebeck and Peltier. The next big breakthrough in understanding the thermo-electric phenomena came in 1948, when Callen[12] used the Onsanger theory of non-equilibrium thermodynamics to provide a rigorous and coherent description of the thermoelectric phenomena. Abraham Ioffe in his pioneering work[33] extended this approach to relate the thermoelectric phenomena to the solid-state material properties which will be briefly described below.

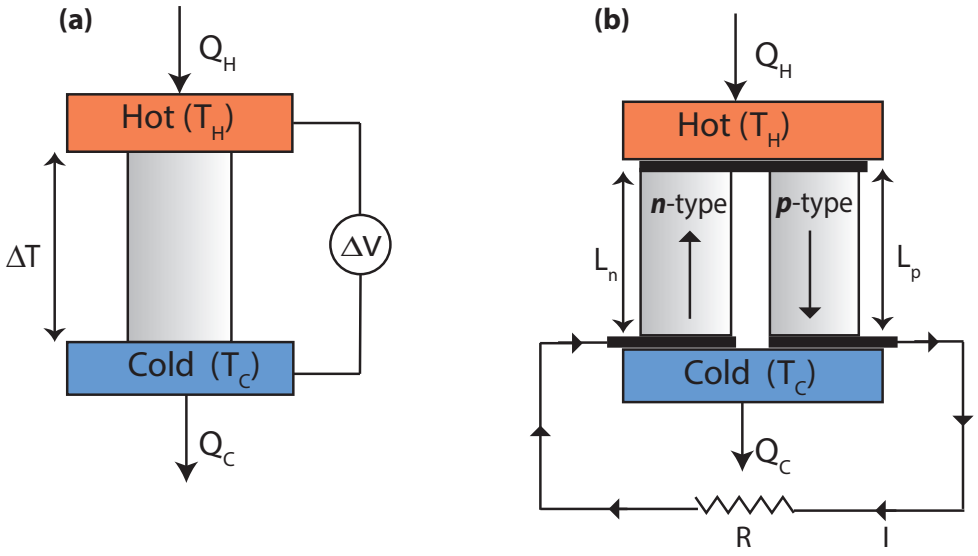

Figure 1.1: (a) Schematic picture of a thermoelectric material placed between two thermal reservoirs maintained at different temperatures. (b) Schematic picture of a thermoelectric device comprising of both p-type and n-type semiconducting materials.

Fig. 1.1(a) provides a simple schematic picture of a thermo-electric material sandwitched between two thermal reservoirs maintained at two different temperatures T_H and T_C. The input heat Q_H flows from the hotter electrode (T_H) to the thermoelectric material and the output heat Q_C flows from the thermoelectric mate-

rial to the colder electrode (T_C). This heat flow in turn creates an electric field ($\boldsymbol{E}$). The $\boldsymbol{E}$ is related to the temperature differential (∇T) through the thermopower (S) as

$$\boldsymbol{E} = S \cdot \nabla T \ .$$

Within the approximation of linearly varying temperature field and electric field, we can rewrite thermopower as

$$S = -\frac{\Delta V}{\Delta T} \ ,$$

where ΔV is the open-circuit voltage observed in the external circuit.

1.2.1 Efficiency of Thermoelectric device (η)

Understanding the efficiency of the thermo-electric device and relating it to material properties is very important to design and create new materials with high efficiency. In this section we follow Refs.[60,57] to relate the efficiency of a thermoelectric device to its material properties. The schematic picture of an actual thermoelectric device that converts the heat into electrical energy is given in Figure 1.1(b). It consists of a p-type and n-type semiconductor element sandwitched between hot and cold reservoirs. The heat-flow generates a voltage differential with opposite signs in the p-type and n-type semiconductors. As a result, the electrical current flows from hotter to colder electrode in the p-type semiconductor, while it flows from the colder to hotter electrode in the n-type semiconductor. This opposing direction of current-flow results in the semiconductor elements to be electrically connected in series although the heat flow between them is in parallel. The generated current flows through the external circuit to create the output power.

The conversion efficiency of the device is given by the ratio of the output electrical energy (W) to the input heat (Q_H) supplied.

$$\eta = \frac{W}{Q_H} \tag{1.1}$$

The input heat Q_H supplied from the hot reservoir to the thermo-electric device can be expressed in terms of the reservoir temperatures and material properties as[57,60]

$$Q_H = (S_p - S_n)\, IT_H + K_{eff}\,(T_H - T_C) - \frac{1}{2} I^2 R_{eff} \tag{1.2}$$

where I is the current S_p and S_n are the thermopowers of the p-type and n-type thermoelectric materials respectively. T_H and T_c are the temperature of the hot and cold sources respectively. K_{eff} and R_{eff} are the effective thermal conductance and electrical resistance given by

$$\begin{aligned} K_{eff} &= \frac{k_p A_p}{L_p} + \frac{k_n A_n}{L_n} \\ R_{eff} &= \frac{L_p}{\sigma_p A_p} + \frac{L_n}{\sigma_n A_n} \end{aligned} \tag{1.3}$$

where k and σ are the thermal and electrical conductivity respectively. A is the area of cross section and L is the height. The output electrical energy W is given by

$$W = I^2 R \tag{1.4}$$

Substituting W and Q_H in the efficiency equation we get

$$\eta = \frac{W}{Q_H} = \frac{I^2 R}{(S_p - S_n)\, IT_H + K_{eff}\,(T_H - T_C) - \frac{1}{2} I^2 R_{eff}} \tag{1.5}$$

We can show that the device efficiency is maximized when the external load resistance R matches the internal effective resistance R_{eff}. Employing this relationship we can simplify the device efficiency as

$$\eta = \frac{\left(\sqrt{(1+ZT_m)}-1\right)}{\left(\sqrt{(1+ZT_m)}+T_c/T_H\right)} \underbrace{\frac{T_H - T_C}{T_H}}_{\text{Carnot Efficiency}} \tag{1.6}$$

where T_m is the mean temperature of the reservoirs

$$T_m = \frac{T_H + T_c}{2}$$

where Z is given by

$$Z = \frac{(S_p - S_n)^2}{\left(\sqrt{\frac{k_p}{\sigma_p}} + \sqrt{\frac{k_n}{\sigma_n}}\right)^2} \tag{1.7}$$

Z has the units of K^{-1}. Z can be non-dimensionalized by multiplying T_m to create figure of merit ZT_m. The efficiency of any thermodynamical system is limited by Carnot efficiency. As observed from the equation 1.6, the efficiency of the system increases monotonically as a function of ZT_m to reach towards Carnot efficiency. It can be shown that for normal operating conditions, we will need $ZT_m \geq 3$ to have 30% efficiency of Carnot cycle at which point the thermo-electric devices can compete with the traditional thermo-mechanical energy conversion systems[75].

The ZT_m of the total device depends directly on the figure of merit ZT of the individual p and n-type elements which is given by

$$ZT = \frac{S^2\sigma}{k}T \tag{1.8}$$

The numerator of the equation $S^2\sigma$ is commonly referred to as the power factor of the material. For a given operating temperature region, the ZT value of a material can be maximized by increasing the power factor or decreasing the thermal conductivity.

1.3 Figure of Merit (ZT) and Material Properties

1.3.1 Maximizing the Power Factor $\left(S^2\sigma\right)$

Metals are a poor choice to be used as thermoelectric elements since they have high electrical and thermal conductivity. Further in metals, we cannot systematically control and modify the electrical and thermal conductivity independently. Semiconductors provide us better ability to independently control its material properties. The semiconductors possess low electrical and thermal conductivity. The electrical conductivity of these material can be systematically improved through doping or alloying. In a typical bulk semiconductor, doping increases the career concentration (n) which in turn increases the electrical conductivity (σ), since the σ is related to n as

$$\sigma = ne\mu \tag{1.9}$$

where e is the elementary charge of the career and μ is the career mobility. Interestingly what we observe for a typical semiconductor is that doping increases the electrical conductivity whereas it decreases the thermopower of the material. Hence there is an optimal level of career concentration until which the power factor $\left(S^2\sigma\right)$ increases as shown in Figure 1.2(a)[60]. Beyond this point, the thermopower falls much more rapidly compared to the increase in σ which results in a decreased power-factor of the material.

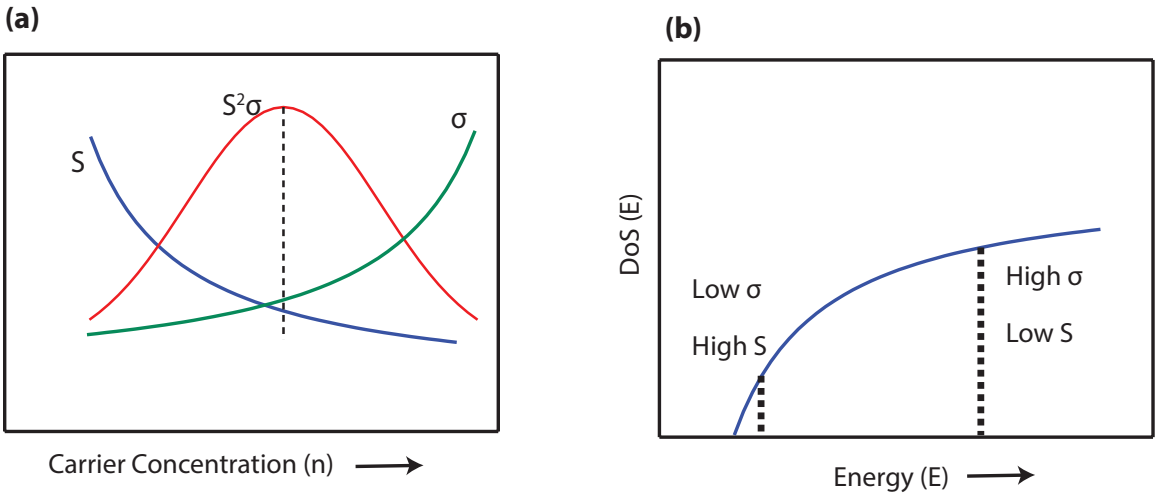

Figure 1.2: Figures adapted from Ref.[60] (a) Thermopower (S), electrical conductivity (σ) and power factor $(S^2\sigma)$ as a function of carrier concentration (n). (b) Electrical conductivity (σ) and thermopower (S) values are determined by the DoS and its derivative respectively.

The decrease in thermopower with increasing career concentration can be understood from the Mott equation which relates the thermopower (S) and electrical conductivity (σ) as

$$S = \frac{\pi^2 k^2 T}{3e} \frac{\partial \ln \sigma}{\partial E}\bigg|_{E=E_F}. \tag{1.10}$$

From this equation, we can observe that S is directly proportional to the derivative of σ with respect to the energy at the Fermi energy (E_F). This in turn is directly proportional to the derivative of density of states (DoS) near E_F. For a semiconductor with very little doping the E_F (or chemical potential) is very close to the band edge where the DoS is very small (resulting in a small σ) although the derivative of the DoS is large resulting in a large thermopower. As we increase the doping, the E_F shifts deep into the band where the DoS is high resulting in larger σ but the derivative of the DoS is smaller deep inside the band which results in smaller thermopower. This idea is also explained through a schematic picture in Figure 1.2(b).

1.3.2 Minimizing Thermal Conductivity (k)

Decreasing thermal conductivity is another way of increasing the ZT value. In a crystalline material, the two important contributors to thermal conductivity (k) are the electronic thermal conductivity (k_{el}) and the lattice thermal conductivity (k_{latt}). The electronic contribution to the thermal conductivity (k_{el}) increases according to the Weideman-Franz (WF) law which is given by

$$k_{el} = L\sigma T \tag{1.11}$$

where L is the Lorenz number. As we could observe from this equation very high electronic conductivities ($\geq$2000 Scm^{-1} [65]) could lead to a significant increase in k_{el} which in turn could lead to decrease in ZT values.

At temperatures above Debye temperature, lattice vibrations (or phonons) have a dominant contribution to the specific heat of the material and in turn the lattice thermal conductivity (k_{latt})[65]. The classical kinetic theory provides a good approximation for the lattice thermal conductivity (k_{latt})[65] which is given as

$$k_{latt} = C_v l v_s \tag{1.12}$$

where C_v is the specific heat of material at constant volume. l is the mean free path of the phonon and v_s is the average velocity of sound.

Historically, one of the most important approaches towards decreasing k_{latt} is to introduce point defects by synthesizing isostructural solid solutions[65]. These point defects induces strong phonon scattering which significantly decreases l and in turn k_{latt}. A classical example for this approach is the introduction of Sb into the Bi_2Te_3 system. The $Bi_{2-x}Sb_xTe_3$, $Bi_2Sb_xTe_{3-x}$ solid solutions have a much lower thermal

conductivity (1.5 $Wm^{-1}K^{-1}$ compared to the value of 2.4 $Wm^{-1}K^{-1}$ in Bi_2Te_3). This drastic reduction in k increases the ZT value in the solid solutions to 1 when compared to the value of 0.6 for the parent compound[65].

The another interesting and potentially revolutionary idea to minimize k was proposed by Slack in 1995[60]. This idea is commonly referred as Phonon-Glass Electron-Crystal (PGEC) approach. As the name suggests PGEC is an approach where the lattice phonons of the semiconductor material experiences a high scattering glass like environment, whereas the electrons see a low scattering crystalline environment. This can be accomplished by introducing cage like structures in materials which contains small atoms. These entrapped atoms exhibit extended anharmonic oscillations called as *rattling* motion. This rattling motion can potentially lead to dramatic reduction in lattice thermal conductivity. The PGEC has stimulated a lot of new research that has lead to increase in ZT values of materials like clathrates[65]. The other successful strategies to reduce thermal conductivity is to utilize boundary scattering[10,25] and nanostructuring in bulk materials[75].

1.4 Materials with high Figure of Merit (ZT)

The most successful thermo-electric materials that have been developed are

- Single-phase materials such as skutterudites (ZT$\sim$ 1.25 at 900K[71]), clathrates (ZT$\sim$0.9 at 1000K[13]), half-heusler compounds (ZT$\sim$ 0.7 at 800K[63]), $\beta - Zn_4Sb_3$ (ZT$\sim$1.3 at 670K[11]).

- Anisotropic chalcogenide based materials such as thallium chalcogenides (ZT$\sim$ 1.2 at 500K[79]), bismuth telluride (ZT$\sim$ 1.0 at 450K[84]).

- Isotropic chalcogenide based materials such as lead telluride (ZT$\sim$ 0.8-1.0 at

650K[19]), $AgSbTe_2/GeTe$ (ZT$\sim$ 1.5 at 750K[64]).

- Inhomogeneous nanostructured materials such as $AgPb_mSbTe_{s+m}$ (ZT$\sim$ 1.7 at 700K[31]), $NaPb_mSbTe_{2+m}$ (ZT$\sim$ 1.6 at 675K[29]), $PbTe/PbS$ (ZT$\sim$ 1.5 at 650K[66]).

1.5 Simultaneous Maximization of Thermopower (S) and Electrical Conductivity (σ)

The above described materials have reasonably good ZT values at high temperatures which makes them useful candidates for high temperature application such as automobiles. But for ambient temperature applications such as wearable electronics or bio-medical devices, we need high values of ZT at ambient temperatures. One of the fundamental limitations in achieving higher ZT at these low ambient temperatures is the inverse relationship between S and σ in bulk semiconducting materials which leads us to the question— *What is the optimal DoS in which the S and σ are both simultaneously high?* This question was initially answered by Mahan *et.al*[40] and Humphrey *et.al*[32] who argued that a material with discrete energy-levels (DoS made up of Dirac distributions) would have the highest efficiency. Discrete energy levels occur only in materials that are quantum confined (length scales of the order of few nanometers where quantum-mechanical effects are predominant) in all three dimensions such as a quantum-dot. Placing these energy levels as close as possible to the Fermi energy (as shown in Fig. 1.3(a)) by tailoring the material structure would simultaneously maximize both thermopower and electrical conductivity.

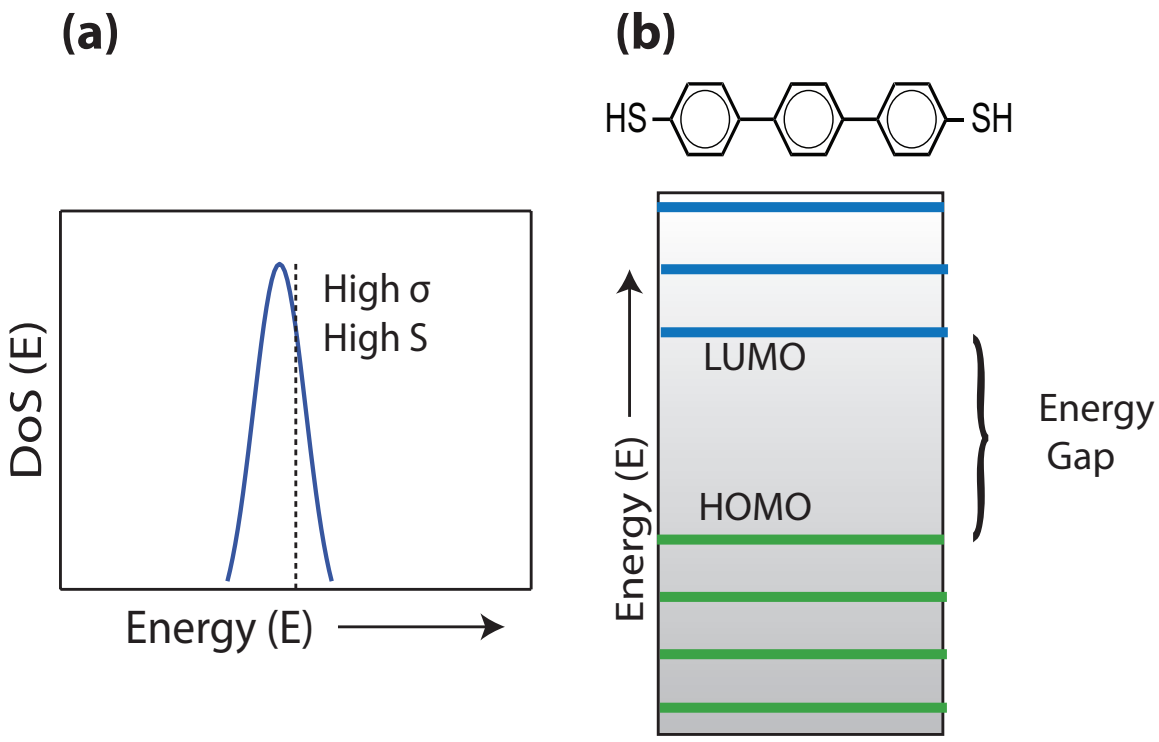

Figure 1.3: (a) Simultaneous maximization of electrical conductivity (σ) and thermopower (S) for a Gaussian shaped DoS. (b) Schematic representation of the discrete energy levels of an aromatic molecule.

1.5.1 Metal-molecule-metal heterojunctions (MMMJs)

The approach described by Mahan & Humphrey leads us to the next question *What is the test system that we can build to test these predictions?*. Metal-molecule-metal heterojunctions (MMMJs) where the aromatic molecules are placed between two metal electrodes (Au in this case) are an excellent test system that can be used both experimentally and computationally to understand the influence of discrete energy levels on the thermoelectric efficiency.

Aromatic molecules are some of the stable nano-scale systems that exist in nature. Their atomic-scale dimensions results in an electronic-structure with discrete energy levels. A schematic picture of these energy levels are provided in

Fig. 1.3(b) where the highest energy level that is occupied with electrons is called as HOMO (highest occupied molecular orbital) and the lowest unoccupied energy level is called the LUMO (lowest unoccupied molecular orbital). The energy difference between the HOMO-LUMO energy levels is the band-gap of the molecule.

When the molecule is placed in contact with the metal electrodes, the molecule tries to align its chemical potential with the metallic Fermi energy (E_F). This results in the molecular energy levels reorganizing to new energies. Further, the wave functions from the molecule and the metals overlap one another resulting in the broadening of the energy levels. This idea is described in the schematic picture shown in Figs. 1.4(a),(b).

Now we can apply a voltage potential across the electrodes. This externally applied potential shifts the chemical potential of the two electrodes. This variation in the chemical potentials result in a non-equilibrium condition that drives electronic transport from one electrode to the other through the aromatic molecule which is measured as current in the external circuit. A schematic picture of this process is described in Fig. 1.4(c).

1.5.2 Conductance (G) in MMMJs

The electronic transport in a nano-scale system like a single molecule is very different from that of larger systems. For example the Ohm's law that describes the relationship between conductance (G) and conductivity (σ) in microscopic systems is given by

$$G = \frac{\sigma A}{L}$$

Based on Ohm's law one would expect that for atomic-scale systems such as single molecule (length $L \rightarrow 0$), the conductance (G) to increase to very high values. However sophisticated theoretical and experimental analysis based on quantum mechanics[17] have shown that in the limit $L \rightarrow 0$, a quantum mechanical system with a perfectly transmitting single energy level has upper limit of conductance called the quantum of conductance G_0 of value $7.74809 \times 10^{-5} S$. This breakdown of the Ohm's law in the nano-scale region can be attributed to the nature of electronic transport. The electron transport in macro-scale and meso-scale systems dominated by scattering based transport. However in case of molecules, the length of the molecule is of the same order of the electron mean free path. This results in the electrons predominantly tunneling through the molecule without any scattering or interaction. The probability of electrons tunneling through the molecules (and in turn G) depends on the length of the molecule and the strength of the coupling between the molecule and metal electrodes. One of the consequences of this tunneling mode of transport is the exponential decay of G as a function of length which has been established by various experimental works[20,83,74,46,69,4,69,77]. Due to this unique nature of electronic transport in these nano-scale systems, the thermoelectric figure of merit (ZT) for these systems are expressed in terms of thermopower (S), electrical conductance (G) and thermal conductance (K) as

$$ZT = \frac{S^2 G}{K} T. \tag{1.13}$$

1.5.3 Thermopower (S) in MMMJs

To understand the influence of electronic-structure on the thermopower S of the MMMJs, we maintain the metallic electrodes at different temperatures. As a result,

the Fermi function of the metallic electrodes are smeared to different magnitudes. The electrode maintained at a higher temperature (T_H) has its Fermi function more smeared compared to the electrode maintained at a lower temperature. As a result the hotter electrodes has more unoccupied (occupied) states below (above) Fermi energy (E_F) when compared to the colder electrode. This occupancy mismatch results in a non-equilibrium condition which drives the electronic transport. This electronic transport is measured on the external circuit as an open-circuit voltage (ΔV). From the applied temperature differential (ΔT) and measured (ΔV), we can calculate the thermopower (S) as

$$S = -\frac{\Delta V}{\Delta T} \tag{1.14}$$

From Figs. 1.5(a),(b), it can be intuitive that the magnitude of the thermopower (S) depends on the energetic difference between the frontier molecular orbital (reorganized HOMO or LUMO) and the metallic Fermi energy (E_F). However, the sign of the thermopower depends on the nature of the frontier molecular orbital. If the reorganized HOMO is closer to the (E_F), the electrons below the (E_F) flow from the cold electrode with higher occupancy to hot electrode with lower occupancy resulting in a positive thermopower (see Fig. 1.5(a)). However if the reorganized LUMO level is closer to the (E_F), the electrons above the (E_F) flow from the hot electrodes with higher occupancy to cold electrode with lower occupancy resulting in a negative thermopower (see Fig. 1.5(b)). Thus measuring thermopower can also help us in determining the nature of electronic transport across molecules. A positive thermopower indicates HOMO dominated transport (p-type) and a negative thermopower indicates a LUMO dominated transport (n-type).

1.6 Organization of Thesis

We had discussed in the previous section that the energy-levels must be positioned very close to metallic Fermi energy (E_F) to simultaneously maximize both the thermopower (S) and electrical conductance (G). In metal-molecule-metal heterojunctions (MMMJs), the positioning of the frontier molecular orbital (FMOs) close to E_F depends on two important aspects namely (i) the relative energy difference between the HOMO/LUMO energies of isolated molecules with respect to E_F and, (ii) the nature of molecular energy level reorganization when brought into contact with the metal electrodes. In this dissertation, we explore the role played by the molecular end-groups (the atoms that bind the molecule to the electrode atoms) in influencing the molecular energy-level reorganization and in turn the thermopower (S) of MMMJs. The analysis is performed by employing ab-initio (density functional theory) based computational models.

Chapter II provides a brief overview of the important historical experimental advancements in understanding the influence of electronic-structure on the electronic transport and transport properties such as conductance (G) and thermopower (S) in MMMJs. This is followed by the explanation of the experiments performed by our collaborators that provided the motivation for this dissertation. Chapter III describes the quantum mechanical formalism that is used to develop computational models to predict the transport properties of MMMJ. This chapter also describes in detail about the computational model and the predicted thermopower (S) and charge injection barrier Δ values for a wide range of Au-aromatic molecule based MMMJs. Chapter IV performs a detailed comparison of the electronic-structure of triphenyl di-thiol $(SS3)$ and triphenyl di-isocyanide $(NC)_2 3$ based MMMJs to understand

how the molecular end-groups influence MMMJ electronic-structure and in turn the sign of their thermopower ($(SS3)$ has positive thermopower whereas $(NC)_2\,3$ has a negative thermopower). This analysis enabled us to propose a hypothesis based on charge transfer between the molecule and metal atoms that provides a consistent explanation to the difference in the sign of thermopower. Further, in this chapter we develop detailed computational models that validate the proposed hypothesis. In chapter V we validate the generality of the hypothesis by applying the hypothesis on MMMJs based on various other aromatic molecules. Finally, we conclude this chapter by developing computational models that can very efficiently predict the molecular energy level reorganization and in turn the sign of the MMMJ thermopower. In chapter VI, we summarize the work and explain how the ideas developed in this work can be extended to perform high throughput analysis of the electronic-structure of various MMMJs to identify the molecule/metal combination with the most optimal electronic-structure to maximize the power factor. In this chapter, we also briefly explain the recent developments in DFT calculations that can lead to quantitative prediction of the power factor of the MMMJs.

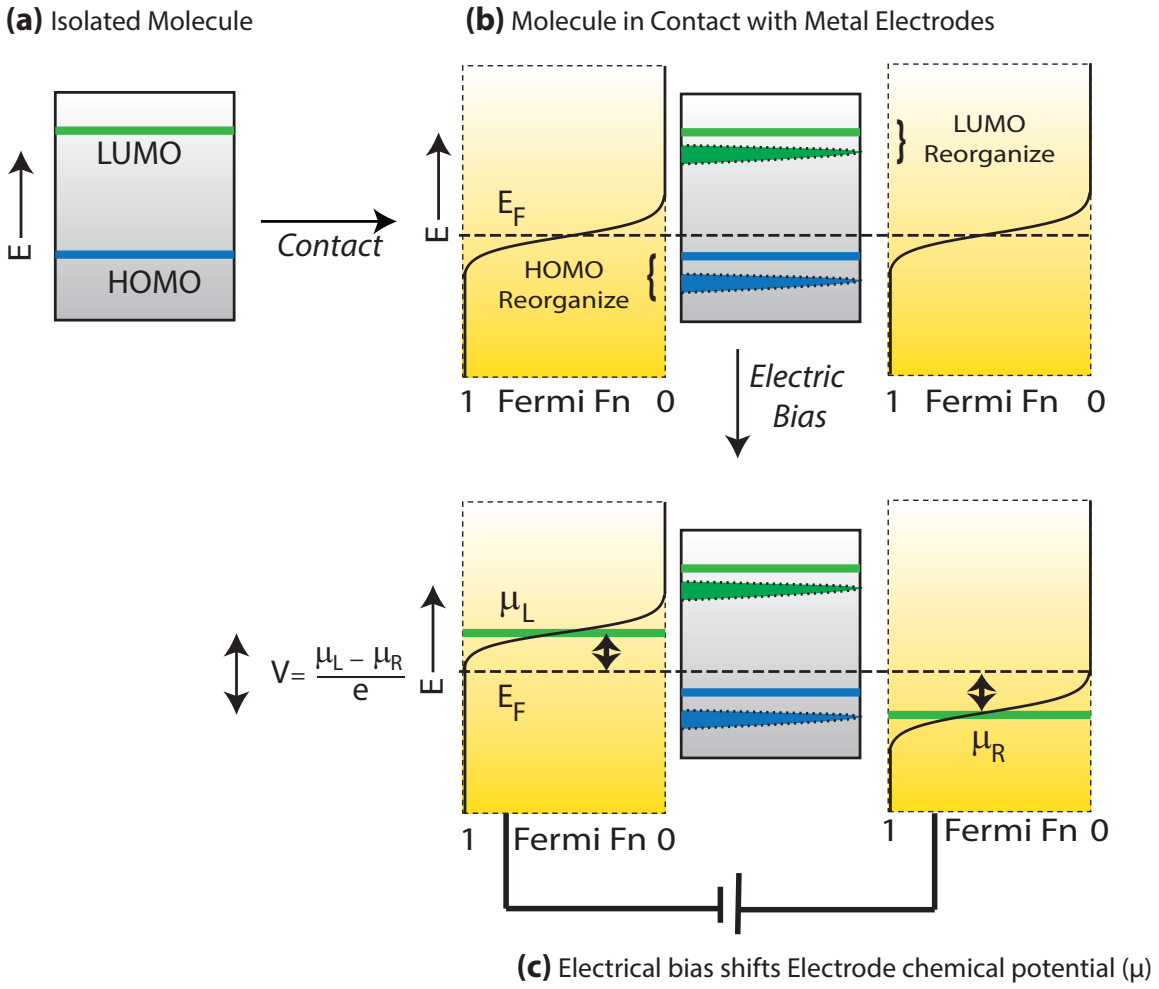

Figure 1.4: (a) Schematic picture of an aromatic molecule with discrete HOMO/LUMO energy levels in an isolated environment. (b) Molecule in contact with metal electrodes that results in the reorganization and broadening of the HOMO/LUMO energy levels of the molecule. (c) Applying a voltage bias shifts the chemical potentials of the metal electrodes which results in the non-equilibrium condition that drives current.

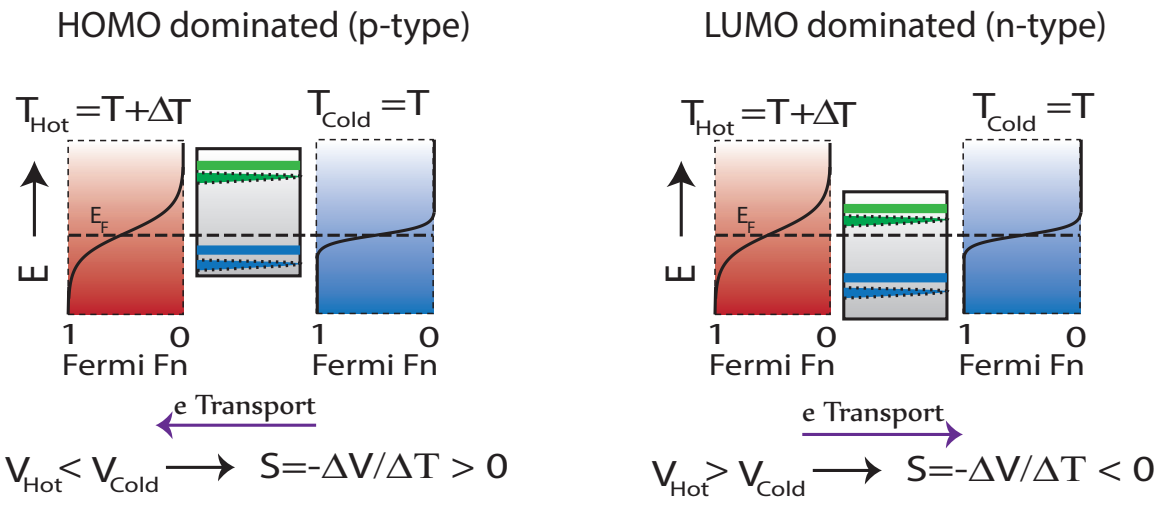

Figure 1.5: Schematic representation of the electronic transport in a MMMJ under a temperature differential (a) MMMJs where the reorganized HOMO energy level is closer to the E_F, electrons flow from the colder electrode to the hotter electrode resulting in a positive thermopower (b) MMMJs where the reorganized LUMO energy level is closer to the E_F, electrons flow from the hotter electrode to the colder electrode resulting in a negative thermopower.

CHAPTER II

Experimental Motivation

2.1 History of Conductance (G) and Thermopower (S) Measurements

In order to design atomic scale electronic or energy conversion systems, we need to understand the electronic and energy transport in these atomic scale systems where the physics of the transport is completely dominated by quantum mechanical effects. Metal-molecules-metal heterojunctions are an excellent test systems to understand the flow of electrons and energy across atomic scale systems. The first important work in this field was done in 1971 by Mann & Kuhn[42] where they performed experiments to measure the electrical conductivity of monolayers of cadmium salts of fatty acids. These measurements showed that the conductivity of these monolayers dropped exponentially with monolayer thickness providing the first experimental evidence of electronic tunneling through these organic monolayers. The first theoretical analysis of using organic molecules as electrical components was proposed by Aviram and Ratner in 1974[3]. In this work they analyzed the electronic transport across single molecules and argued that organic devices arising from single molecules could perform many of the same basic logical operations that are being

performed by inorganic systems. However the first experimental work of attaching metal electrodes to a single molecule to measure its conductance was reported only in 1997 by Reed and co-workers[59]. In this work they employed a mechanically controlled break junction (MCBJ) to trap a single molecule of 1,4 diphenyl dithiol between metal electrodes for long enough time to measure its conductance. In 2002, Park *et.al* developed an electromigrated break junctions (EBJs) based technique to measure the conductance of a cobalt-center organometallic complex[48]. This work provided experimental validation to some unique effects such as Columb blockade and Kondo effect[48] that could only be observed in nano-scale systems. In 2003, Xu & Tao[80] introduced a scanning tunneling microscope (STM) based approach to perform molecular conductance measurements. This approach removed most of the ambiguity in previous works by observing the quantized steps in I-V plots. This approach makes it easy to create, break and recreate the junction in few minutes which makes it possible to create thousands of junctions to perform statistical analysis of molecular conductance. Numerous experimental studies based on improvising this STM based technique and introducing atomic force microscopy (AFM) based techniques provide a detailed understanding of the influence of end-groups and molecular length on the conductance of MMMJs.[20,83,74,46,69,4,69,77]

However conductance measurements alone could not provide information on the nature of transport (p-type or n-type) across these molecular junctions. Paulsson and Datta[51] first suggested that the sign of the Seebeck coefficient, S, of molecular junctions can indicate the dominant mode of transport in thermopower. They argued that a metal-molecule-metal heterojunction (MMMJ) with HOMO (p-type) dominated transport exhibits a positive thermopower whereas a heterojunction with LUMO (n-type) dominated transport exhibits a negative thermopower. A detailed

explanation of this correlation would be provided in chapter III. Reddy *et.al*[56] first experimentally measured the thermopower of thiol terminated phenyl molecules employing a scanning tunneling microscope (STM). This experimental measurement unequivocally established the positive thermopower and in turn the p-type (HOMO) dominated transport in di-thiol terminated phenyl molecules. However in this approach, they were only able to measure the thermopower but not the conductance of the MMMJs. The AFM based experimental setup was designed by Tan et.al in 2010[70] that could concurrently measure the electrical conductance and thermopower of aromatic molecules trapped between Au electrodes. The same group in 2011[69] used this experimental setup to perform a detailed study of conductance of MMMJs based on aromatic molecules with different lengths and end-groups. The results obtained from this experimental work provided the motivation for the computational study elaborated in the subsequent chapters. We now briefly describe the experimental study conducted by our collaborators which provided the motivation for this dissertation.

2.2 Experimental Setup

Fig. 2.1 shows a schematic picture illustrating the experimental setup of metal-molecule-metal heterojunction (MMMJ) built by Tan *et.al*[70,69], which was employed by them to simultaneously measure MMMJ conductance and thermopower. The experimental setup comprises of molecules interacting with a Au coated substrate through their end-groups in turn creating a self-assembled monolayer. Monolayers were characterized using ellipsometry and X-ray photo-electron spectroscopy to determine thickness and chemical composition. The AFM cantilever tip makes a soft mechanical contact ($\sim$ 1nN contact force) with the Au substrate covered

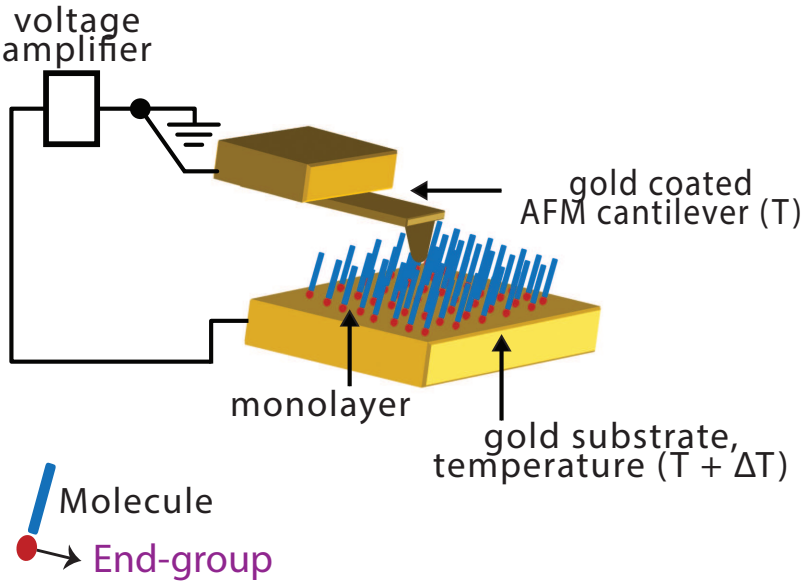

Figure 2.1: Schematic representation of the experimental setup adapted from Tan *et.al*[69]. The experimental setup can concurrently measure MMMJ conductance and thermopower.

with the monolayer of molecules. This creates a MMMJ encompassing multiple molecules (∼100). The electrical characteristics of the MMMJ is measured by grounding the AFM tip and applying a bias voltage to the substrate. A low-noise current amplifier was used to monitor the electrical current during these measurements. To measure the thermopower (i) an electrical heater is used to heat the substrate to an elevated temperature T+ΔT and the AFM cantilever tip is anchored to a thermal reservoir which is maintained at temperature T. This setup ensured atleast 95% of the temperature differential (ΔT) occurs across the molecules trapped in between the metal electrodes. The resultant thermoelectric voltage of the junction is measured by a custom-built voltage amplifier. More detailed information of this experimental setup are provided in Tan *et.al*[70,69].

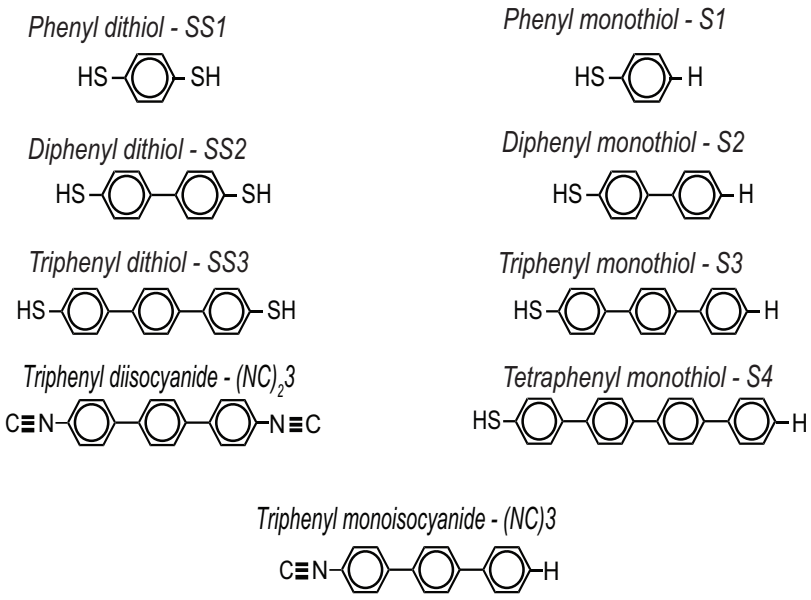

Figure 2.2: Aromatic molecules that were studied experimentally by Tan *et.al*[69].

2.3 Conductance (G) and Thermopower (S) Measurements

The low bias electrical resistances (R) of the MMMJs were measured by applying a voltage range from $+0.3V$ to $-0.3V$ between the tip and the substrate. The measured values of R for mono-thiol and di-thiol terminated molecules are shown in Figure 2.3(a). As observed from the Figure 2.3, the resistance of the molecules increases exponentially with length, indicating that the dominant mode of transport is the quantum mechanical tunneling. Further it is also observed that the electrical resistance of the monothiol junctions is at least an order of magnitude larger than the corresponding dithiol junctions. This can be attributed to the weak interaction between the monothiol molecules and the Au electrode atoms at the H end.

Thermoelectric voltage measurements were performed by applying a temperature differential ΔT between the tip and the substrate. Temperature differentials ranging from 0K to 12K were applied in steps of 3K to measure the temperature differential. The measured thermoelectric voltage ΔV of the dithiol and monothiol

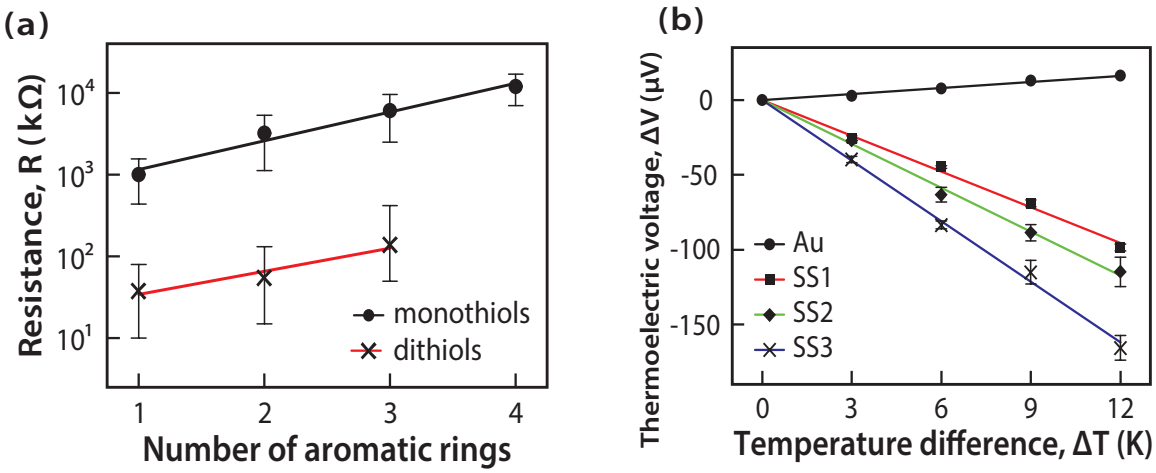

Figure 2.3: Experimental measurements conducted by Tan *et.al*[69,68]. (a) Measured resistance values plotted as a function of number of phenyl rings for monothiol and dithiol terminated MMMJs. (b) Measured thermoelectric voltage ΔV values as a function of applied temperature differential ΔT for dithiol terminated MMMJs.

terminated molecules are shown in Figs. 2.3(b) and 2.4(a) respectively. The magnitude of the measured thermoelectric voltage ΔV increases linearly as the applied temperature differential ΔT. The measured thermoelectric voltage is related to the thermopower (S) of the junction (S) by the following expression[69]

$$S = S_{Au} - \frac{\Delta V}{\Delta T}, \tag{2.1}$$

where, S_{Au} is the thermopower of gold.

The resultant thermopower (S) obtained from the measured thermo-electric voltage is provided in Table 2.1. As observed from Table 2.1, the thermopower (S) increases linearly with increasing length. The values obtained from AFM experimental setup (measuring for about 100 molecules) is very similar to those obtained from STM setup that measures single molecule thermopower[56]. This correlation indicates that the inter-molecular interactions in the studied monolayers are small

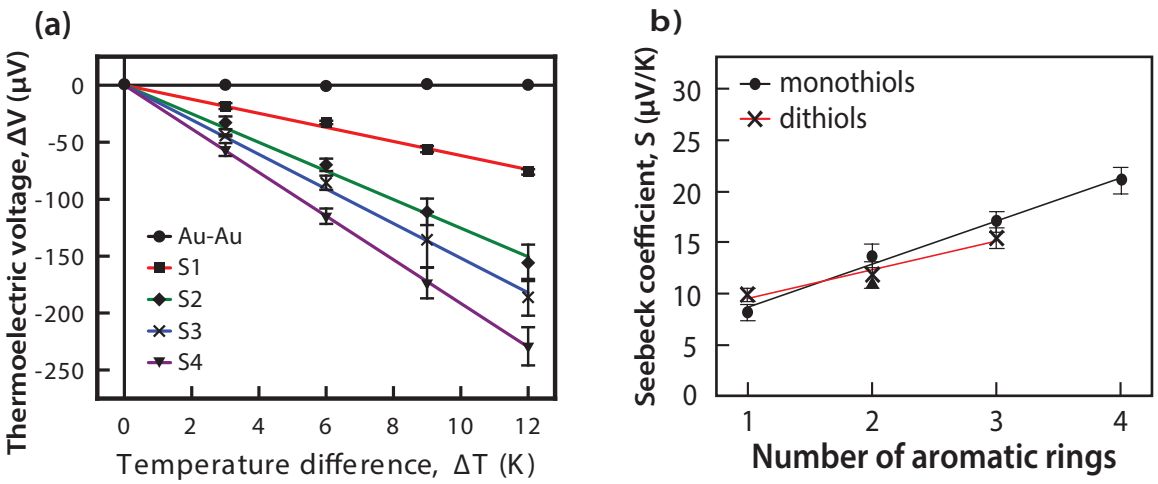

Figure 2.4: Experimental measurements conducted by Tan *et.al*[69,68]. (a) Measured thermoelectric voltage ΔV values as a function of applied temperature differential ΔT for monothiol terminated MMMJs. (b) Measured thermopower values plotted as a function of number of phenyl rings for monothiol and dithiol terminated MMMJs.

and do not significantly affect the measured thermopower. This result also justifies the employment of computational models based on single molecule junctions that would be developed and employed in the subsequent chapters to analyze these properties.

Further it is also observed that the thermopower of mono-thiol molecules is very similar to that of di-thiol molecules although their electrical resistance are very different. This can be attributed to the role of contact coupling strength on the MMMJ properties. This behavior is well explained using a simple model by Paulsson and Datta[51]. In this picture the transmission function of a weakly bound junction is related to the transmission of a strongly bound junction by a scaling factor ($0 < c < 1$):

$$\tau(E)_{weak} = c\tau(E)_{strong}$$

For the aforementioned relationship between transmission functions $\tau(E)$, we can demonstrate that the conductance values of these two systems are widely different but their thermopower values would remain the same (see chapter III for more information).

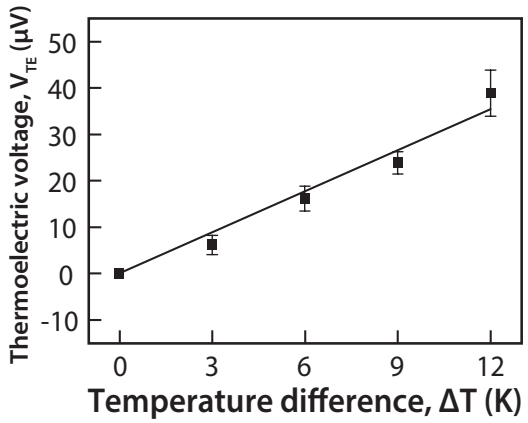

Figure 2.5: Experimental measurements conducted by Tan *et.al*[69,68]. (a) Measured thermoelectric voltage ΔV values as a function of applied temperature differential ΔT for triphenyl isocyanide based MMMJ.

This experimental setup was also used to measure the electrical resistance and the thermopower of triphenyl monoisocyanide $(NC)\,3$ based MMMJs. The thermopower measured for these MMMJs were found to be negative (-1.0 ± 0.4) which in turn indicates that the transport in these molecular junctions are dominated by LUMO level (p-type transport). It is interesting to note that when the contact coupling is reduced by removing one of the thiol groups, the thermopower is relatively invariant. However, changing the end groups from thiol to isocyanide changes not only the magnitude of the Seebeck coefficient but also its sign.

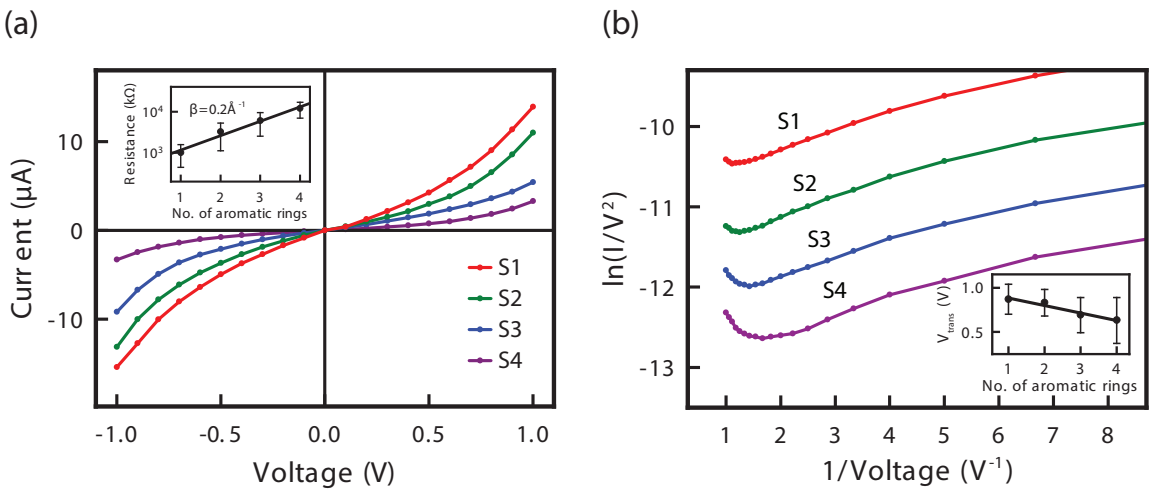

Figure 2.6: Experimental measurements conducted by Tan *et.al*[69,68]. (a)I-V plots for monothiol terminated MMMJs. (b) Measured thermoelectric voltage ΔV values as a function of applied temperature differential ΔT for triphenyl isocyanide based MMMJ. (b)Fowler-Nordheim (F-N) plot for MMMJs with monothiol terminated phenyl molecules. The minimal value in the F-N plot represents the transition voltage (V_{trans}) of the MMMJ. The inset shows the measured (V_{trans}) as a function of molecular length.

2.4 Transition Voltage Spectroscopy Measurements

Although the thermopower measurements can identify the nature of the closest frontier molecular orbital FMO (HOMO or LUMO), these measurements cannot determine the energetic separation between the Fermi energy and the closest frontier molecular orbital (FMO). However transition voltage spectroscopy (TVS) can be used to estimate these energetic separations[8]. In order to perform TVS, the current-voltage (I-V) characteristics of the metal-molecule-metal heterojunctions (MMMJs) are measured for high voltage bias. This is accomplished by sweeping an applied bias across the MMMJs from +1.0 V to -1.0 V while measuring the electric current flowing through the junctions. The measured I-V characteristics for monothiol based MMMJs $(S1 - S4)$ are shown in Fig. 2.6(a). Once the I-V characteristics of the

System	Experimental measurements conducted by Tan *et.al*[69,68]	
	Thermpower S $(^{\mu V}/_{K})$	Transition Voltage eV_{trans} (eV)
$SS1$	9.8 ± 0.6	-
$SS2$	11.7 ± 1.3	-
$SS3$	15.4 ± 1.0	-
$S1$	8.1 ± 0.8	0.87 ± 0.17
$S2$	13.6 ± 1.2	0.83 ± 0.15
$S3$	17.6 ± 1.0	0.69 ± 0.20
$S4$	21.0 ± 1.3	0.69 ± 0.26
$(NC)\,3$	-1.0 ± 0.4	-

Table 2.1: Experimental measurements conducted by Tan *et.al*[69,68]. Thermopower S and transition voltage eV_{trans} values experimentally measured of MMMJs made up of phenyl molecules with monothiol, dithiol and isocyanide end-groups.

MMMJs were obtained, these values were further analyzed by plotting a Fowler-Nordheim (F-N) curve: $\ln {}^{I}/_{V^2}$ against ${}^{1}/_{V}$. The F-N curves for the monothiol based MMMJs are shown in Fig. 2.6(b). The F-N curves of all the heterojunctions contain a minimum. The voltage corresponding to the minimum of the F-N curve, called the transition voltage (V_{trans})[8], can be related to the energetic separation Δ (*aka* injection barrier) between the MMMJ Fermi energy E_F and the dominant frontier molecular orbital as,

$$eV_{trans} \sim \Delta \tag{2.2}$$

where e is the charge of an electron. Conventionally, the I-V data obtained at positive voltages are used in the F-N plot. The positive bias corresponds to the scenario where the substrate is grounded and a positive voltage is applied to the cantilever tip. It has also been observed that the transition voltage eV_{trans} is independent of the number of molecules and in turn on the radius of the AFM tip. The measured V_{trans} values of all the AMMJs are shown in the inset of Fig. 2.6(b) as well as in Table 2.1. The values of V_{trans} for Au-S1-Au, Au-S2-Au, Au-S3-Au junctions match

well with the previous experimental results[8]. The experimentally obtained V_{trans} values indicate that the energetic separation (Δ) between the E_F and the dominant frontier molecular orbital decreases with increasing molecular chain length.

The results obtained from these experiments pose two interesting observations on the influence of molecular structure on the heterojunction's (MMMJ) transport properties. (i) Changing the end-group from thiol to isocyanide changed the sign of the thermopower of triphenyl based MMMJs– which in turn indicates a shift from p-type transport in thiol terminated molecular systems to n-type transport in isocyanide terminated molecular systems. (ii) The energetic separation (Δ) between the E_F and the dominant frontier molecular orbital of monothiol based molecular junctions decreases with increasing molecular chain length. Unfortunately, experiments alone cannot provide insights into the influence of the molecular structure on the MMMJ electronic-structure and in turn its transport properties. To this end, we develop an ab-initio based computational model which can quantitatively predict the thermopower and energetic separation for all these molecules. We then use the developed computational model to systematically analyze the influence of the molecular structure on the transport properties such as thermopower S and energetic separation Δ which are very important in improving the thermoelectric properties of these systems.

CHAPTER III

Modeling MMMJ Transport Properties

In chapter I we had briefly discussed how the electrical conductance (G) of a macro-scale semiconducting system is related to its electrical conductivity (σ). This relationship famously known as Ohm's law is given as

$$G = \frac{\sigma A}{L}$$

where A is the cross-sectional area and L is the length of the system. The electrical transport across these systems can be quantitatively modeled through the Boltzmann Transport Equation (BTE). However in atomic-scale systems such as single molecules where the length of the system $L \rightarrow 0$, the above approach breaksdown. This breakdown in the nano-scale region can be attributed to the nature of electronic transport. The electron transport in macroscopic systems is dominated by scattering based transport (diffusive transport). However, in case of molecules the electrons predominantly tunnel through the molecule without any scattering (ballistic transport). In order to capture this quantum mechanical ballistic transport we need to employ a formalism that was proposed by Rolf Landauer[38] and developed into a comprehensive theory by Markus Buttiker, Yigal Meir and Ned Wingreen[18,17].

Their approach to calculate the transport properties of nanojunctions will be briefly explained in the following sections.

3.1 Landauer Formalism

Landauer formalism is one of the most famous approaches towards solving transport across nano-scale junctions[38,18]. This formalism provides an explicit relationship that relates the experimental observable such as the total current (I_{Tot}), conductance G and thermopower S to the electronic-structure of the system.

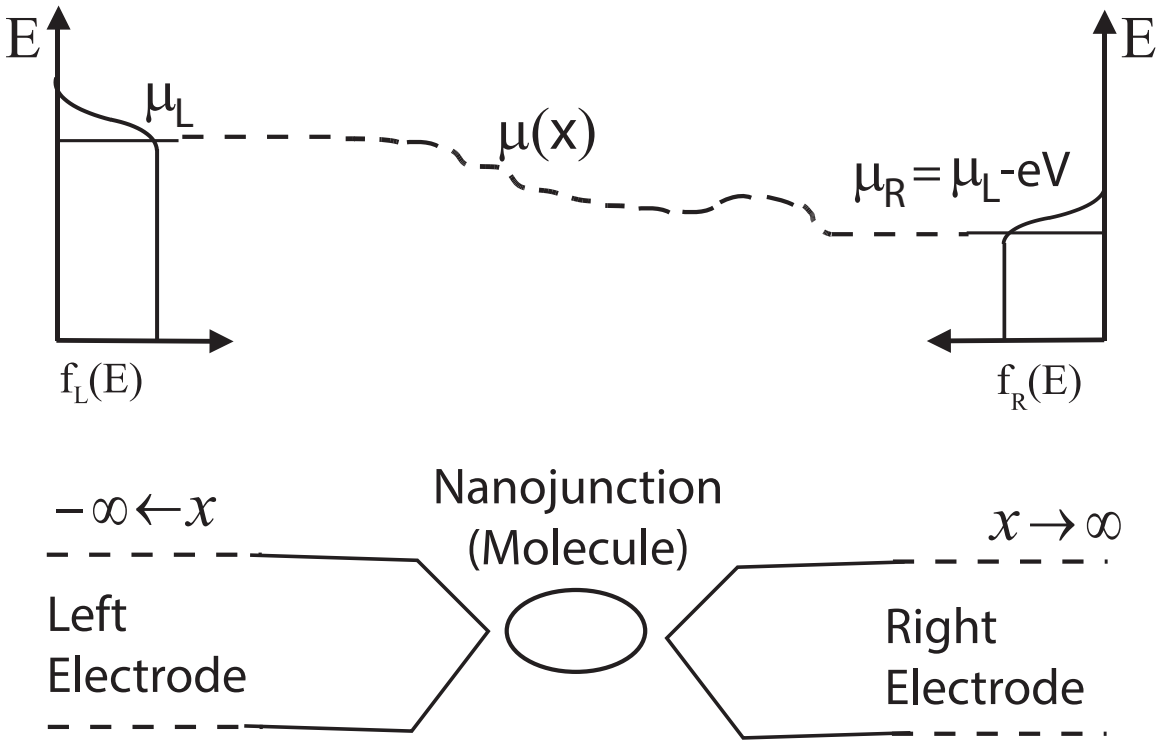

Figure 3.1: Landauer model of electronic transport where the nanojunction is connected to two semi-infinite electrodes. The voltage bias is applied across the nanojunction by changing the chemical potential of the electrodes which results in a current flow.

3.1.1 Model Description

The Landauer model system comprises of the nano-scale junction (in this case a molecule) in contact with two large metallic electrodes as shown in Fig. 3.1. The metallic electrodes which are in contact with the nano-scale junction are assumed to be semi-infinite electrodes/reservoirs. Reservoirs are systems that can donate/accept arbitrary number of electrons without any change to its internal state (electronic-structure or its Fermi energy (E_F)). The semi-infinite metallic electrodes enables us to assume the whole system to be in steady state where its electronic-structure (characterized by the density operator of the system $\hat{\rho}$) is assumed to be independent of time. The whole infinite system encompassing the nanojunction and semi-infinite electrodes can be described by a Hamiltonian $\hat{H}$. The reservoir far away from junction is assumed to be in equilibrium and its states non-interacting. Hence, we can fill these states based upon the Fermi-Dirac distribution. The voltage bias across the nano-scale junction is applied by changing the chemical potential of the electrodes.

$$\Delta V = (\mu_L - \mu_R)/e$$

This change in the chemical potential of the two electrodes creates a non-equilibrium condition that drives the current flow across the nano-scale junction.

3.1.2 Global Current (I_{Tot}) Description in Landauer Model

In this section, we explain the approach to mathematically describe the steady state global current (I_{Tot}) across nano-scale junctions. Let $\boldsymbol{x}$ indicate a position vector in $\mathbb{R}^3$. Let x be the transport direction and let $\boldsymbol{x}_\perp$ indicate a vector in direction normal to transport direction (in this case (y,z)). Let $\hat{H}_0$ be the Hamiltonian

corresponding to the electrodes.

Let $|\chi_i\rangle$ be an eigen state of H_0 that starts deep inside the left electrode in the past ($x \to -\infty, t \to -\infty$). The $|\chi_i\rangle$ has a well defined energy E and momentum (k) that is directed towards the nanojunction. The state now travels towards the nanojunction where it experiences a different spatially localized potential (V) and gets elastically scattered. A part of the wave $\left|\psi_{i,Tr}\right\rangle$ gets transmitted into the right electrode while the rest of it $\left|\psi_{i,Re}\right\rangle$ gets reflected to the left electrode. The transmitted and reflected waves can be expressed as linear combination of states with the same energy E.

$$\begin{aligned} \left|\psi_{i,Tr}\right\rangle &= \sum_{f=1}^{N(E)} T_{if} \left|\chi_f\right\rangle \\ \left|\psi_{i,Re}\right\rangle &= |\chi_i\rangle + \sum_{f=1}^{N(E)} R_{if} \left|\chi_f\right\rangle \end{aligned} \tag{3.1}$$

The transmitted part of the wave travels into the right electrode. The current due to this transmitted state from the left electrode can be calculated deep inside the right electrode ($x \to \infty$) as

$$I_{i,Tr}(E) = e \int_{\partial\Omega} \left\langle \psi_{i,Tr} \right| \hat{j}_x \left| \psi_{i,Tr} \right\rangle d\boldsymbol{x}_\perp \tag{3.2}$$

where $\hat{j}_x$ is the current density operator along the transport (x) direction.

The total global current (I_{Tot}) arising from all the relevant states in a steady state system is invariant to the spatial location in the system. For example, the (I_{Tot}) calculated deep inside the left electrode is the same as the one calculated deep inside the right electrode. Here, we calculate the (I_{Tot}) deep inside the right electrode. The

(I_{Tot}) calculated deep in the right electrode has two contributions namely, (i) the transmitted states that originate from the left electrode and (ii) the reflected states that originate from the right electrode.

The global current (I_{Tot}) can be calculated by summing over all the transmitted (reflected) states that originate from left (right) electrode at a given energy E and then integrating all the energies from $-\infty$ to ∞. This idea can be mathematically expressed as,

$$I_{Tot} = 2 \int_{-\infty}^{\infty} dE \left\{ \sum_{i=1}^{N(E)} I_{i,Tr}(E) D_i(E) f_L(E - \mu_L) - \sum_{i=1}^{N(E)} I_{i,Re}(E) D_i(E) f_R(E - \mu_R) \right\} \tag{3.3}$$

where the factor 2 is due to the spin multiplicity, $D_i(E)$ corresponds to the density of states of at energy E and $f_{L/R}$ corresponds to the Fermi-Dirac distribution corresponding to the left and right electrode. Within the approximation of identical electrodes and steady state current, the equations in the first and second parts of integral must be the same

$$\sum_{i=1}^{N(E)} I_{i,Tr}(E) D_i(E) = \sum_{i=1}^{N(E)} I_{i,Re}(E) D_i(E) \tag{3.4}$$

Assuming that the incoming states are plane waves, the above equation can be sim-

plified as

$$\begin{aligned}
\sum_{i=1}^{N(E)} I_{i,Tr}(E)D_i(E) &= \sum_{i=1}^{N(E)} I_{i,Tr}(E)D_i(E) \\
&= \sum_{i=1}^{N(E)} |I_i(E)| \frac{I_{i,Tr}(E)}{|I_i(E)|} D_i(E) \\
&= \frac{e}{2\pi\hbar} \sum_{i=1}^{N(E)} \frac{I_{i,Tr}(E)}{|I_i(E)|} \quad \left(\text{under plane wave assumption } |I_i(E)|D_i(E) = \frac{e}{2\pi\hbar}\right) \\
&= \frac{e}{2\pi\hbar}\tau(E)
\end{aligned} \tag{3.5}$$

where $\tau(E)$ is the normalized transmission or transmission function that describes the probability of an electron with energy E to transmit across the molecule. The $\tau(E)$ is mathematically defined as

$$\tau(E) = \sum_{i=1}^{N(E)} \frac{I_{i,Tr}(E)}{|I_i(E)|} \tag{3.6}$$

$I_i(E)$ is the current due to the original state defined as,

$$I_i(E) = e \int_{\partial\Omega} \langle \chi_i | \, \hat{j}_x \, | \chi_i \rangle \, d\boldsymbol{x}_\perp$$

The total current (I_{Tot}) can now be rewritten as

$$\begin{aligned}
I_{Tot} &= \frac{2e}{2\pi\hbar} \int_{-\infty}^{\infty} \tau(E) \left[f_L\left(E - \mu_L\right) - f_R\left(E - \mu_R\right) \right] dE \\
&= \frac{2e}{h} \int_{-\infty}^{\infty} \tau(E) \left[f_L\left(E - \mu_L\right) - f_R\left(E - \mu_R\right) \right] dE
\end{aligned} \tag{3.7}$$

As you could observe from this equation, the total global current is non-zero only if you apply an external voltage bias ΔV which shifts the chemical potential of the electrodes.

3.1.3 Conductance (G) Description in Landauer Model

The Eq. 3.7 provides an explicit relationship relating the global current (I_{Tot}) to the transmission function $(\tau(E))$ of the nanojunction. Similarly we would also like to have a relationship between conductance (G) and the transmission function $(\tau(E))$. In order to obtain this relationship, we assume that the applied voltage (ΔV) bias shifts the chemical potential of the electrodes symmetrically about the Fermi energy (E_F)

$$\begin{aligned} \mu_L &= E_F + \frac{\Delta V}{2} e \\ \mu_R &= E_F - \frac{\Delta V}{2} e \end{aligned} \tag{3.8}$$

Further we also assume that the applied ΔV is very small $(\Delta V \to 0)$. Under this approximation we can expand the Fermi-Dirac distribution of left electrode about E_F as

$$\begin{aligned} f_L\left(E-\mu_L\right) &= f(E-E_F) + \frac{\partial f}{\partial \tilde{E}}\Big|_{\tilde{E}=E_F} (\mu_L - E_F) \\ &= f(E-E_F) + \frac{\Delta V}{2} e \frac{\partial f}{\partial \tilde{E}}\Big|_{\tilde{E}=E_F} \end{aligned} \tag{3.9}$$

Similarly we can expand the Fermi-Dirac distribution of left electrode about E_F as

$$f_R\left(E-\mu_R\right) = f(E-E_F) - \frac{\Delta V}{2} e \frac{\partial f}{\partial \tilde{E}}\Big|_{\tilde{E}=E_F} \tag{3.10}$$

The difference between the Fermi-Dirac distribution of the two electrodes can be written as

$$\begin{aligned} f_L\left(E-\mu_L\right)-f_R\left(E-\mu_R\right) &= 2e\frac{\Delta V}{2}\frac{\partial f}{\partial \tilde{E}}\Big|_{\tilde{E}=E_F} \\ &= -2e\frac{\Delta V}{2}\frac{\partial f}{\partial E}\Big|_{E=E_F} \quad \left(\frac{\partial f}{\partial E}=-\frac{\partial f}{\partial \tilde{E}}\text{due to form of } f\right) \end{aligned} \tag{3.11}$$

Substituting the above equation in 3.7 we get

$$I_{Tot}=\frac{2e^2}{h}\Delta V\int_{-\infty}^{\infty}\tau(E)\left(-\frac{\partial f}{\partial E}\Big|_{E=E_F}\right)dE \tag{3.12}$$

In the low temperature limit $(T\rightarrow 0)$, the Fermi-Dirac distribution becomes a heavy-side function and hence its derivative $\left(-\frac{\partial f}{\partial E}\right)$ becomes a Dirac delta distribution. Applying this assumption to previous Eq. we get,

$$I_{Tot}=\frac{2e^2}{h}\Delta V\tau(E_F) \tag{3.13}$$

Finally, the conductance of the nanojunction under these assumptions can be written as

$$G=\frac{I_{Tot}}{\Delta V}=\frac{2e^2}{h}\tau(E_F) \tag{3.14}$$

where the constant $\frac{2e^2}{\hbar}$ is called as the universal quantum of conductance (G_0) which is the upper limit value for a perfectly conducting quantum system (i.e, when $\tau(E)=1$).

3.1.4 Thermopower (S) Description in Landauer Model

In the MMMJ system, applying a temperature differential ΔT across the metal electrodes modifies the Fermi-Dirac distribution of the electrodes which results in a non-equilibrium condition that drives electronic transport. This non-equilibrium condition results in a voltage differential which is measured in the external circuit as the open-circuit voltage ΔV. The thermopower S (*aka* Seebeck coefficient) is the negative ratio of the open-circuit voltage measured to the applied temperature differential

$$S = -\frac{\Delta V}{\Delta T} \tag{3.15}$$

Now we would also like to obtain an expression that directly relates S to the transmission function of the nanojunction $\tau(E)$. We had previously seen the expression for current as a function of $\tau(E)$ for very low external voltage bias (see Eq. 3.13). Now the same current can also be obtained by applying a temperature differential across the electrodes

$$I_{Tot} = \frac{2e}{h} \int_{-\infty}^{\infty} \tau(E) \left[f_L \left(E - T_L \right) - f_R \left(E - T_R \right) \right] dE. \tag{3.16}$$

The temperature differential across the system is given by $\Delta T = T_L - T_R$ and the average temperature is $T_A = \frac{T_L + T_R}{2}$. The integrals in the previous equation can be expanded by performing Sommerfeld expansion[2] as

$$\int_{-\infty}^{\infty} \tau(E) f_L \left(E - T_L \right) = \int_{-\infty}^{E_F} \tau(E) dE + \frac{\pi^2}{6} \left(k_B T_L \right)^2 \frac{\partial \tau(E)}{\partial E} \Big|_{E=E_F}, \tag{3.17}$$

$$\int_{-\infty}^{\infty} \tau(E) f_R\left(E - T_R\right) = \int_{-\infty}^{E_F} \tau(E) dE + \frac{\pi^2}{6} \left(k_B T_R\right)^2 \frac{\partial \tau(E)}{\partial E}\Big|_{E=E_F}. \tag{3.18}$$

Substituting the above expansion in Eq. 3.16 and assuming low temperature differential ($\Delta T \to 0$) we get

$$I_{tot} = -2T_A \Delta T \frac{2e}{h} \frac{\pi^2 k_B^2}{6} \frac{\partial \tau(E)}{\partial E}\Big|_{E=E_F}. \tag{3.19}$$

Equating the current equations obtained from external voltage bias (Eq. 3.13) and temperature differential (Eq. 3.19) we get

$$S = -\frac{\Delta V}{\Delta T} = -\frac{\pi^2 k_B^2 T_A}{3e} \frac{1}{\tau(E_F)} \frac{\partial \tau(E)}{\partial E}\Big|_{E=E_F}. \tag{3.20}$$

Thus the above equation describes the thermopower S of the nanojunction as a function of transmission function $\tau(E)$ and its derivative.

3.2 Computing Transmission Function

We could observe from Eqs. 3.7,3.14 and 3.20 that all the transport properties of nanojunction such as current, conductance and thermopower depend on the transmission function $\tau(E)$ of the nanojunction. Thus, $\tau(E)$ is the most fundamental quantity which needs to be computed for calculating the transport properties. The most successful approach to calculate the $\tau(E)$ of real molecules attached to metal atoms is based on non-equilibrium Green's function (NEGF). The NEGF approach that will be described in the subsequent sections closely follows the pioneering work

of Ratner, Datta and co-workers[16,82].

3.2.1 Green's Function of Schrödinger's Equation

The time dependent Schrodinger equation is given as

$$i\hbar\frac{d\left|\psi(t)\right\rangle}{dt} = \hat{H}\left|\psi(t)\right\rangle \quad \left|\psi(t_0)\right\rangle = \left|\psi_0\right\rangle. \tag{3.21}$$

The Green's function corresponding to this first order differential equation in time subject to homogeneous initial condition can be expressed as

$$\left(i\hbar\frac{d}{dt} - \hat{H}\right)\hat{G}(t,t') = \delta(t-t') \quad \hat{G}(t_0,t') = 0. \tag{3.22}$$

The Green's function can be solved in two different scenarios namely (i) the positive time axis $(t, t' > t_0)$ and (ii) the negative time axis $(t, t' < t_0)$

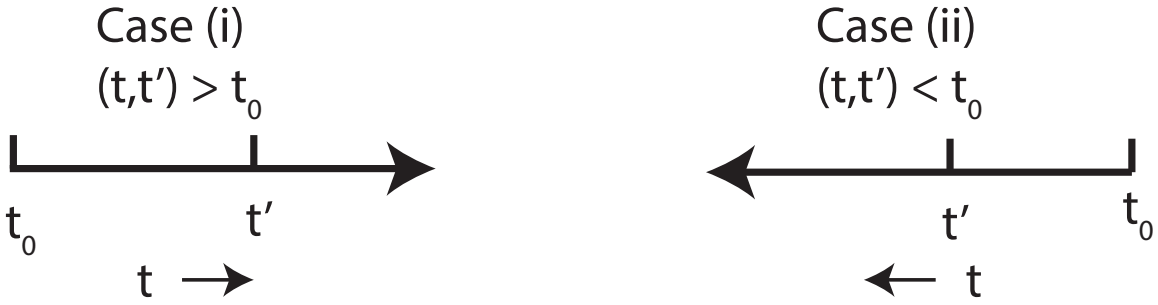

$(\mathbf{i})\mathbf{t}, \mathbf{t}' > \mathbf{t_0}$ In the case of positive time axis, the Green's function is given by,

$$\begin{aligned}\hat{G}^{-}(t,t') &= C^{-}(t')e^{\frac{-iHt}{\hbar}} \quad t < t' \\ \hat{G}^{+}(t,t') &= C^{+}(t')e^{\frac{-iHt}{\hbar}} \quad t > t'\end{aligned} \tag{3.23}$$

Applying the initial condition is applied on $\hat{G}^{-}(t,t')$ we get,

$$\hat{G}^{-}(t_0,t')=0 \quad \Rightarrow \quad C^{-}(t')=0 \quad \Rightarrow \quad \hat{G}^{-}(t,t')=0 \tag{3.24}$$

Applying the jump discontinuity condition, we get

$$\begin{aligned}\hat{G}^{+}(t'_{+},t')-\hat{G}^{-}(t'_{-},t')&=\frac{1}{i\hbar}=\frac{-i}{\hbar}\\ C^{+}(t')e^{\frac{-iHt'}{\hbar}}-0&=\frac{-i}{\hbar}\\ \hat{G}^{+}(t'_{+},t')=\frac{-i}{\hbar}e^{\frac{-iH(t-t')}{\hbar}}&\end{aligned} \tag{3.25}$$

$(\mathbf{ii})\mathbf{t},\mathbf{t'}<\mathbf{t_0}$ In the case of the negative time axis, the Green's function is given by,

$$\begin{aligned}\hat{G}^{-}(t,t')&=C^{-}(t')e^{\frac{-iHt}{\hbar}} \quad t<t'\\ \hat{G}^{+}(t,t')&=C^{+}(t')e^{\frac{-iHt}{\hbar}} \quad t>t'\end{aligned} \tag{3.26}$$

Applying the initial condition is applied on $\hat{G}^{+}(t,t')$ we get,

$$\hat{G}^{+}(t_0,t')=0 \quad \Rightarrow \quad C^{+}(t')=0 \quad \Rightarrow \quad \hat{G}^{+}(t,t')=0 \tag{3.27}$$

Applying the jump discontinuity condition, we get

$$\begin{aligned}\hat{G}^{+}(t'_{+},t')-\hat{G}^{-}(t'_{-},t')&=\frac{1}{i\hbar}=\frac{-i}{\hbar}\\ 0-C^{-}(t')e^{\frac{-iHt'}{\hbar}}&=\frac{-i}{\hbar}\\ \hat{G}^{-}(t'_{+},t')=\frac{i}{\hbar}e^{\frac{-iH(t-t')}{\hbar}}&\end{aligned} \tag{3.28}$$

Since the Green's function is only a function of $\hat{t}=t-t'$, it can be transformed to be expressed in the energy domain. Since the Green's function is not absolutely

integrable, we perform a Laplace transform of the Green's function as

$$\begin{aligned}
\hat{G}^{+}(E) &= \mathcal{L}\left(\hat{G}^{+}(t'_{+}, t')\right) \\
&= \lim_{\eta \to 0} \int_{-\infty}^{\infty} \theta(t-t') \hat{G}^{+}(t'_{+}, t') e^{\frac{iE(t-t')}{\hbar}} e^{\frac{-\eta(t-t')}{\hbar}} dt \\
&= \lim_{\eta \to 0} \int_{t'}^{\infty} \frac{-i}{\hbar} e^{\frac{-iH(t-t')}{\hbar}} e^{\frac{iE-\eta}{\hbar}(t-t')} dt
\end{aligned} \tag{3.29}$$

Substituting $\hat{t} = t - t'$ in the above equation we get

$$\begin{aligned}
\hat{G}^{+}(E) &= \frac{-i}{\hbar} \lim_{\eta \to 0} \int_{t'}^{\infty} e^{\frac{-iH\hat{t}}{\hbar}} e^{-\frac{\eta - iE}{\hbar}\hat{t}} dt \\
&= \frac{-i}{\hbar} \lim_{\eta \to 0} \int_{t'}^{\infty} e^{\frac{-iH\hat{t}}{\hbar}} e^{-s\hat{t}} dt \qquad \left(s = \frac{\eta - iE}{\hbar}\right) \\
&= \lim_{\eta \to 0} \frac{-i}{\hbar} \frac{1}{\frac{\eta - iE}{\hbar} + \frac{iH}{\hbar}} \qquad \left(\mathcal{L}\left[e^{at}\right] = \frac{1}{s-a}\right) \\
&= \lim_{\eta \to 0} \frac{1}{z - H} \qquad (z = E + i\eta)
\end{aligned} \tag{3.30}$$

Similarly we can obtain an expression for $\hat{G}^{-}(E)$. The final expression for the Green's function expressed in energy domain is given as

$$\begin{aligned}
\hat{G}^{+}(z) = \hat{G}^{r}(z) &= \lim_{\eta \to 0} \frac{1}{z - H}, \quad (z = E + i\eta) \\
\hat{G}^{-}(z) = \hat{G}^{a}(z) &= \lim_{\eta \to 0} \frac{1}{\bar{z} - H},
\end{aligned} \tag{3.31}$$

where $\hat{G}^{r}(E)$ and $\hat{G}^{r}(E)$ are the more common ways of representing $\hat{G}^{+}(z)$ and $\hat{G}^{-}(z)$. The $\hat{G}^{r}(E)$ and $\hat{G}^{a}(E)$ symbols indicate that they are retarded Green's func-

tion and advanced Green's function respectively.

3.2.2 Simplifying the Landauer Model

In order to compute the transmission function $\tau(E)$ for real molecules and electrode atoms, we need to simplify the Landauer model by making further approximations. These approximations to the Landauer model are briefly described in this section. Fig. 3.2 pictorially describes the approximations made to the Landauer model. Accordingly, the whole system is split into three separate regions namely (i) the left electrode L (ii) the central region C which encompasses the nanojunction and (iii) the right electrode R. The Hamiltonian of these regions are given by $\hat{H}_{LL}$ $\hat{H}_{CC}$ and $\hat{H}_{RR}$ respectively. We further assume that the central region is coupled to the semi-infinite electrode through localized potentials $\hat{V}_{LC}, \hat{V}_{LC}^{\dagger}$ and $\hat{V}_{CR}, \hat{V}_{CR}^{\dagger}$. The left and the right electrodes are assumed to not have any interaction. The total Hamiltonian $\hat{H}$ is given as

$$\hat{H} = \hat{H}_{CC} + \hat{H}_{LL} + \hat{H}_{CC} + \hat{V}_{LC} + \hat{V}_{LC}^{\dagger} + \hat{V}_{CR} + \hat{V}_{CR}^{\dagger} \tag{3.32}$$

The retarded Green's function of the Schrödinger's equation $\hat{G}^r(z)$ is given by (see Eq. 3.31)

$$\left(z - \hat{H}\right) \hat{G}^r(z) = \mathbb{1} \text{ where } \quad z = \lim_{\eta \to 0} E + i\eta \tag{3.33}$$

where $\mathbb{1}$ is the identity operator. Assuming there exists an orthonormal and spacially

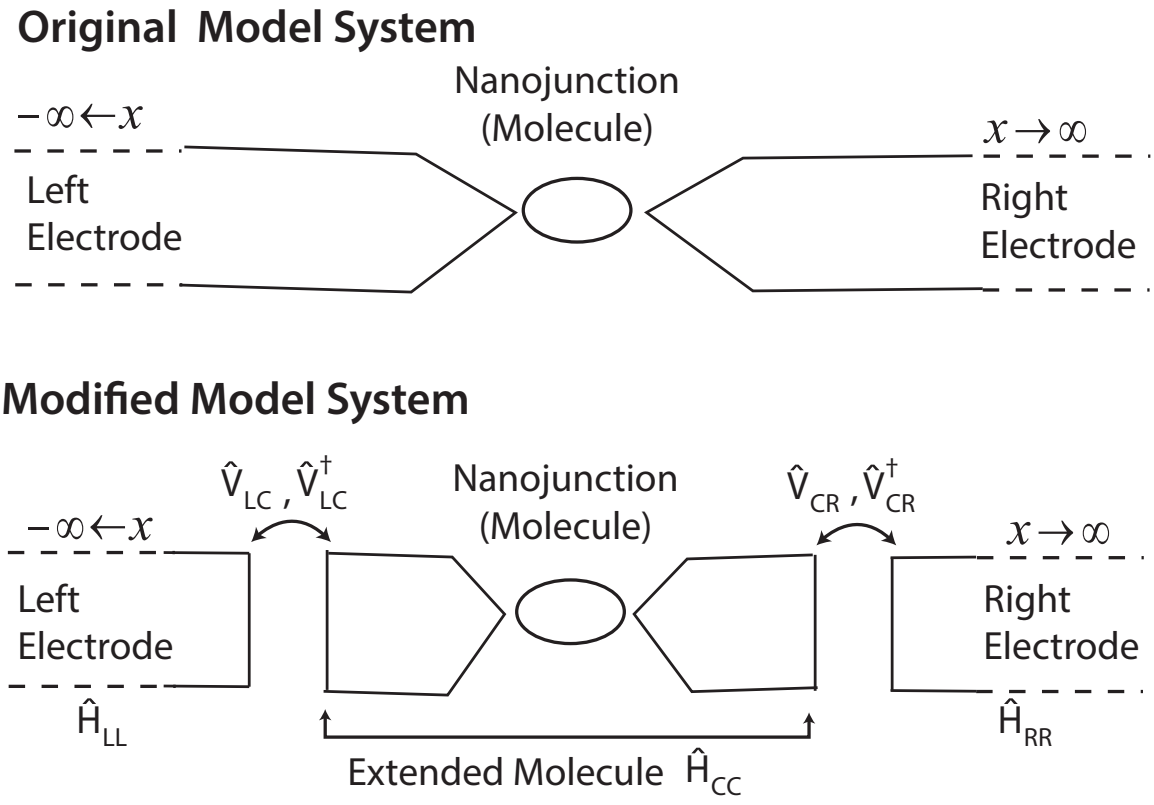

Figure 3.2: Approximations to Landauer Model. The system is broken down into three regions namely (i) the left electrode, (ii)the central region (or extended molecule) and (ii) the right electrode. The interaction between the central region (or extended molecule) and the metal electrodes is assumed to be localized. No interaction is assumed between the two metal electrodes.

localized basis set $\{|\phi_i\rangle\}$, the above equation can be rewritten in matrix form as

$$\left(z - \begin{bmatrix} \hat{H}_{LL} & \hat{V}_{LC} & 0 \\ \hat{V}^{\dagger}_{LC} & \hat{H}_{CC} & \hat{V}_{CR} \\ 0 & \hat{V}^{\dagger}_{CR} & \hat{H}_{RR} \end{bmatrix} \right) \begin{bmatrix} \hat{G}^{r}_{LL}(z) & \hat{G}^{r}_{LC}(z) & \hat{G}^{r}_{LR}(z) \\ \hat{G}^{r}_{CL}(z) & \hat{G}^{r}_{CC}(z) & \hat{G}^{r}_{CR}(z) \\ \hat{G}^{r}_{RL}(z) & \hat{G}^{r}_{RC}(z) & \hat{G}^{r}_{RR}(z) \end{bmatrix} = \begin{bmatrix} \mathbb{1}_{LL} & 0 & 0 \\ 0 & \mathbb{1}_{CC} & 0 \\ 0 & 0 & \mathbb{1}_{RR} \end{bmatrix} \tag{3.34}$$

The above system of equations can be solved to obtain the Green's function of the

central region $\left(G^r_{CC}(z)\right)$ in the presence of the left and right electrodes as,

$$\begin{aligned} \hat{G}^r_{CC}(z) &= \left(z - \hat{H}_{CC} - \hat{\Sigma}_L(z) - \hat{\Sigma}_R(z)\right)^{-1} \\ \hat{\Sigma}_L &= \hat{V}^\dagger_{LC}\left(z - \hat{H}_{LL}\right)^{-1}\hat{V}_{LC} \\ \hat{\Sigma}_R &= \hat{V}_{CR}\left(z - \hat{H}_{RR}\right)^{-1}\hat{V}^\dagger_{CR} \end{aligned} \tag{3.35}$$

The influence of the left and right electrodes on the central region (*aka* extended molecule EM) is quantified in the above expression through the corresponding self-energy operaators $\hat{\Sigma}_{L/R}(z)$. The Hermitian part of the self-energy operators $\left(\frac{\hat{\Sigma}_{L/R}(z)+\hat{\Sigma}^\dagger_{L/R}(z)}{2}\right)$ quantifies the shift in the molecular orbitals due to the influence of the electrodes while the anti-Hermitian part of the self-energy operators $\left(\frac{\hat{\Sigma}_{L/R}(z)-\hat{\Sigma}^\dagger_{L/R}(z)}{2}\right)$ quantifies the broadening of the molecular energy levels[18].

The transmission function $\tau(E)$ of the central region and in turn that of the nanojunction can now be calculated as[18]

$$\begin{aligned} \tau(E) &= Tr\left[\hat{\Gamma}_L(z)\hat{G}^r_{CC}(z)\hat{\Gamma}_R(z)\hat{G}^a_{CC}(z)\right] \\ \hat{\Gamma}_{L/R}(z) &= i\left[\hat{\Sigma}_{L/R}(z) - \hat{\Sigma}^\dagger_{L/R}\right] \end{aligned} \tag{3.36}$$

where $\hat{G}^a_{CC}(z)$ is advanced Green's function of the nanojunction. As discussed previously, $\hat{G}^a_{CC}(z)$ is just the complex conjugate of $\hat{G}^r_{CC}(z)$. The operators $\hat{\Gamma}_{L/R}(z)$—called as broadening operators constitute the anti-Hermitian part of the self-energy operators.

3.2.3 Self-energy of Semi-infinite Electrodes

The formalism requires the electrodes to be semi-infinite in nature which leads us to the question— *How to efficiently calculate the Green's function of a semi-infinite electrode employing a localized atom-centered basis set?* This question was answered by Lopez and co-workers[61] who devised an efficient recursive algorithm to calculate the Green's function of a semi-infinite electrode. Under this algorithm, the Hamitonian is assumed to be made up of perfectly repetitive principle layers with each principle layer containing *l* atoms and *m* basis-functions per atom. Further we also assume that all the principle layers interact only with the nearest neighbors in an identical fashion. These assumptions can be mathematically stated as

$$\begin{aligned} H_{00} &= H_{11} = ... = H_{ii} = ... \\ H_{01} &= H_{12} = ... = H_{i,i+1} = ... \\ H_{ij} &= 0 \; \forall j \;\; \notin (i-1, i, i+1) \end{aligned} \tag{3.37}$$

The block state of the principal layer 'n' $(\psi_n(k))$ containing l atoms and m basis-functions per atom can be represented in terms of the localized atom-centered basis set as

$$\psi_n(k) = \begin{bmatrix} \left|\phi_n^{11}(k)\right\rangle \\ . \\ . \\ \left|\phi_n^{\lambda\alpha}(k)\right\rangle \\ . \\ . \\ \left|\phi_n^{lm}(k)\right\rangle \end{bmatrix} \tag{3.38}$$

The Green's function of this electrode is given as

$$\left(z - \hat{H}\right) \hat{G}^r = \mathbb{1} \text{ where } \quad z = \lim_{\eta \to 0} E + i\eta \tag{3.39}$$

We write $\hat{G}^r(z)$ as $\hat{G}^r$ for notational simplicity. Acting the above Eq. on basis function $\left|\phi_0^{\lambda\alpha}(k)\right\rangle$, we get,

$$\left(z - \hat{H}\right) \hat{G}^r \left|\phi_0^{\lambda\alpha}(k)\right\rangle = \left|\phi_0^{\lambda\alpha}(k)\right\rangle. \tag{3.40}$$

Taking inner product of the above equation with another basis function of 0^{th} principle layer we get,

$$\left\langle \phi_0^{\bar{\lambda}\beta}(k) \right| \left(z - \hat{H}\right) \hat{G}^r \left|\phi_0^{\lambda\alpha}(k)\right\rangle = \delta_{\bar{\lambda}\lambda}\delta_{\beta\alpha}. \tag{3.41}$$

The identity operator for the semi-infinite block is given as

$$\mathbb{1} = \sum_{n'=0}^{\infty} \sum_{\lambda'=1}^{l} \sum_{\alpha'=1}^{m} \left|\phi_{n'}^{\lambda'\alpha'}(k)\right\rangle \left\langle \phi_{n'}^{\lambda'\alpha'}(k) \right|. \tag{3.42}$$

Inserting $\mathbb{1}$ in between $\hat{H}$ and $\hat{G}^r$ we get,

$$z \left\langle \phi_0^{\bar{\lambda}\beta}(k) \right| \hat{G}^r \left|\phi_0^{\lambda\alpha}(k)\right\rangle - \sum_{n'=0}^{\infty} \sum_{\lambda'=1}^{l} \sum_{\alpha'=1}^{m} \left\langle \phi_0^{\bar{\lambda}\beta}(k) \right| H \left|\phi_{n'}^{\lambda'\alpha'}(k)\right\rangle \left\langle \phi_{n'}^{\lambda'\alpha'}(k) \right| \hat{G}^r \left|\phi_0^{\lambda\alpha}(k)\right\rangle = \delta_{\bar{\lambda}\lambda}\delta_{\beta\alpha}. \tag{3.43}$$

Since the Hamiltonian is assumed to be tight binding, the only non zero coefficients are those for $n' = 0, 1$ which simplifies the above equation as,

$$z\left\langle \phi_0^{\bar{\lambda}\beta}(k)\right| \hat{G}^r \left|\phi_0^{\lambda\alpha}(k)\right\rangle - \sum_{\lambda'=1}^{l}\sum_{\alpha'=1}^{m}\Big\{\left\langle \phi_0^{\bar{\lambda}\beta}(k)\right| H \left|\phi_0^{\lambda'\alpha'}(k)\right\rangle \left\langle \phi_0^{\lambda'\alpha'}(k)\right| \hat{G}^r \left|\phi_0^{\lambda\alpha}(k)\right\rangle + \left\langle \phi_0^{\bar{\lambda}\beta}(k)\right| H \left|\phi_1^{\lambda'\alpha'}(k)\right\rangle \left\langle \phi_1^{\lambda'\alpha'}(k)\right| \hat{G}^r \left|\phi_0^{\lambda\alpha}(k)\right\rangle\Big\} = \delta_{\bar{\lambda}\lambda}\delta_{\beta\alpha}. \tag{3.44}$$

The above equation can be written in compact matrix form as

$$z\hat{G}^r_{00} - H_{00}\hat{G}^r_{00} - H_{01}\hat{G}^r_{10} = I \tag{3.45}$$

Take inner product of Eq. 3.40 with a basis function of the 1^{st} principle layer we get,

$$\left\langle \phi_1^{\bar{\lambda}\beta}(k)\right| \left(z - \hat{H}\right) \hat{G}^r \left|\phi_0^{\lambda\alpha}(k)\right\rangle = 0. \tag{3.46}$$

Similar to Eq. 3.45 we insert $\mathbb{1}$ operator in between $\hat{H}$ and $\hat{G}^r$ and assume tight binding interaction and we get,

$$z\left\langle \phi_1^{\bar{\lambda}\beta}(k)\right| \hat{G}^r \left|\phi_0^{\lambda\alpha}(k)\right\rangle - \sum_{\lambda'=1}^{l}\sum_{\alpha'=1}^{m}\Big\{\left\langle \phi_1^{\bar{\lambda}\beta}(k)\right| H \left|\phi_0^{\lambda'\alpha'}(k)\right\rangle \left\langle \phi_0^{\lambda'\alpha'}(k)\right| \hat{G}^r \left|\phi_0^{\lambda\alpha}(k)\right\rangle + \left\langle \phi_1^{\bar{\lambda}\beta}(k)\right| H \left|\phi_1^{\lambda'\alpha'}(k)\right\rangle \left\langle \phi_1^{\lambda'\alpha'}(k)\right| \hat{G}^r \left|\phi_0^{\lambda\alpha}(k)\right\rangle + \left\langle \phi_1^{\bar{\lambda}\beta}(k)\right| H \left|\phi_2^{\lambda'\alpha'}(k)\right\rangle \left\langle \phi_2^{\lambda'\alpha'}(k)\right| \hat{G}^r \left|\phi_0^{\lambda\alpha}(k)\right\rangle\Big\} = 0. \tag{3.47}$$

The above equation can be written in compact matrix form as

$$z\hat{G}^r_{10} - H_{10}\hat{G}^r_{00} - H_{11}\hat{G}^r_{10} - H_{12}\hat{G}^r_{20} = 0 \tag{3.48}$$

Using the relationships $H_{11} = H_{00}$ (due to identical principle layer), $H_{12} = H_{01}$ (due to identical tight binding interaction) and $H_{10} = H_{01}^{\dagger}$ (due to hermiticity of Hamiltonian), we can rewrite the above Eq. as

$$(z - H_{00})\,\hat{G}^r_{10} = H_{01}^{\dagger}\hat{G}^r_{00} + H_{01}\hat{G}^r_{20} \tag{3.49}$$

Substituting Eq. 3.49 in Eq. 3.45 we get,

$$\left(z - H_{00} - H_{01}\,(z - H_{00})^{-1}\,H_{01}^{\dagger}\right)\hat{G}^r_{00} = I + H_{01}\,(z - H_{00})^{-1}\,H_{01}\hat{G}^r_{20} \tag{3.50}$$

The above equation provides a nice explicit relationship that relates the $\hat{G}^r_{00}$ to $\hat{G}^r_{20}$.

The Eq. 3.49 can be generalized to an arbitrary n^{th} principle layer if we take the inner product of Eq. 3.40 with a basis function of the n^{th} principle layer $(n \neq 0)$ and we get

$$(z - H_{00})\,\hat{G}^r_{n,0} = H_{01}^{\dagger}\hat{G}^r_{n-1,0} + H_{01}\hat{G}^r_{n+1,0} \tag{3.51}$$

The Green's function of an arbitrary n^{th} principle layer $\left(\hat{G}^r_{n,n}\right)$ can be obtained by acting Eq. 3.39 on basis function of the n^{th} principle layer $\left|\phi_n^{\lambda\alpha}(k)\right\rangle$ and taking inner product with another basis function of the same layer $\left|\phi_n^{\bar{\lambda}\beta}(k)\right\rangle$ and we get

$$\begin{aligned}\Big(z - H_{00} - H_{01}\,(z - H_{00})^{-1}\,H_{01}^{\dagger} - H_{01}^{\dagger}\,(z - H_{00})^{-1}\,H_{01}\Big)\,\hat{G}^r_{n,n} \\ = I + H_{01}^{\dagger}\,(z - H_{00})^{-1}\,H_{01}^{\dagger}\hat{G}^r_{n-2,n} + H_{01}\,(z - H_{00})^{-1}\,H_{01}\hat{G}^r_{n+2,n}\end{aligned} \tag{3.52}$$

Similarly the generalization of the Eq. 3.50 yields,

$$\left(z - H_{00} - H_{01}\left(z - H_{00}\right)^{-1} H_{01}^{\dagger} - H_{01}^{\dagger}\left(z - H_{00}\right)^{-1} H_{01}\right) \hat{G}_{n,0}^{r}$$
$$= H_{01}^{\dagger}\left(z - H_{00}\right)^{-1} H_{01}^{\dagger} \hat{G}_{n-2,0}^{r} + H_{01}\left(z - H_{00}\right)^{-1} H_{01} \hat{G}_{n+2,0}^{r} \tag{3.53}$$

Eqs. 3.50, 3.52 and 3.53 can be more compactly rewritten as

$$\left(z - \epsilon_{1,s}\right) \hat{G}_{00}^{r} = I + \alpha_1 \hat{G}_{20}^{r} \tag{3.54}$$

$$\left(z - \epsilon_{1}\right) \hat{G}_{n,0}^{r} = \beta_1 \hat{G}_{n-2,0}^{r} + \alpha_1 \hat{G}_{n+2,0}^{r} \tag{3.55}$$

$$\left(z - \epsilon_{1}\right) \hat{G}_{n,n}^{r} = I + \beta_1 \hat{G}_{n-2,0}^{r} + \alpha_1 \hat{G}_{n+2,0}^{r}, \tag{3.56}$$

where

$$\alpha_1 = H_{01}\left(z - H_{00}\right)^{-1} H_{01}$$
$$\beta_1 = H_{01}^{\dagger}\left(z - H_{00}\right)^{-1} H_{01}^{\dagger}$$
$$\epsilon_{1,s} = H_{00} + H_{01}\left(z - H_{00}\right)^{-1} H_{01}^{\dagger}$$
$$\epsilon_1 = H_{00} + H_{01}\left(z - H_{00}\right)^{-1} H_{01}^{\dagger} + H_{01}^{\dagger}\left(z - H_{00}\right)^{-1} H_{01}$$

Considering only the even numbered principle layers $(n = 2k)$ Eq. 3.54 can be rewritten as

$$\left(z - \epsilon_{1,s}\right) \hat{G}_{00}^{r} = I + \alpha_1 \hat{G}_{20}^{r} \tag{3.57}$$

$$\left(z - \epsilon_{1}\right) \hat{G}_{2k,0}^{r} = \beta_1 \hat{G}_{2(k-1),0}^{r} + \alpha_1 \hat{G}_{2(k+1),0}^{r} \tag{3.58}$$

$$\left(z - \epsilon_{1}\right) \hat{G}_{2k,2k}^{r} = I + \beta_1 \hat{G}_{2(k-1),0}^{r} + \alpha_1 \hat{G}_{2(k+1),0}^{r}, \tag{3.59}$$

Thus above set of Equations can be effectively algorithmized into an iteration of calculating $\hat{G}^r_{2k,0}$, to ensure that in every iteration we double the number of effective principle layers $(k_i = 2k_{i-1})$ captured by the Green's function. The iterative algorithm can be concisely stated as

$$\alpha_i = \alpha_{i-1} \left(z - \epsilon_{i-1}\right)^{-1} \alpha_{i-1} \tag{3.60}$$

$$\beta_i = \beta_{i-1} \left(z - \epsilon_{i-1}\right)^{-1} \beta_{i-1} \tag{3.61}$$

$$\epsilon_i = \epsilon_{i-1} + \alpha_{i-1} \left(z - \epsilon_{i-1}\right)^{-1} \beta_{i-1} + \beta_{i-1} \left(z - \epsilon_{i-1}\right)^{-1} \alpha_{i-1} \tag{3.62}$$

$$\epsilon_{i,s} = \epsilon_{i-1,s} + \alpha_{i-1} \left(z - \epsilon_{i-1}\right)^{-1} \beta_{i-1} \tag{3.63}$$

where the initial values are $\epsilon_0 = \epsilon_{0,s} - H_{00}$, $\alpha_0 = H_{01}$ and $\beta_0 = H^{\dagger}_{01}$.

3.2.4 Green's Function and Density of States

The Density of States (DoS) is defined as the number of available states per interval of energy that can be occupied by the electrons. It can be mathematically denoted as

$$DoS(E) = \frac{dN}{dE}$$

The DoS when integrated along with the Fermi-Dirac distribution (that determines the probability of an electron to occupy an energy level) provides the total number of electrons in the system

$$N_e = \int_{-\infty}^{\infty} DoS(E) f(E - \mu) dE \tag{3.64}$$

where N_e is the number of electrons. Now we can express the DoS as a function of the retarded Green's function $\hat{G}^r(z)$ which can be used to calculate the total DoS and the localized DoS (DoS on a particular location like molecule). The Green's function of a system is given by

$$\hat{G}^r(z) = \lim_{\eta \to 0} \frac{1}{z - \hat{H}}$$

$$\text{Inserting } \mathbb{1} = \sum_n |\psi_n\rangle \langle\psi_n|$$

$$\hat{G}^r(z) = \lim_{\eta \to 0} \sum_n \frac{1}{z - E_n} |\psi_n\rangle \langle\psi_n|$$

From theory of distributions[26], we can prove that

$$\lim_{\eta \to 0} \left\langle \frac{1}{x + i\eta - x_0}, \phi \right\rangle = P \left\langle \left(\frac{1}{x - x_0} \right), \phi \right\rangle - i\pi \langle \delta(x - x_0), \phi \rangle \tag{3.65}$$

where ϕ is an infinitely differentiable (C_∞) function with compact support. $\langle \cdot, \cdot \rangle$ indicates the action of the functional (on the left hand side) on the test function ϕ, which in this case in an integral over the R^3 domain. $P \langle \cdot, \cdot \rangle$ is the principal integral value of the functional. Using the above expression we can obtain the imaginary part of $\hat{G}^r(z)$ as,

$$-\frac{1}{\pi} Im \left(\hat{G}^r(z) \right) = \sum_n \delta (E - E_n) |\psi_n\rangle \langle\psi_n| \tag{3.66}$$

Integrating the imaginary part of $\hat{G}^r(z)$ along with the Fermi-Dirac distribution over the entire energy we get

$$-\frac{1}{\pi}\int_{-\infty}^{\infty} Im\left(\hat{G}^r(z)\right) f(E-\mu)dE = \int_{-\infty}^{\infty}\sum_n \delta\left(E-E_n\right)|\psi_n\rangle\langle\psi_n| f(E-\mu)dE \quad (3.67)$$

$$= \sum_n f(E-\mu)|\psi_n\rangle\langle\psi_n| \quad (3.68)$$

$$= \hat{\rho} \quad (3.69)$$

where $\hat{\rho}$ is the first order density matrix. We also know that the trace of the $\hat{\rho}$ will gives us the number of electrons

$$-\frac{1}{\pi}\int_{-\infty}^{\infty} Tr\left[Im\left(\hat{G}^r(z)\right) f(E-\mu)\right] dE = Tr\left[\hat{\rho}\right] = N_e \quad (3.70)$$

$$\int_{-\infty}^{\infty} -\frac{1}{\pi} Tr\left[Im\left(\hat{G}^r(z)\right)\right] f(E-\mu)dE = N_e \quad (3.71)$$

Comparing the above equation with Eq. 3.64 we can obtain an explicit expression for DoS as a function of $\hat{G}^r(z)$ as

$$DoS(E) = -\frac{1}{\pi} Tr\left[Im\left(\hat{G}^r(z)\right)\right] \quad (3.72)$$

For a localized basis set, the DoS over a specific subdomain S of the system can be obtained by performing the trace operation only over the basis functions that have a non-zero compact support over the subdomain S.

3.2.5 Non Orthogonal Basis Set

All the equations derived in this chapter assumed that the basis functions are orthogonal. However the most common basis set used in the transport community is the linear combination of atomic orbitals (LCAO) basis set which is not orthogonal in nature. In this section we describe how the equations transform in a non-orthogonal basis set.

The Green's function $\hat{G}^r(z)$ corresponding to a Hamiltonian $\hat{H}$ system can be expressed in a non-orthogonal basis set as

$$\hat{G}^r(z) = \lim_{\eta \to 0} \left(zS - \hat{H}\right)^{-1} \tag{3.73}$$

where S is the overlap matrix and its components are defined as

$$S_{ij} = \int_{\Omega} \phi_i(\boldsymbol{x}) \phi_j(\boldsymbol{x}) d\boldsymbol{x} \tag{3.74}$$

The Green's function of the central region $\hat{G}^r_{CC}(z)$ in the presence of semi-infinite electrodes (L,R) is given as

$$\hat{G}^r_{CC}(z) = \left(zS - \hat{H}_{CC} - \hat{\Sigma}_L(z)\hat{\Sigma}_R(z)\right)^{-1} \tag{3.75}$$

$$\hat{\Sigma}_L(z) = \left(zS_{LC} - \hat{V}_{LC}\right)^{\dagger} \hat{g}_{LL} \left(zS_{LC} - \hat{V}_{LC}\right) \tag{3.76}$$

$$\hat{\Sigma}_R(z) = \left(zS_{CR} - \hat{V}_{CR}\right) \hat{g}_{RR} \left(zS_{CR} - \hat{V}_{CR}\right)^{\dagger} \tag{3.77}$$

The equation relating the transmission function $(\tau(E))$ to the $\hat{G}^r_{CC}(z)$ and $\hat{\Sigma}_{L/R}(z)$ (see Eq. 3.36) remains unmodified but the equation relating DoS to the $\hat{G}^r_{CC}(z)$ is

given by

$$DoS(E) = -\frac{1}{\pi} Tr\left[Im\left(\hat{G}^r(z)S\right)\right] \tag{3.78}$$

3.3 Computational Model

3.3.1 Density Functional Theory

The Hamiltonian of the electrodes and that of the extended molecule needs to be numerically computed in order to compute the transmission function $\tau(E)$. The Kohn-Sham density functional theory (KS-DFT) is one of the most commonly used quantum mechanical formalism to efficiently compute the ground-state energy and in turn the ground-state properties of a wide range of materials properties. The KS-DFT approach can also be used to compute the Hamiltonian of a material system. The KS-DFT approach is based on the key result of Hohenberg & Kohn[30] that proved that the ground-state energy can be expressed as a unique functional of electron density. However, the actual functional form of this representation is not known. This challenge was addressed in an approximate sense by Kohn & Sham[37] that enabled the usage of KS-DFT approach to study real material systems. In this section, we closely follow the Motamarri *et.al*[44] in briefly describing the Kohn-Sham approach of reducing the original problem of many-body interacting electrons into an equivalent problem of non-interacting electrons in an effective mean field to compute the ground-state electronic-structure of the heterojunction.

3.3.1.1 Kohn-Sham variational problem

The Kohn-Sham energy functional (neglecting spin) that describes a material system consisting of N electrons and M nuclei system is given by[49,22]

$$E(\boldsymbol{\Psi}, \boldsymbol{R}) = T_s(\boldsymbol{\Psi}) + E_{xc}(\rho, \nabla\rho) + E_H(\rho) + E_{ext}(\rho, \boldsymbol{R}) + E_{zz}(\boldsymbol{R}) \tag{3.79}$$

where

$$\rho(\boldsymbol{r}) = \sum_{i=1}^{N} |\psi_i(\boldsymbol{x})|^2 \tag{3.80}$$

represents the electron density. In the above expression, the spatial coordinates are represented by $\boldsymbol{r}$, whereas $\boldsymbol{x} = (\boldsymbol{r}, s)$ includes both the spatial and spin degrees of freedom. $\boldsymbol{\Psi} = \{\psi_1(\boldsymbol{x}), \psi_2(\boldsymbol{x}), \cdots, \psi_N(\boldsymbol{x})\}$ denotes the vector of orthonormal single electron wavefunctions, where each wavefunction $\psi_i \in \mathbb{X} \times \{\alpha, \beta\}$ can in general be complex-valued, and comprises of a spatial part belonging to a suitable function space $\mathbb{X}$ and a spin state denoted by $\alpha(s)$ or $\beta(s)$. We denote by $\boldsymbol{R} = \{\boldsymbol{R}_1, \boldsymbol{R}_2, \cdots \boldsymbol{R}_M\}$ the collection of all nuclear positions.

The first term in the Kohn-Sham energy functional in (3.79), $T_s(\boldsymbol{\Psi})$, denotes the kinetic energy of non-interacting electrons and is given by

$$T_s(\boldsymbol{\Psi}) = \sum_{i=1}^{N} \int \psi_i^*(\boldsymbol{x}) \left(-\frac{1}{2}\nabla^2\right) \psi_i(\boldsymbol{x})\, d\boldsymbol{x} \tag{3.81}$$

where ψ_i^* denotes the complex conjugate of ψ_i.

The electrostatic interaction energies in the Kohn-Sham energy functional in (3.79) are given by

$$E_H(\rho) = \frac{1}{2} \int \int \frac{\rho(\boldsymbol{r})\rho(\boldsymbol{r}')}{|\boldsymbol{r} - \boldsymbol{r}'|}\, d\boldsymbol{r}\; d\boldsymbol{r}' \tag{3.82}$$

$$E_{ext}(\rho, \boldsymbol{R}) = \int \rho(\boldsymbol{r}) V_{ext}(\boldsymbol{r}, \boldsymbol{R})\, d\boldsymbol{r} = \sum_J \int \rho(\boldsymbol{r}) V_J(\boldsymbol{r}, \boldsymbol{R}_J)\, d\boldsymbol{r} \tag{3.83}$$

$$E_{zz} = \frac{1}{2} \sum_{I, J \neq I} \frac{Z_I Z_J}{|\boldsymbol{R}_I - \boldsymbol{R}_J|} \tag{3.84}$$

where E_H is the Hartree energy representing the classical electrostatic interaction energy between electrons, E_{ext} is the interaction energy between electrons and the external potential induced by the nuclear charges given by $V_{ext} = \sum_J V_J(\boldsymbol{r}, \boldsymbol{R}_J)$ with V_J denoting the potential (singular Coulomb potential or local pseudopotential) contribution from the J^{th} nucleus, and E_{zz} denotes the repulsive energy between nuclei with Z_I denoting the charge on the I^{th} nucleus. We note that in a non-periodic setting, representing a finite atomic system, all the integrals in equations (3.81)-(3.83) are over $\mathbb{R}^3$ and the summations in (3.83)-(3.84) include all the atoms I and J in the system. In the case of an infinite periodic crystal, all the integrals over $\boldsymbol{r}$ in equations (3.81)-(3.83) extend over the unit cell, whereas the integrals over $\boldsymbol{r}'$ extend in $\mathbb{R}^3$. Similarly, in (3.83)-(3.84) the summation over I is on the atoms in the unit cell, and summation over J extends over all lattice sites. We note that, in the context of periodic problems, the above expressions assume a single k-point ($\Gamma-$point) sampling. The computation of the electron density and kinetic energy in (3.80) and (3.81) for multiple k-point sampling involves an additional quadrature over the k-points in the Brillouin zone (cf. e.g[22]).

E_{xc} in the energy functional equation denotes the exchange-correlation energy that describes the quantum-mechanical many body interactions between electrons. The exact functional form of E_{xc} is unknown and hence various approximations are employed to describe these quantum mechanical interactions. The most simplest approximation is to describe the exchange-correlation energy functional to de-

pend solely on the electron density ($E_{xc}(\rho)$). This class of approximation is called as the local density approximation (LDA), has been successfully used in describing metallic systems whose electron density changes very slowly. The next extension to describe these quantum-mechanical interactions is to describe the exchange-correlation energy functional to depend on both the electron density and its derivative ($E_{xc}(\rho, \nabla\rho)$). This class of approximation is called as the generalized gradient approximation (GGA), has been successfully used in describing finite systems such as molecular geometry.

One of the major issues in DFT level approximation is the electronic-self interactions. Unlike Hartree-Fock, where the electronic self interactions get exactly cancelled out between the electrostatic and exchange terms, the KS-DFT contains electronic self-interactions. These self-interaction errors in KS-DFT results in model inaccuracies that particularly affect the computation the LUMO energy level (or conduction band in a solid). One of the straight forward ways to reduce this self-interaction error is to incorporate a portion of exact exchange from Hartree-Fock theory with the KS-DFT exchange and correlation. This approximation, commonly referred as the hybrid exchange-correlation enables to improve the accuracy of predicting the LUMO energy level (or conduction band) or a material system. In this work we use one of the famous hybrid exchange-correlation functional B3LYP[7,6], which has been used by various researchers in predicting the electronic structure of various molecules and metal-molecule heterojunctions.

Subsequently, the problem of determining the ground-state energy and electron density for given positions of nuclei can be expressed as the following variational problem:

$$\inf_{\boldsymbol{\Psi}\in\mathcal{X}} E(\boldsymbol{\Psi}, \boldsymbol{R}) \tag{3.85}$$

where $\mathcal{X} = \left\{ \boldsymbol{\Psi} \,|\, \langle \psi_i, \psi_j \rangle_{\mathbb{X}\times\{\alpha,\beta\}} = \delta_{ij} \right\}$ with $\langle\ ,\ \rangle_{\mathbb{X}\times\{\alpha,\beta\}}$ denoting the inner product defined on $\mathbb{X} \times \{\alpha, \beta\}$. $\mathbb{X}$ denotes a suitable function space that guarantees the existence of minimizers.

3.3.1.2 Kohn-Sham eigenvalue problem

The stationarity condition corresponding to the Kohn-Sham variational problem is equivalent to the non-linear Kohn-Sham eigenvalue problem given by:

$$\mathcal{H}\psi_i = \epsilon_i \psi_i \tag{3.86}$$

where

$$\mathcal{H} = \left(-\frac{1}{2}\nabla^2 + V_{\text{eff}}(\rho, \boldsymbol{R}) \right) \tag{3.87}$$

is the Hamiltonian operator with eigenvalues ϵ_i, and the corresponding orthonormal eigenfunctions ψ_i for $i = 1, 2, \cdots, N$ denote the canonical wavefunctions. The electron density in terms of the canonical wavefunctions is given by

$$\rho(\boldsymbol{r}) = \sum_{i=1}^{N} |\psi_i(\boldsymbol{x})|^2 \tag{3.88}$$

and the effective single-electron potential, $V_{\text{eff}}(\rho, \boldsymbol{R})$, in (3.87) is given by

$$V_{\text{eff}}(\rho, \boldsymbol{R}) = V_{ext}(\boldsymbol{R}) + V_H(\rho) + V_{xc}(\rho) = V_{ext}(\boldsymbol{R}) + \frac{\delta E_H}{\delta \rho} + \frac{\delta E_{xc}}{\delta \rho} \tag{3.89}$$

It is efficient to compute the total electrostatic potential, defined as the sum of the external potential ($V_{ext}(\boldsymbol{R})$) and the Hartree potential ($V_H(\rho)$), through the solution

of a Poisson equation

$$-\frac{1}{4\pi}\nabla^2\phi(\boldsymbol{r},\boldsymbol{R}) = \rho(\boldsymbol{r}) + b(\boldsymbol{r},\boldsymbol{R})$$

which is given by

$$\phi(\boldsymbol{r},\boldsymbol{R}) \equiv V_H(\rho) + V_{ext}(\boldsymbol{r},\boldsymbol{R}) = \int \frac{\rho(\boldsymbol{r'})}{|\boldsymbol{r}-\boldsymbol{r'}|}\,d\boldsymbol{r'} + \int \frac{b(\boldsymbol{r'},\boldsymbol{R})}{|\boldsymbol{r}-\boldsymbol{r'}|}\,d\boldsymbol{r'} \tag{3.90}$$

where $b(\boldsymbol{r},\boldsymbol{R})$ describes the nuclear charge distribution. Finally, the system of equations corresponding to the Kohn-Sham eigenvalue problem are given by

$$\left(-\frac{1}{2}\nabla^2 + V_{\text{eff}}(\rho,\boldsymbol{R})\right)\psi_i = \epsilon_i\psi_i \tag{3.91a}$$

$$\rho(\boldsymbol{r}) = \sum_{i=1}^{N} |\psi_i(\boldsymbol{x})|^2 \tag{3.91b}$$

$$-\frac{1}{4\pi}\nabla^2\phi(\boldsymbol{r},\boldsymbol{R}) = \rho(\boldsymbol{r}) + b(\boldsymbol{r},\boldsymbol{R})\ ; \qquad V_{\text{eff}}(\rho,\boldsymbol{R}) = \phi(\boldsymbol{r},\boldsymbol{R}) + \frac{\delta E_{xc}}{\delta\rho} \tag{3.91c}$$

which have to be solved self-consistently with appropriate boundary conditions based on the problem under consideration. In the case of a periodic crystal, the effective potential V_{eff} has the periodicity of the lattice and the solutions of the Kohn-Sham eigenvalue problem are given by the Bloch theorem[(2)]. Thus, for periodic systems, it is computationally efficient to compute the Bloch solutions directly, whereas in case of a finite system or systems where we are interested in local electronic-structure, it is better off to use a localized basis set.

Since, in this work we are interested in understanding the influence of Au electrode atoms on the molecular electronic-structure, we need a basis set that is spa-

tially localized which can capture this influence. It is for this reason, we use atom centered linear combination of atomic orbitals (LCAO) basis set in this work. In particular, we use LANL2DZ[28,76,27] basis set in this work. Most of the chemical interactions are due to the valence electrons of different atoms interacting with one another. Hence, for computational efficiency we can approximate the core electrons through an effective potential called as pseudopotential. The LANL2DZ basis set used in this work, also provides the pseudopotential approximation for the core electrons of the Au atoms.

3.3.2 System Geometry

The first important computational model decision that we have to make to employ the Landauer formalism to compute MMMJ transport properties is the decision pertaining to system geometry. The most common way to model the central region of the system is to incorporate a few metal atoms (Au in this case) along with the molecule. Adding Au atoms to the central region increases the length of the central region which in turn ensures the model constrain that the left and the right electrode must have no interaction. Further, adding Au atoms also enables us to systematically define the localized coupling potentials $\left(\hat{V}_{LC}, \hat{V}_{CR}\right)$ between the central region and the semi-infinite electrodes. The typical central region from which the Hamiltonian $\hat{H}_{CC}$ is calculated is shown in Fig. 3.3(a). Here, the central region comprises of four layers of Au atoms arranged in the $\langle 111 \rangle$ plane direction. The central region is also called as the extended molecule and we will use both these terminologies interchangeably in the remainder of this dissertation.

The next important model decision is to determine how the molecular end-group makes contact with Au electrode atoms to form a chemical bond. Since, we have

very little experimental information on this interaction, the model decisions are driven by energy minimization through computational modeling. In this work, we consider three different contact models, namely the top-site, hollow-site and atop-trimer to model the molecular adsorption on the Au atoms. A schematic picture of these contact models are provided in Fig. 3.4.

As described in the previous section, the Hamiltonian of the central region is calculated within the density functional theory (DFT) approximation. Hybrid B3LYP exchange-correlation functional[7,6] and Los Alamos basis set with a double zeta split for valence electrons[28](LANL2DZ) and its corresponding effective core potential was employed for all the electronic-structure calculations. The DFT calculations were performed employing the quantum chemistry software Q-Chem[62]. The geometry of the aromatic molecules of interest $(SS1-SS4, S1-S4, (NC))_2\,3)$ is first optimized employing DFT calculations. Upon optimization, the contact model that binds the molecular end-group to the Au atoms (top, hollow or a-top) is determined by comparing the binding energies and selecting the configuration with the highest binding energy. The geometry of the molecules are further optimized in the presence of Au atoms (while keeping the positions of Au atoms fixed). In all optimizations the vibrational frequencies were considered to confirm that the structures correspond to minima in the potential surface. The Hamiltonian of this optimized central region (extended molecule) $\hat{H}_{CC}$ is now calculated within the DFT approximation.

As discussed previously, we need to calculate H_{00} and H_{01} of the principle layers which can then be used in the iterative algorithm (see Eq. 3.60) to calculate the surface Green's function of the left $\hat{g}_{LL}(z)$ and right $\hat{g}_{RR}(z)$ electrodes. To compute H_{00} and H_{01}, we consider a Au cluster with five $\langle 111 \rangle$ with each plane containing six

atoms each as shown in Figs. 3.3(c) and (d). Figs.3.3(c) and (d) also schematically explains how H_{00} and H_{01} is extracted from this cluster calculation. The coupling potential that couples the central region (extended molecule) to the left and right electrodes $\hat{V}_{LC}$, $\hat{V}_{CR}$ are assumed to be the same as H_{01} obtained from the Au cluster calculation. Upon calculating the electrode Green's function and the coupling potentials, we can calculate the self-energy operators $\hat{\Sigma}_{L/R}(z)$ from Eq. 3.75. In our calculations, the self energy operators of the electrodes are computed only at E_F, which is commonly referred to as the wide band scheme and has been shown to be a good approximation for MMMJs created from Au electrodes with density of states dominated by the *s* band[72].

We need to add the $\hat{\Sigma}_{L/R}(z)$ to $\hat{H}_{CC}$ to calculate $\hat{G}^r_{CC}(z)$ (see Eq. 3.75). However adding the computed self-energies on the $\hat{H}_{CC}$ sub-block that represents the last layer of the central region (extended molecule) results in inaccurate values due to the surface effects on the central region. To remove these surface effects, we project the Hamiltonian computed from the 4 layer central region onto a central region (extended molecule) with one Au layer as shown in Fig. 3.3(b). Adding the self-energy to the sub-block of this projected Hamiltonian ensures that most of the errors arising from the surface effects are effectively removed. Upon calculating $\hat{G}^r_{CC}(z)$, we can calculate the MMMJ transmission function $\tau(E)$ from Eq. 3.36.

3.4 Results & Discussion

3.4.1 Dithiol based MMMJs

The above computational model was employed to compute the transmission functions, $\tau(E)$, for the MMMJs based on dithiol molecules (SS1-SS3 - see Fig. 2.2).

In this model, we assumed that the thiol end-group deprotonated upon contact with Au atoms[83]. Further it was observed that the hollow-site was the most stable contact model through which the sulfur atom binded with the Au atoms of the central region (extended molecule). The computed $\tau(E)$ for these dithiol based MMMJs are shown in Fig. 3.5(a). The transmission at Fermi energy (E_F) decreases rapidly as the length of the molecules is increased, in turn explaining the sharp increase in the resistance of the MMMJs observed experimentally (see Fig. 2.3(a)). The Seebeck coefficients (thermopower) of the MMMJs can be calculated from $\tau(E)$ as,

$$S = -\frac{\Delta V}{\Delta T} = -\frac{\pi^2 k_B^2 T_A}{3|e|}\frac{1}{\tau(E)}\frac{\partial \tau(E)}{\partial E}\Big|_{E=E_F}.$$

As we could observe from this equation, the magnitude of thermopower is directly proportional to the slope of $\tau(E)$ at E_F. Further its sign is the negative of the sign of the $\tau(E)$ slope at E_F. To illustrate it further, Fig. 3.5(a) shows that for all dithiol terminated molecules, the slope of $\tau(E)$ at E_F is negative. Hence, based on the previous equation we should expect a positive thermopower similar to those observed experimentally. The computed Seebeck coefficients and the corresponding measured values are provided in Table 3.1. Here, the linear increase of the Seebeck coefficient with the number of rings, is consistent with the experimental observation and other recent computational studies[36,52]. The deviations between experiment and modeling may be due to the microscopic variations in the contact details, which are not addressed by the computational model. Further, molecular vibrations could cause the benzene rings in the molecules to deviate from their equilibrium alignments potentially altering its thermopower. These vibrational effects on the transport properties were also not considered in this present study.

3.4.2 Monothiol based MMMJs

The $\tau(E)$ values were similarly calculated for mono-thiol based MMMJs (S1-S4 -see Fig. 2.2). Similar to dithiol molecules, the thiol end-group is assumed to have deprotonated upon contact with Au atoms and the sulfur atoms binds to the Au cluster through a hollow-site. However, on the H end, the top-site was the more energetically favorable contact model. The computed $\tau(E)$ for these dithiol based MMMJs are shown in Fig. 3.5(b). The value of $\tau(E)$ at E_F is much lower compared to the dithiol molecules with the same number of phenyl rings. This indicates the higher resistance to electronic transport in monothiol based MMMJs due to the very weak coupling between the H (of phenyl ring) and Au atoms. This effect was also measured experimentally by our collaborators (see Fig. 2.3). From Fig. 3.5(b), we could also observe that similar to dithiols, the value of the transmission function at E_F drops exponentially with increasing molecular length. To quantify this effect, we fit the computed values of the low bias electrical resistance of the molecular junctions (using Eq. 3.14) to an exponentially decaying function $(R \propto exp(-\beta L))$. Specifically we find that $\beta = 0.3\text{Å}^{-1}$ fits well with the computational data. This value of β matches well with the experimentally obtained value of $\beta = 0.22 \pm 0.10\text{Å}^{-1}$.

The computed values of the thermopower for dithiol based MMMJs are provided in Table 3.1 and are in reasonable agreement with the experimentally measured values validating the models used in the computations. As we had discussed in chapter II, although the electrical resistance of the monothiols is more than an order higher when compared to dithiols, their thermopower values are very similar to dithiols which is attributed to the strength of the contact couplings[51]. Accordingly, the $\tau(E)$ of the weakly bound junction is related to the transmission of a strongly

bound junction by a scaling factor ($c > 0, c << 1$):

$$\tau(E)_{weak} = c\tau(E)_{strong}$$

Employing the above approximation, the electrical conductance of the weakly bound MMMJ is much lower compared to the strongly bound systems but their thermopower (given by Eq. 3.20) is the same for both the systems.

The other important question which arises from TVS experimental measurements of monothiol based MMMJs that needs to be addressed is: *Why does the energetic separation decrease with increasing length for the molecular junctions studied here?* In the introduction we had discussed that the energetic separation between the frontier molecular orbital (HOMO/LUMO) and E_F depends on two important factors namely (a) the energy levels of the isolated molecular system, and (b) the shift in the energy levels upon the creation of molecular junctions (see Fig. 1.4). To determine the origins of the length dependence of the energetic separation, we investigate the role played by the aforementioned factors.

To this end, we perform electronic-structure calculations on the isolated molecules. The increased delocalization in molecules S1 through S4 results in smaller HOMO-LUMO gaps. Importantly, we find that the energetic separation between the HOMO level of the isolated molecules and the MMMJ E_F decreases with increasing length as shown in Table 3.2 . However, this alone does not completely explain the energetic separation between the chemical potential of the electrodes and the HOMO levels of the MMMJs, which is also governed by the shifts in the energy levels upon contact formation. We determine these shifts by comparing the energies of the HOMO levels of the isolated molecules with the corresponding energies of the

HOMO levels of the MMMJ, which are identified by the energetic location of the transmission peak below the chemical potential (Fig. 3.5(b)). The shift upon contact is found to be highest for the S1 based MMMJ (0.32 eV downward) and decreases with increasing length, being the smallest for the S4 based MMMJ (0.21 eV downward). Thus, the shift of the energy levels compliments the energetic separation of isolated molecules, resulting in a large (small) shift for short (long) molecules. The electronic-structure origins for a large shift (reorganization) for shorter molecules is explained in detail in chapter V in the context of dithiol terminated molecules.

3.4.3 Isocyanide based MMMJs

We model the transport properties of the triphenyl di-isocyanide based MMMJs to analyze the sign dependence of the MMMJ thermopower on the molecular end-groups. In this model, we observe that the top-site model was the most energetically favorable contact model through which isocyanide end-group binds to the Au atoms in the extended molecule.

Although the experiments were performed on mono-isocyanide end-group $(NC)\,3$ molecules, for modeling simplicity, we model a di-isocyanide $(NC)_2\,3$ terminated MMMJ to calculate the thermopower which can then be compared against experimental values. This modeling scheme is justified by our observation of the invariance of the Seebeck coefficient on the coupling strength. The computed transmission function $\tau(E)$ is shown in Fig. 3.6(a). The $\tau(E)$ plot shows that transport in diisocyanide junctions is dominated by the LUMO channel, resulting in n-type transport. The Seebeck coefficient calculated for the $(NC)_2\,3$ molecular junction was $-1.6\frac{\mu V}{K}$. This value matches in sign with the experiments and has a magnitude comparable to the experimentally measured value of $-1.0 \pm 0.4\frac{\mu V}{K}$. The negative Seebeck co-

efficient of the isocyanide MMMJ is in contrast to the positive coefficient of the corresponding thiol-terminated MMMJs.

System	Thermopower $S\left(\frac{\mu V}{K}\right)$	
	Computed Values	Experimental Values
$SS1$	2.4	9.8 ± 0.6
$SS2$	10.8	11.7 ± 1.3
$SS3$	21.9	15.4 ± 1.0
$S1$	3.6	8.1 ± 0.8
$S2$	14.5	13.6 ± 1.2
$S3$	26.1	17.6 ± 1.0
$S4$	35.8	21.0 ± 1.3

Table 3.1: Computed thermopower S of MMMJs made up of phenyl molecules with monothiol, dithiol and isocyanide end-groups. The computed values are also compared against experimentally measured thermopower values.

System	Computational		Experimental
	$\epsilon_{IM}^{H}\ (eV)$	$\Delta\ (eV)$	$eV_{trans}\ (eV)$
$S1$	-6.42	1.22	0.87 ± 0.17
$S2$	-6.13	0.93	0.83 ± 0.15
$S3$	-5.96	0.76	0.69 ± 0.20
$S4$	-5.84	0.64	0.69 ± 0.26

Table 3.2: Computed values of HOMO energies $\left(\epsilon_{IM}^{H}\right)$ of phenyl molecules with monothiol end-groups. The computed values of the energy difference (Δ) between the HOMO transmission peak and the Fermi energy E_F of the MMMJs made up on phenyl molecules with monothiol end-groups. These computed values are compared against experimentally measured transition voltage eV_{trans} values.

3.4.4 Comparing electronic-structure of $SS3$ and $(NC)_2\,3$

To get a better understanding of this result, we calculate the density of states of the MMMJs localized on the molecular region (henceforth called as molecular density of states or M-DoS) of the triphenyl molecule with thiol $SS3$ and isocyanide $(NC)_2\,3$ end-groups. The computed M-DoS is plotted in Fig. 3.6(b).

The M-DoS plot indicates that the peaks in the M-DoS coincide with the peaks in the corresponding $\tau(E)$ plots. And as a result we see that, the M-DoS peak of the $SS3$ junction that is closest to the junction E_F lies below Fermi energy E_F. This in turn results in HOMO dominated (or p-type) electronic transport across the molecular junction. In contrast, the M-DoS of $(NC)_2\,3$ junctions shows that electronic transport in these junctions is dominated by orbitals above the E_F (n-type), resulting in a negative thermopower.

To further characterize the transport mechanism, we would like to identify the molecular orbital in the MMMJ that dominates the electronic transport and compare it against the dominant frontier molecular orbitals (HOMO/LUMO) of the isolated molecules. The molecular orbitals in MMMJ are characterized by spectrally decomposing the transmission matrix at the energies that corresponds to the dominant peaks in the transmission function $\tau(E)$[50]. This constitutes to the HOMO peaks for the $SS3$ molecular junctions and LUMO peaks for the $(NC)_2\,3$ junctions.

In both the molecular junctions considered in the present study, a single eigenchannel, referred to as the dominant conduction orbital (DCO), contributes to more than 99% of transport. The DCO's of both the $SS3$ and $(NC)_2\,3$ molecular junctions are shown in Figs. 3.7(a) and (b). Here we can observe that the DCO of the $SS3$ MMMJs exhibit π bonding, very closely resembling the HOMO molecular orbitals of the isolated molecule (Fig. 3.7(a)). On the other hand, the DCO of $(NC)_2\,3$ MMMJs exhibit the π^* bonding closely resembling the LUMO molecular orbitals of the isolated molecule (Fig. 3.7(b)). A similar analysis was made for other aromatic molecules considered in this work (see Appendix. A for more details) in which we observed that for all MMMJs with HOMO dominated transport (p-type) had a DCO with π bonding, very closely resembling the HOMO molecular orbitals of isolated

molecules. Whereas in case of MMMJs with LUMO dominated transport (n-type), the DCOs exhibited π^* bonding closely resembling the LUMO molecular orbitals of the isolated molecule.

This analysis reiterates our hypothesis that upon contact with metal electrodes the frontier molecular orbitals of the molecules reorganize to new energies without a significant modification to their spatial representation. However this analysis still does not provide a comprehensive explanation of the influence of molecular end-groups on the electronic-structure of the MMMJs and in turn on their thermopower. This elucidation will be provided in the next chapter.

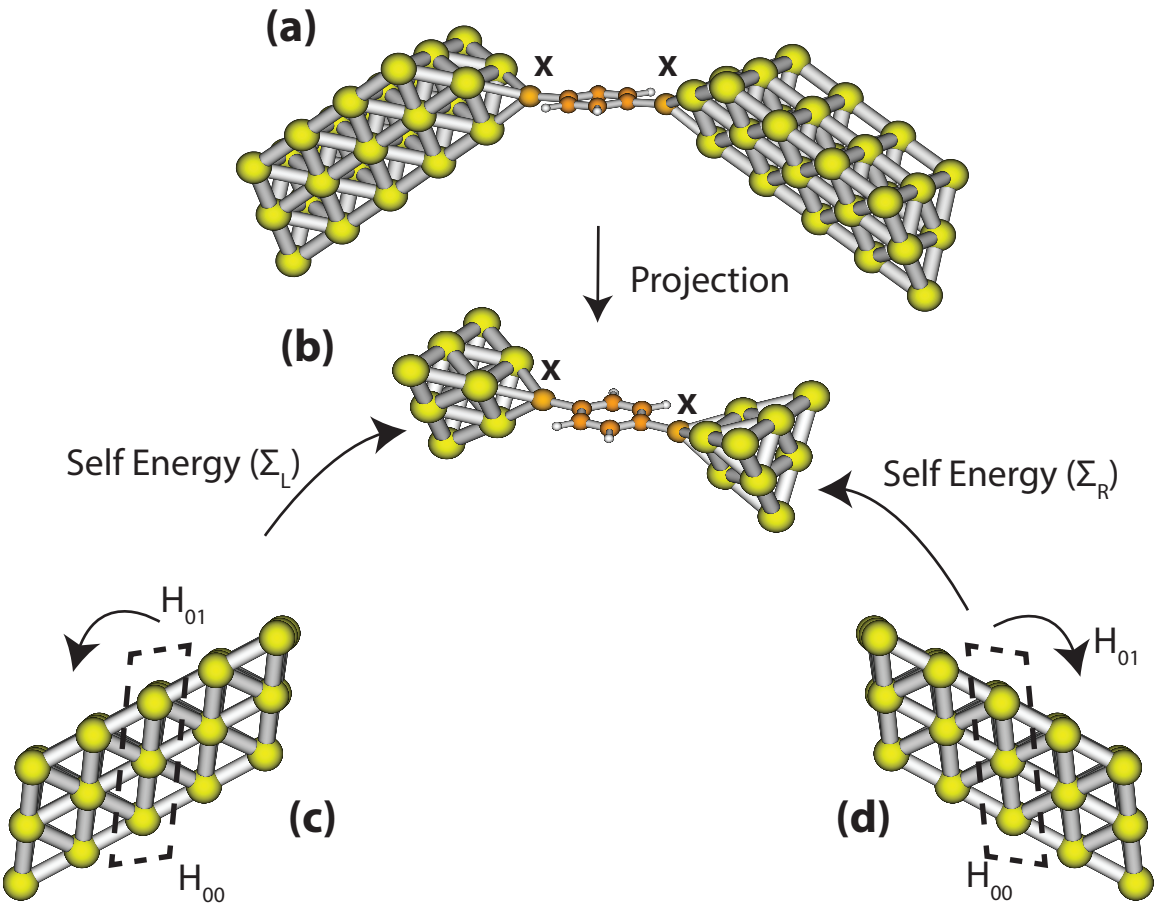

Figure 3.3: (a) Atomic representation of the central region (extended molecule) comprising of molecule connected to Au clusters through the relevant contact model. (b)Atomic representation of the region onto which the Hamiltonian of the central region is projected to remove surface effects. (c) Atomic representation of the Au cluster from which the self energy of the left electrode $\left(\hat{\Sigma}_L\right)$ is constructed. (d) Atomic representation of the Au cluster from which the self energy of the right electrode $\left(\hat{\Sigma}_R\right)$ is constructed.

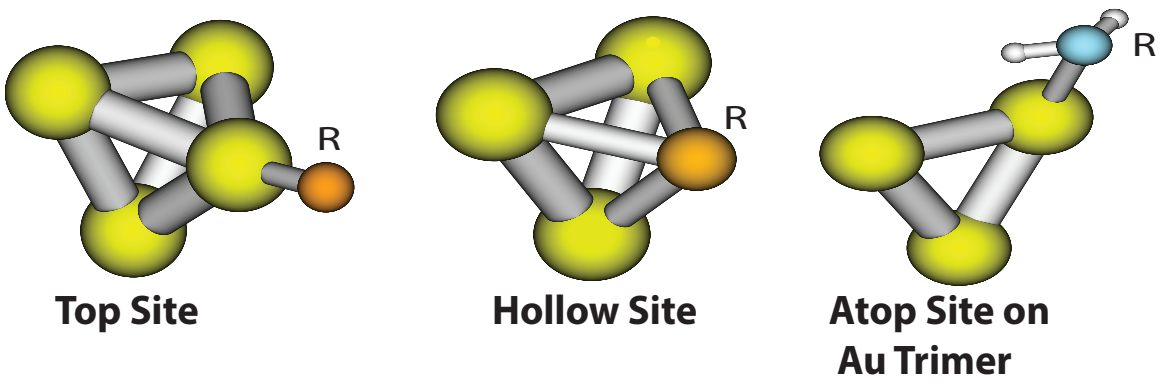

Figure 3.4: The perspective view of three important contact models that was used in this work to model the chemically bonding between the molecular end-group R to the Au atoms.

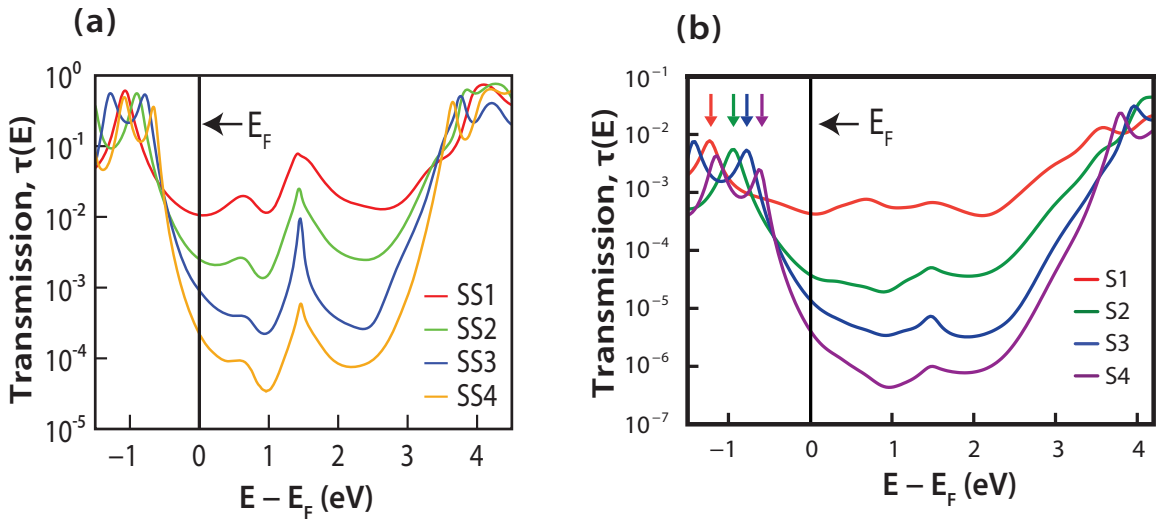

Figure 3.5: (a)Transmission function $\tau(E)$ of the MMMJs constructed from dithiol terminated phenyl molecules and Au atoms. (b)Transmission function $\tau(E)$ of the MMMJs constructed from monothiol terminated phenyl molecules and Au atoms. The arrows indicate the energies corresponding to the HOMO transmission peaks for each MMMJ.

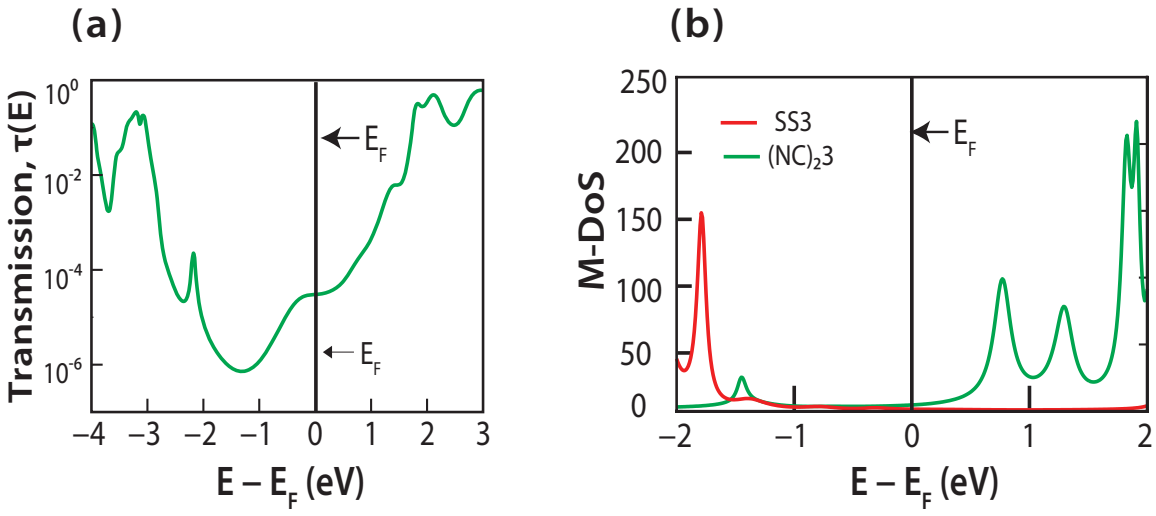

Figure 3.6: (a)Transmission function $\tau(E)$ of the MMMJs constructed from triphenyl diisocyanide and Au atoms. (b)Comparison of M-DoS of $SS3$ and $(NC)_2\,3$ based MMMJs.

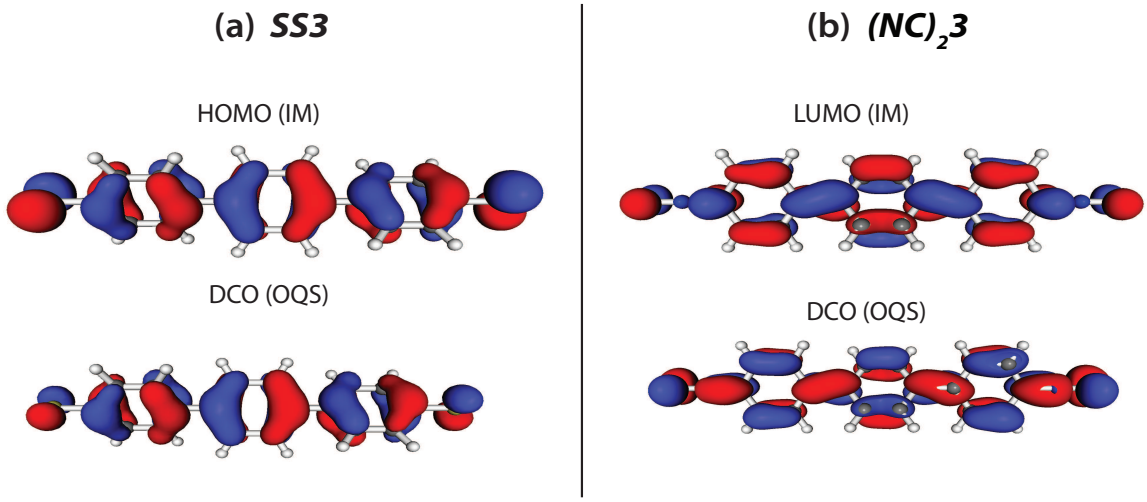

Figure 3.7: ((a) Plots comparing the HOMO orbital of triphenyl dithiol $SS3$ molecule in an isolated environment and the DCO of the same molecule in the presence of metal electrodes (MMMJs) at the HOMO transmission peak energies. (b) Plots comparing the LUMO orbital of triphenyl diisocyanide $(NC)_2\,3$ molecule in an isolated environment and the DCO of the same molecule in the presence of metal electrodes (MMMJs) at the LUMO transmission peak energies.

CHAPTER IV

Characterizing and Quantifying the End-group Influence

The experimental and computational results explained in the previous chapters provide some important insights on the length and end-group dependence of the thermoelectric properties of MMMJs However, the underlying mechanism that relates the effect of end-groups on the electronic-structure of MMMJs and in turn on the resulting thermoelectric properties needs further elucidation. This chapter bridges this gap by illustrating the role of end-groups on the resultant electronic-structure. Further this work also provides a simple intuitive understanding of the relationship between pertinent characteristics of isolated molecules (HOMO, LUMO energies, Electronegativity) and the thermopower of MMMJs created from them.

In this chapter, we begin by analyzing the electronic-structure of triphenyl dithiol ($SS3$) and triphenyl di-isocyanide ($(NC)_2\,3$) isolated molecules (Figure 2.2(a)) using density functional theory (DFT) calculations performed with GAUSSIAN-09 software[24] by employing B3LYP functional[7,6] and LANL2DZ basis sets[28]. The computed HOMO and LUMO energy levels of these molecules are presented in Table 4.1. These results indicate that the Fermi Energy (E_F) of Au (also the

E_F of MMMJ), which is $\sim$ -5.2 eV,[81] lies in the HOMO-LUMO gap of these molecules and is closer to the HOMO energy level. Interestingly, the experimental and computational studies from previous chapters suggest that Au-$(NC)_2$3-Au junctions exhibit a LUMO dominated transport, whereas Au-$SS3$-Au junctions exhibit HOMO dominated transport. This observation raises an important question: How do end-groups influence the reorganization of molecular orbital upon contact with electrodes?

Property	$SS3$	$(NC)_2$3
ϵ^H_{IM}(eV)	-5.85	-6.56
ϵ^L_{IM}(eV)	-1.42	-2.25
ΔN	-0.28	0.34
χ(eV)	4.39	5.35

Table 4.1: Energies of the HOMO (ϵ^H_{IM}) and the LUMO(ϵ^L_{IM}) of IM, charge transfer (ΔN) and electronegativity (χ) for $SS3$ and $(NC)_2$3 molecules.

4.1 Quantifying Energy Level Reorganization

In order to obtain insights into end-group mediated reorganization of energy levels, we compared the molecular density of states (M-DoS) of $SS3$ and $(NC)_2$3 before and after making contact with Au electrodes. Specifically, the M-DoS is calculated for three different scenarios: (a) isolated molecule (IM); (b) extended molecule (EM), where the molecule is coupled to Au clusters through the most stable adsorption site and; (c) open quantum system, where the extended molecule is connected to semi-infinite electrodes through the self energy operators $\hat{\Sigma_{L/R}}(z)$.

From chapter III we know that the retarded Green's function, $G^r_{ij}(z)$ of the

Schrodinger Eq. that is subsequently used to compute M-DoS, is given by

$$G^r_{ij}(z) = (zS_{ij} - H_{ij} - \Sigma_{L_{ij}} - \Sigma_{R_{ij}})^{-1} \quad z = E + i\eta \quad , \tag{4.1}$$

where E is the energy and η is a small imaginary parameter to regularize the Green's function. In the above expression, H_{ij} and S_{ij} denote the Hamiltonian and overlap matrix of the system under consideration. $\Sigma_{L/R}$ denote the self-energy operators corresponding to the left and right leads. In the case of IM and EM systems, where the systems are not in contact with the semi-infinite electrodes, the $\Sigma_{L/R}$ are set to zero.

The density of states, $D(E)$, is then obtained from $G^r(z)$ by (see section 3.2.4 for derivation)

$$D(E) \quad = -\frac{1}{\pi} Tr\left(Im\left[G^r(z)S\right]\right) \quad . \tag{4.2}$$

To compute M-DoS, the trace in Eq.4.2 is performed only over the orbitals that are centered on the molecule.

We begin with our electronic-structure analysis of the SS3 and $(NC)_2\,3$ molecular systems. The computed M-DoS for IM, EM and open quantum systems for $SS3$ and $(NC)_2\,3$ are shown in Figs. 4.1(a) and (b) respectively. The peaks in the M-DoS curves correspond to the energetic position of the frontier molecular orbitals. A comparison between the M-DoS of IM and EM for both molecules shows that the HOMO and LUMO states of the EM shift to lower energies in comparison to the IM. However, it is interesting to note that this downward shift in energies is significantly larger in the case of $(NC)_2\,3$. In particular, the shift of HOMO and LUMO states in the case of $SS3$ is -0.27 eV and -0.17 eV respectively, whereas in

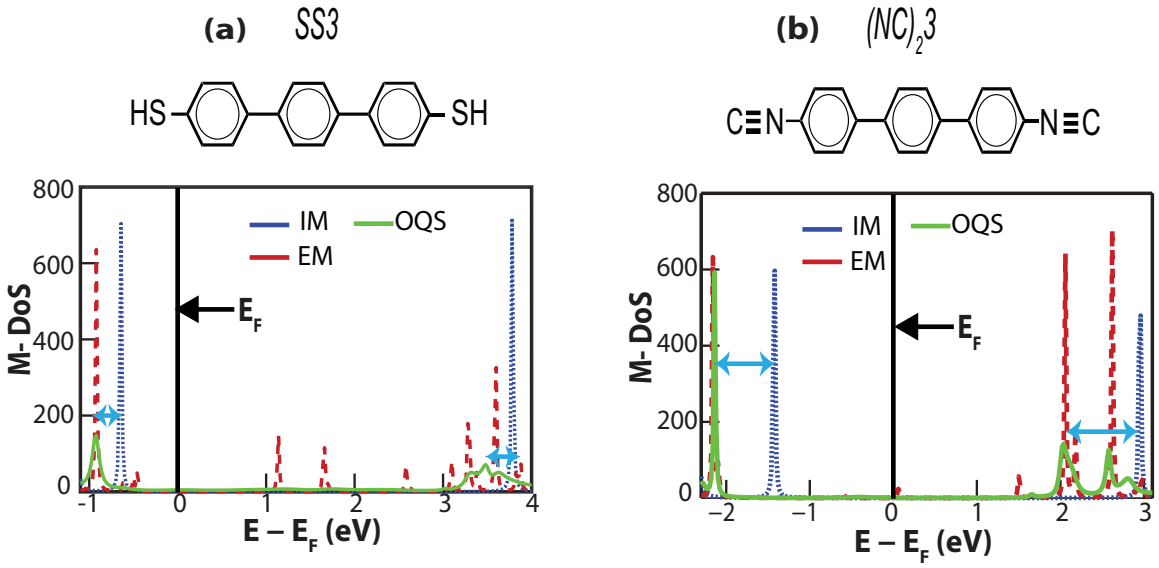

Figure 4.1: (a) M-DoS of $SS3$ molecule in different scenarios (namely isolated molecule IM, extended molecule EM and open quantum system). (b) M-DoS of $(NC)_2\,3$ molecule in different scenarios. The M-DOS of the IM, EM and open quantum system are denoted by blue-dotted line, red-dashed line and green-continuous curves respectively. The purple arrows indicate the magnitude of the M-DOS shift.

the case of $(NC)_2\,3$ these shifts are significantly larger: -0.75 eV for HOMO and -0.91 eV for LUMO. A comparison of the M-DoS of the EM and open quantum systems in Figure 4.1(a) and 4.1(b) shows that the energies corresponding to the M-DoS peaks are almost identical. In fact a similar comparison for MMMJs based on a wide range of other molecules (see Appendix. B) with Au electrodes indicate that the reorganization of the frontier molecular orbitals is completely captured by the EM system. This suggests that for the purpose of understanding the reorganization of the molecular states, the shifts in the M-DoS peaks of the EM are representative of the respective shifts in the open quantum systems. Hence, most of the subsequent analysis in this chapter compares the electronic-structure (M-DoS) of the isolated molecule (IM) only with those of the extended molecule (EM).

4.2 Molecular End-groups and Charge Transfer ΔN

Although these results demonstrate that end-groups play an important role in realigning the molecular orbitals, the dominant mechanism that leads to the differences in the magnitude of these shifts is yet to be identified. As a first step towards answering this question, we compare the number of electrons present in the isolated and extended molecular systems. The insights obtained from such an analysis are also expected to be valid for the open quantum system, since the shift of the M-DOS is completely captured by the extended molecule. To quantify the change in the number of electrons in the IM and EM systems, we define the electrode-coupling induced *charge transfer* (ΔN) as

$$\Delta N = N_{IM} - N_{EM} \quad , \tag{4.3}$$

where N_{IM} denotes the number of electrons in the IM, and N_{EM} denotes the number of electrons in the spatial location of the molecule in the EM system. N_{EM} is computed by expressing the single particle density matrix $\hat{\rho}$ in the localized natural atomic orbital (NAO) basis and performing the trace only over the orbitals which are centered on the molecule:

$$N_{EM} = \sum_{i \in Mol} \hat{\rho}_{ii} \quad . \tag{4.4}$$

This approach is commonly referred to as natural population analysis[58]. In the case of $(NC)_2\,3$, N_{IM} is simply obtained from the total number of electrons in the IM. However in the case of $SS3$, as the hydrogen atoms are assumed to have deprotonated upon contact with Au atoms (in EM system), the electrons contributed by them

are excluded from N_{IM}. The ΔN values for $SS3$ and $(NC)_2\,3$ (see Table 4.1) indicate that, $SS3$ molecule gains 0.28 electron partial charge upon contact with the Au atoms. Such a gain in electronic charge is in agreement with recent studies[81,67,53]. On the other hand, $(NC)_2\,3$ molecule loses 0.34 electron partial charge to Au atoms. It is interesting to note that the magnitude in the shift of M-DoS between IM and EM systems is greater for $(NC)_2\,3$ which loses electrons, while the shift is smaller for $SS3$ which gains electrons.

4.3 Charge Transfer Hypothesis

Based on the above observations, we hypothesize that the magnitude of the shift in M-DoS is correlated to the end-group mediated charge transfer between Au atoms and the molecule. In particular, the shift in M-DoS is governed by two important factors: (i) the stabilization of energy levels induced by the physical contact to the Au cluster; (ii) the change in electron-electron interactions (Coulomb repulsion and exchange-correlation effects) due to the chemical interaction between the molecule and the Au atoms to neutralize the chemical potential. This chemical interaction is characterized by the charge transfer between the molecule and the Au atoms. The effect of stabilization is to shift the energy levels to lower energies, whereas the effect of electron-electron interactions (*aka* charge transfer effect) is to increase their energies.

For example, in the case of $SS3$, the partial electron gain increases the electron-electron repulsion which increases the energy of molecular orbitals. This results in the stabilization and charge-transfer effect opposing one another in turn resulting in a small magnitude of total shift (reorganization). However in the case of $(NC)_2\,3$, the charge transfer is out of the molecule which reduces the electron-electron repul-

sion. This results in the stabilization and charge-transfer effect complementing one another resulting in a large magnitude total shift (reorganization) to lower energies. A schematic presentation of the proposed mechanism is shown in Fig. 4.2.

We note that the effect of charge transfer between a molecule and electrodes, upon contact, can also be described in terms of interface dipoles[34,73,9,39]. In fact, past work has invoked this picture to quantitatively understand the barriers to electron/hole injection at the interface of organic molecular layers and metal electrodes, in the context of organic light emitting diodes and photovoltaic devices[14,23]. In the present work, the computed M-DoS accounts for both the effect of charge transfer and the stabilization of energy levels resulting from the bond formation at the electrodes. Further, we subsequently also relate the resulting electronic-structure to the thermoelectric properties of MMMJs.

While the charge transfer hypothesis correlates the direction of charge transfer to the extent of the reorganization of the FMOs, the direction of charge transfer is determined by the difference in the electronegativity (χ) of the molecule and that of the Au cluster. In the present work, we use the Mulliken's definition[45] of electronegativity (χ), where χ is defined as average of ionization energy and electron affinity. The ionization energies and electron affinities of all systems of interest (molecules, Au clusters) are computed at the DFT level using B3LYP functional and LANL2DZ basis set. The χ of Au cluster with the hollow site configuration—contact model for $SS3$—is computed to be 4.98 eV, while that of the top site configuration—contact model for $(NC)_2 3$—is computed to be 4.90 eV (see Fig. 3.4 for contact geometries). The χ of $SS3$ is computed to be 5.23 eV, which is higher than that of the Au cluster, explaining the computed charge transfer into the molecule. In contrast, the χ of $(NC)_2 3$ is computed to be 4.39 eV, which is lower than the electronegativity of the

Au cluster, explaining the charge transfer out of the molecule.

4.4 Validating the Charge Transfer Hypothesis

The hypothesis assumes that the coupled effect of stabilization and charge-transfer effects determine the total-shift in the energies of the molecular orbitals. The hypothesis can be validated if we can independently quantify the influence of these effects on the energy level shift. These effects cannot be delineated experimentally and so their influence can only be quantified independently through a computational model. In order to quantify the role of both stabilization and charge transfer effects on the reorganization of frontier molecular orbital (FMOs) in molecular junctions, we adopt the following computational approach. First, we compute the electronic-structure of isolated molecules (IM) in vacuum. Subsequently, to understand the effect of stabilization, we compute the shifts in the energies of FMOs due to the perturbing potential of the electrode atoms without allowing for charge transfer. We refer to this intermediate hypothetical state as the stabilized molecule (SM). Finally, we perform a self-consistent calculation that allows for charge transfer between the electrodes and the molecule. This calculation includes the effect of both stabilization and charge transfer. Comparing the energies of FMOs from the self-consistent calculation with that of the SM calculation allows us to delineate the charge transfer effects on the reorganization of FMOs.

In order to compute the effect of stabilization due to the perturbing potential of Au electrodes on the FMOs, we consider Au clusters that comprise of four $\{111\}$ planes of six Au atoms each in addition to the contacting Au atoms (hollow-site for $SS3$ and top-site $(NC)_2 3$). The geometry of the SM system is same as that of the extended molecule (EM) that was previously discussed. The Hamiltonian H_{SM}

corresponding to the SM is defined as

$$H_{SM} = H_{IM} + V_{Au} \ , \tag{4.5}$$

where H_{IM} denotes the Hamiltonian of the IM and V_{Au} denotes the perturbing potential of the Au clusters. We note that V_{Au} is the effective Kohn-Sham (KS) potential that is obtained from a DFT calculation of isolated Au clusters. In order to compute H_{SM}, we express H_{IM} and V_{Au} in the same basis. This is achieved by including the basis functions of Au clusters as ghost atoms in the computation of the electronic-structure of IM. Similarly, the basis functions of IM are included as ghost atoms in the computation of the electronic-structure of isolated Au clusters. The stabilization effect on the reorganization of FMOs is extracted by comparing the molecular density of states (M-DoS) peaks of the IM and the SM. The M-DoS is defined as

$$\text{M-DoS}(E) = -\frac{1}{\pi} Tr\left[Im\left(G^r(z)S\right)\right]_{Mol} \quad z = \lim_{\eta \to 0} E + i\eta \ , \tag{4.6}$$

where S denotes the overlap matrix of the common basis set, $G^r(z)$ denotes the retarded Green's function of the system under consideration, E denotes the energy and η is a small parameter to regularize the Green's function. To compute the M-DoS of the IM, the Green's function $G^r(z)$ of the IM, denoted by $G^r_{IM}(z)$, is used in Eq. (4.6), which in turn is given by

$$G^r_{IM}(z) = \left(zS - H_{IM}\right)^{-1} \ . \tag{4.7}$$

The retarded Green's function of SM, denoted by G^r_{SM}, can be computed by em-

ploying the Lippman Schwinger equation[18] as

$$\begin{aligned} G^r_{SM}(z) &= G^r_{IM}(z) + G^r_{IM}(z) V_{Au} G^r_{SM}(z) \ , \\ &= \sum_{n=0}^{\infty} G^r_{IM}(z) \left[V_{Au} G^r_{IM}(z) \right]^n \ , \\ &= (zS - H_{SM})^{-1} \ . \end{aligned} \tag{4.8}$$

Subsequently, the M-DoS of the SM, is computed by replacing G^r with G^r_{SM} in Eq. (4.6).

The M-DoS of the SM captures only the effects of the electrodes to stabilize the energy levels, and not the effects of change in e-e interactions due to charge transfer. In order to account for both these effects, we compute the electronic-structure and M-DoS of the molecular system comprising of the molecule in chemical contact with the Au clusters. This system is the same as the extended molecule (EM) previously described. The EM represents the final state after charge equilibration. The M-DoS for the EM can be computed by replacing G^r with G^r_{EM} in Eq. (4.6), where $G^r_{EM}(z)$ denotes the retarded Green's function of the EM, and is given by

$$G^r_{EM}(z) = (zS - H_{EM})^{-1} \ , \tag{4.9}$$

where H_{EM} denotes the Hamiltonian of the EM.

The computed M-DoS of the IM, SM and EM, for $SS3$ and $(NC)_2 3$, are shown in Figs. 4.3(a) and (b), respectively. The M-DoS for all the systems considered in the present work are plotted with respect to the Fermi energy of Au ($E_F = -5.2$ eV[81])—a common baseline—as the location of FMOs with respect to the Fermi energy of the contacting electrodes governs the thermoelectric properties of the junction. In order to quantify the shift of FMOs due to stabilization and charge transfer

effects separately, we begin by identifying the energies of FMOs in the IM from their M-DoS peaks. We denote by ϵ^H_{IM} and ϵ^L_{IM} the energies of highest occupied molecular orbital (HOMO) and the lowest unoccupied molecular orbital (LUMO) of the IM, respectively. These energy values for $SS3$ are $\epsilon^H_{IM} = -5.85$ eV and $\epsilon^L_{IM} = -1.42$ eV. For $(NC)_2 3$, these energy values are $\epsilon^H_{IM} = -6.56$ eV and $\epsilon^L_{IM} = -2.25$ eV. We note that the Fermi Energy of Au ($E_F = -5.2\ eV$) lies in the HOMO-LUMO gap of these molecules, and is closer to the HOMO energy level in both cases.

M-DoS Shift	$SS3$	$(NC)_2 3$
$\Delta\epsilon^H_{SM-IM}$(eV)	-0.77	-0.21
$\Delta\epsilon^L_{SM-IM}$(eV)	-1.01	-0.73
$\Delta\epsilon^H_{EM-SM}$(eV)	0.50	-0.54
$\Delta\epsilon^L_{EM-SM}$(eV)	0.84	-0.18

Table 4.2: The reorganization of FMOs (HOMO/LUMO) due to the individual effects of stabilization $\left(\Delta\epsilon^H_{SM-IM}/\ \Delta\epsilon^L_{SM-IM}\right)$ and charge transfer $\left(\Delta\epsilon^H_{EM-SM}/\ \Delta\epsilon^L_{EM-SM}\right)$ for $SS3$ and $(NC)_2 3$ molecules.

M-DoS Shift	$SS3$	$(NC)_2 3$
$\Delta\epsilon^H_{EM-IM}$(eV)	-0.27	-0.75
$\Delta\epsilon^L_{EM-IM}$(eV)	-0.17	-0.91

Table 4.3: The overall shift of the FMOs (due to both stabilization and charge transfer) using the full self-consistent calculation (EM) $\left(\Delta\epsilon^H_{EM-IM}/\ \Delta\epsilon^L_{EM-IM}\right)$ for $SS3$ and $(NC)_2 3$ molecules.

The shift of FMOs due to the individual effects of stabilization and charge transfer are determined from the energies of the M-DoS peaks of IM, SM and EM. To this end, we denote the energies of FMOs of the SM as ϵ^H_{SM} and ϵ^L_{SM}, and those of EM as ϵ^H_{EM} and ϵ^L_{EM}. The shifts in the energies of FMOs due to stabilization are given by $\Delta\epsilon^H_{SM-IM} = \epsilon^H_{SM} - \epsilon^H_{IM}$ and $\Delta\epsilon^L_{SM-IM} = \epsilon^L_{SM} - \epsilon^L_{IM}$. Similarly the shifts associated with charge transfer are given by $\Delta\epsilon^H_{EM-SM} = \epsilon^H_{EM} - \epsilon^H_{SM}$ and $\Delta\epsilon^L_{EM-SM} = \epsilon^L_{EM} - \epsilon^L_{SM}$. The shift of FMOs for $SS3$ due to stabilization are –0.77

eV and –1.01 eV respectively for HOMO ($\Delta\epsilon^{H}_{SM-IM}$) and LUMO ($\Delta\epsilon^{H}_{SM-IM}$). The corresponding shifts for $(NC)_2 3$ are $\Delta\epsilon^{H}_{SM-IM} = -0.21$ eV and $\Delta\epsilon^{L}_{SM-IM} = -0.73$ eV. We note that, in both the cases of $SS3$ and $(NC)_2 3$, the FMOs shift towards lower energies, confirming the proposed influence of the stabilization effect of the Au electrode potential (V_{Au}) on the FMOs reorganization. The shifts in the energies of FMOs resulting from charge transfer between the SS3 molecule and contacting Au clusters are computed to be $\Delta\epsilon^{H}_{EM-SM} = 0.5$ eV and $\Delta\epsilon^{L}_{EM-SM} = 0.84$ eV. In contrast, in the case of $(NC)_2 3$, these values are computed to be $\Delta\epsilon^{H}_{EM-SM} = -0.54$ eV and $\Delta\epsilon^{L}_{EM-SM} = -0.18$ eV.

It is interesting to note that, while the charge transfer effect shifts the FMOs to higher energies in $SS3$, it shifts these energy levels to lower energies in the case of $(NC)_2 3$. These contrasting shifts of the FMOs results in the HOMO level remaining closer to E_F in the case of $SS3$ EM and the LUMO level moving closer to E_F in the case of $(NC)_2 3$ EM (cf. Figs. 4.3(a)-(b)). The location of the FMOs of the EM with respect to E_F is in turn strongly correlated to the nature of transport[69,5], which results in p-type transport in $SS3$ as opposed to n-type transport in $(NC)_2 3$.

The results discussed above explicitly validate the charge transfer hypothesis, which correlates the direction of charge transfer to the extent of reorganization of the FMOs, by delineating the individual effects of stabilization and charge transfer on the reorganization of FMOs. In particular, for both $SS3$ and $(NC)_2 3$, the effect of the perturbing potential of the Au electrodes resulted in a shift of the FMOs to lower energies. In the case of $SS3$ with charge transfer into the molecule, the effect of charge transfer resulted in a shift of the FMOs to higher energies, resulting in a small overall shift of the FMOs to lower energies, computed to be $\Delta\epsilon^{H}_{EM-IM} = -0.27$ eV and $\Delta\epsilon^{L}_{EM-IM} = -0.17$ eV for HOMO and LUMO respectively. Whereas, in the

case of $(NC)_2 3$ with charge transfer out of the molecule, the effect of charge transfer resulted in a shift of the FMOs to lower energies, resulting in a larger overall shift of the FMOs to lower energies $\left(\Delta\epsilon^{H}_{EM-IM} = -0.75 \text{ eV}, \Delta\epsilon^{L}_{EM-IM} = -0.91 \text{ eV}\right)$. Thus the charge transfer hypothesis elucidates how the end-groups determine the molecular electronegativity (χ) which in turn determines the direction of charge transfer ΔN (into the molecule or out of the molecule). The direction of charge transfer determines the magnitude of the total shift of the energy levels. The molecules that gain charge have a small total shift due to the opposing influences of the stabilization and charge transfer effect. However the energy levels of the molecules that lose charge experience a large total shift to lower energies due to the complementary nature of the stabilization and charge transfer effect.

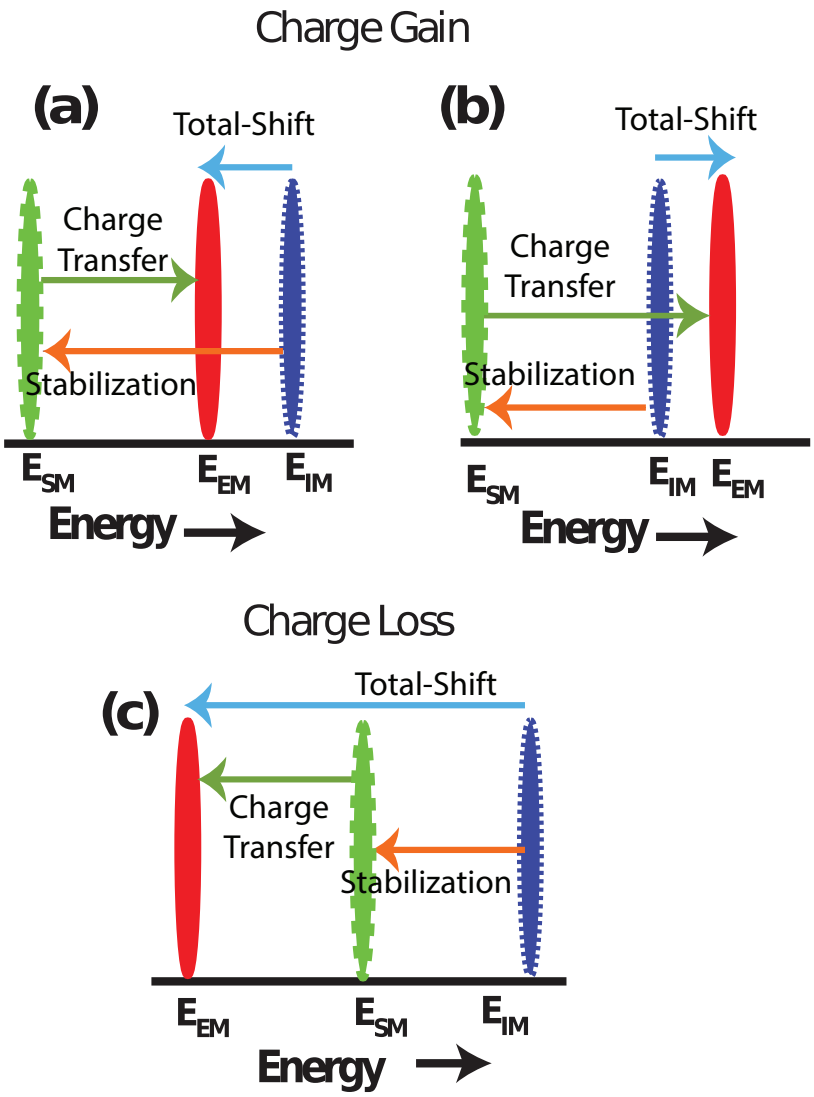

Figure 4.2: Schematic of the FMOs reorganization based on the charge transfer hypothesis: The stabilization effect, always lowers the FMO energy $(E_{IM} \rightarrow E_{SM})$. (a-b) In a charge gaining molecule the charge transfer effect increases the FMO energy. The opposing nature of stabilization and charge transfer effects result in a small total-shift of the FMO energies. (c)In a charge losing molecule the charge transfer effect decreases the FMO energy. The complementary nature of stabilization and charge transfer effects result in a large total-shift of the FMOs to lower energies.

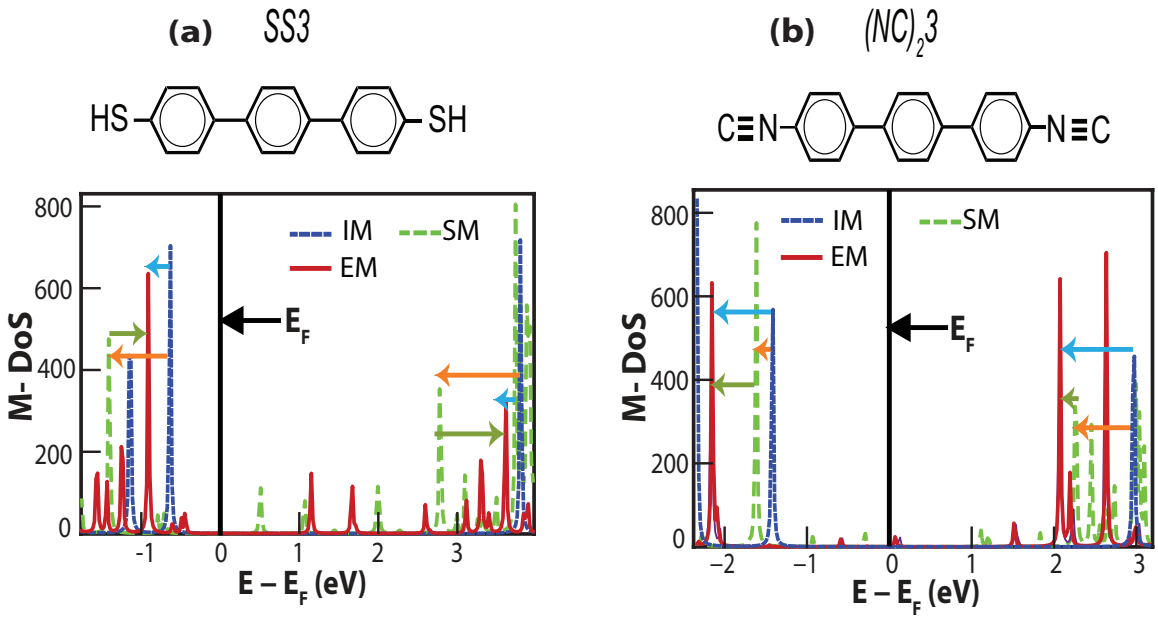

Figure 4.3: (a) M-DoS of $SS3$ molecule in different scenarios (IM, SM and EM). (b) M-DoS of $(NC)_2\,3$ molecule in different scenarios. The orange arrow indicates the shift due to stabilization effect. The green arrow indicates the shift due to charge transfer effect and the blue arrow indicates the total-shift of the M-DoS peaks.

CHAPTER V

Generality of the Charge Transfer Hypothesis

The charge transfer hypothesis introduced in chapter IV was able to successfully elucidate how the molecular end-groups influence the MMMJ electronic-structure and in turn their thermo-electric properties. However most of the previous analysis was based on just triphenyl molecule with thiol ($SS3$) and isocyanide end-groups ($(CN)_2\,3$). We would like to extend our analysis to various other molecules and end-groups to validate the generality of the charge transfer (CT) hypothesis. In this chapter we employ CT hypothesis to analyze the energy level reorganization and its influence on transport properties for MMMJs based on six other aromatic molecules with different end-groups and molecular lengths

5.1 Triphenyl Dihydroxyl ($OO3$) and Triphenyl Dinitrile ($(CN)_2\,3$)

We extend our study to MMMJs based on various other aromatic molecules. As a first step, we consider triphenyl dihydroxyl ($OO3$) and triphenyl di-nitrile ($(CN)_2\,3$) (Figure 2.2). Similar to the thiol end-group, the hydroxyl end-group is assumed to have deprotonated upon contact with Au[83]. The stable adsorption site for $OO3$ and $(CN)_2\,3$ are respectively the hollow and top[43] sites. The HOMO-LUMO

energy values for the corresponding isolated molecules are presented in Table 5.1. Similar to the previous systems, the E_F lies in the HOMO-LUMO gap with the HOMO level being closer to the E_F. The electronegativity χ values calculated for these molecules are shown in Table 5.1. The χ value of $OO3$ (5.35 eV) is higher when compared to the hollow-site Au cluster (4.98 eV) to which it binds indicating a charge gain by the molecule. On the other hand, the χ value of $(CN)_2\,3$ (4.39 eV) is lower compared to the top-site Au cluster (4.90eV) to which it binds indicating a charge loss by the molecule. The computed values of charge transfer (ΔN) are indeed consistent with the χ values as shown in Table 5.1. Based on the CT hypothesis we would predict that for the charge gaining $OO3$ molecule, the stabilization and charge transfer effects are opposing one another resulting in a small total shift. The small total shift must retain the HOMO level of the molecule closer to the MMMJ E_F in turn resulting in a HOMO dominated (p-type) transport. On the other hand, for the charge losing $(CN)_2\,3$ molecule, the stabilization and charge transfer effects are complementing one another resulting in a large total shift of the orbitals to lower energies. This large total shift should bring the LUMO level of the molecule closer to the MMMJ E_F in turn resulting in a LUMO dominated (n-type) transport.

These predictions are validated by computing the M-DoS of the molecules in an isolated environment (IM) and in contact with the cluster of Au atoms through the most stable contact model (extended molecule, EM). The computed M-DoS values of $OO3$ and $(CN)_2\,3$ are shown in Figs. 5.1(a) and (b). We could observe from these figures that in case of $OO3$ the energy levels undergo a small total shift which retains the HOMO level closer to E_F. Whereas in $(CN)_2\,3$ system, the energy levels undergo a large total shift to lower energies bringing the LUMO level closer to E_F as predicted by the CT hypothesis. The numerical values of the total shift $\left(\Delta\epsilon^{H/L}_{EM-IM}\right)$

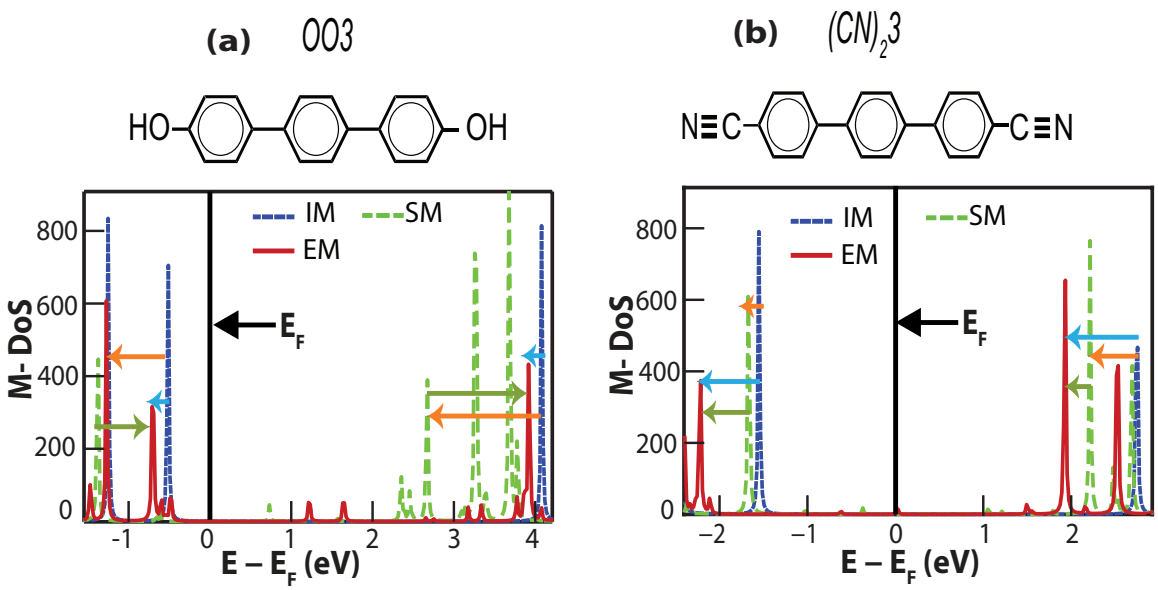

Figure 5.1: (a) M-DoS of $OO3$ molecule in different scenarios (IM, SM and EM systems). (b) M-DoS of $(CN)_2\,3$ molecule in different scenarios. The orange arrow indicates the shift due to stabilization effect. The green arrow indicates the shift due to charge transfer effect and the blue arrow indicates the total-shift of the M-DoS peaks.

of both $OO3$ and $(CN)_2\,3$ based systems are provided in Table. 5.3.

The CT hypothesis can be further validated by independently quantifying the shift due to the stabilization effect and the charge transfer effect. This is achieved by computing the shift of the energy levels (M-DoS) due to the perturbing potential of the electrode atoms without allowing for charge transfer. We refer to this intermediate hypothetical state as the stabilized molecule (SM). Comparing the M-DoS of the SM with those of the IM systems provide the shift due to stabilization effect ($\Delta\epsilon^{H/L}_{SM-IM}$ —see Table 5.2). These values show that the energy levels move to lower energies in both $OO3$ and $(CN)_2\,3$ molecules due to the stabilization effect as predicted by the CT hypothesis. Comparing the M-DoS of the SM with those of the EM systems provide the shift due to charge transfer effect ($\Delta\epsilon^{H/L}_{EM-SM}$—see

Table 5.2). These values show that for the charge gaining $OO3$ molecule the charge transfer effect shifts the energy levels to higher energies, whereas for the charge losing $(CN)_2\,3$ molecule, the charge transfer effect shifts the energy levels to lower energies consistent with the CT hypothesis.

5.2 Triphenyl diamine ($(NH_2)_23$) and 4-4' Bipyridine ($NN2$)

Next we consider MMMJs based on triphenyl diamine ($(NH_2)_23$) and 4-4' bipyridine ($NN2$) (Figure 2.2). The stable adsorption site for $(NH_2)_23$ and $NN2$ are respectively the a-top trimer and top[43] sites. The HOMO-LUMO energy values for the corresponding isolated molecules are presented in Table 5.1. Similar to the previous systems, the E_F lies in the HOMO-LUMO gap of $NN2$ with the HOMO level being closer to the E_F. Interestingly, in case of $(NH_2)_23$, unlike the other end-groups, the HOMO level of the isolated molecule is above the E_F of Au electrode. The electronegativity χ values calculated for these molecules are shown in Table 5.1. The χ value of $(NH_2)_23$ (2.70 eV) is lower when compared to the atop-site Au cluster (4.98 eV) to which it binds indicating a charge loss by the molecule. Similarly the χ value of $NN2$ (4.56 eV) is also lower compared to the top-site Au cluster (4.90 eV) to which it binds indicating a charge loss by the molecule. The computed values of charge transfer (ΔN) are indeed consistent with the χ values as shown in Table 5.1. Based on the CT hypothesis we would predict that since both the molecules have a net charge loss, the stabilization and charge transfer effects are complementing one another resulting in a large total shift to lower energies. In case of $NN2$, we predict that this large total shift should bring the LUMO level of the molecule closer to the MMMJ E_F in turn resulting in a LUMO dominated (n-type) transport. On the other hand in case of $(NH_2)_23$, we predict that this large total shift

would move the molecular HOMO level below the MMMJ E_F resulting in HOMO dominated transport.

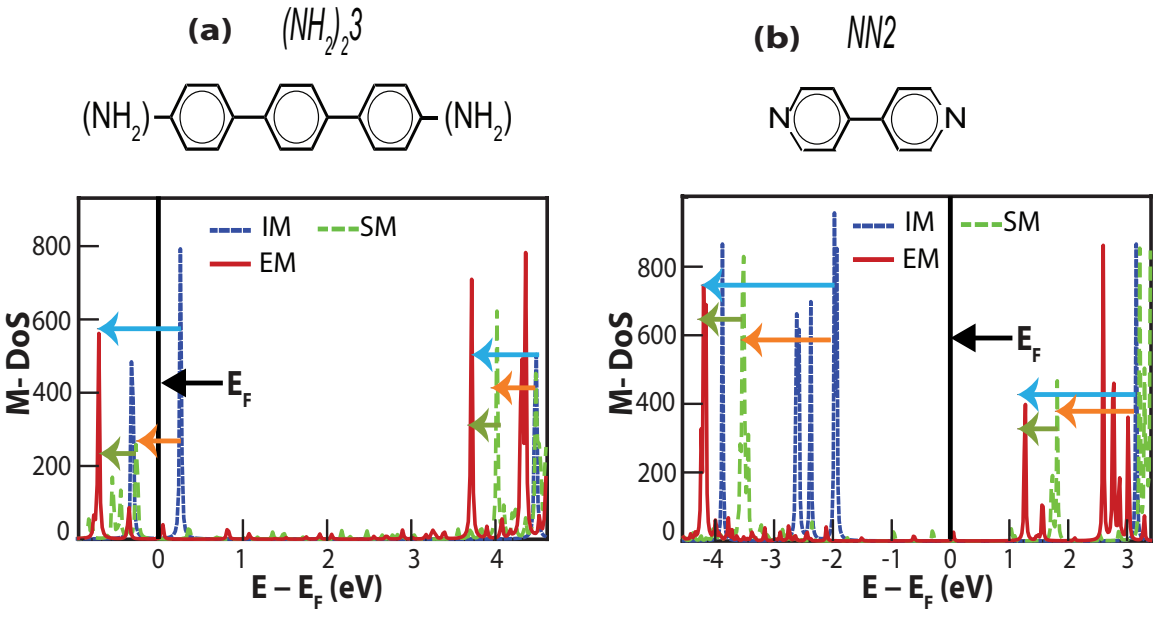

Figure 5.2: (a) M-DoS of $(NH_2)_23$ molecule in different scenarios (IM, SM and EM systems). (b) M-DoS of $NN2$ molecule in different scenarios. The orange arrow indicates the shift due to stabilization effect. The green arrow indicates the shift due to charge transfer effect and the blue arrow indicates the total-shift of the M-DoS peaks.

Similar to previous analysis, these predictions are validated by computing the M-DoS of the molecules in an isolated environment (isolated molecule IM), molecules experiencing the external potential of Au atoms due to physical contact (stabilized molecule, SM) and molecules in chemical contact with the cluster of Au atoms through the most stable contact model (extended molecule, EM). The computed M-DoS values of $(NH_2)_23$ and $NN2$ are shown in Figs. 5.2 (a) and (b). As predicted, the stabilization effect (obtained by comparing M-DoS peaks of IM and SM) and the charge transfer effect (obtained by comparing M-DoS peaks of SM and EM) complement one another to create a large total shift to lower energies. As predicted, this

large total shift brings the LUMO level of the $NN2$ molecule close to the MMMJ E_F which would result in a HOMO LUMO dominated (p-type) transport. In case of $(NH_2)_2 3$, the large total-shift pushes the HOMO level of the molecule below the E_F that would result in a LUMO dominated (n-type) transport. The numerical values of the total shift $\left(\Delta\epsilon^{H/L}_{EM-IM}\right)$ is provided in Table 5.3. The numerical values of the independent shift due to stabilization $\left(\Delta\epsilon^{H/L}_{SM-IM}\right)$ and charge transfer effects $\left(\Delta\epsilon^{H/L}_{EM-SM}\right)$ are provided in Table 5.3.

Finally, we can calculate the transport properties for MMMJs based on these molecules. The transmission function $\tau(E)$ calculated for all these molecules are plotted in Fig. 5.3. From these plots, we can observe that in case of $OO3$ and $(NH_2)_2 3$, the HOMO transmission peak is closer to the MMMJ E_F which results in a negative slope of the $\tau(E)$ at the E_F and in turn a positive thermopower. In case of $(CN)_2\,3$ and $NN2$, the LUMO transmission peak is closer to the MMMJ E_F which results in a positive slope of the $\tau(E)$ at the E_F and in turn a negative thermopower. The calculated thermopower values for all these MMMJs are provided in Table 5.4. In case of $(NH_2)_2 3$ and $NN2$, the computed values match very well with experimental values providing additional validation for our computational model.

5.3 Influence of Molecular Length on FMO Reorganization

We would also like to investigate the effect of molecular length on the FMO reorganization. To this end we analyze the M-DoS shift in phenyl ($SS1$), di-phenyl ($SS2$) and tri-phenyl ($SS3$) based MMMJs with dithiol end-group. The HOMO-LUMO energy values corresponding to the isolated molecules is provided in Table 5.1. Accordingly we observe that for all the three molecules, the E_F lies in the HOMO-LUMO energy gap and is closer to the HOMO energy level. The χ value

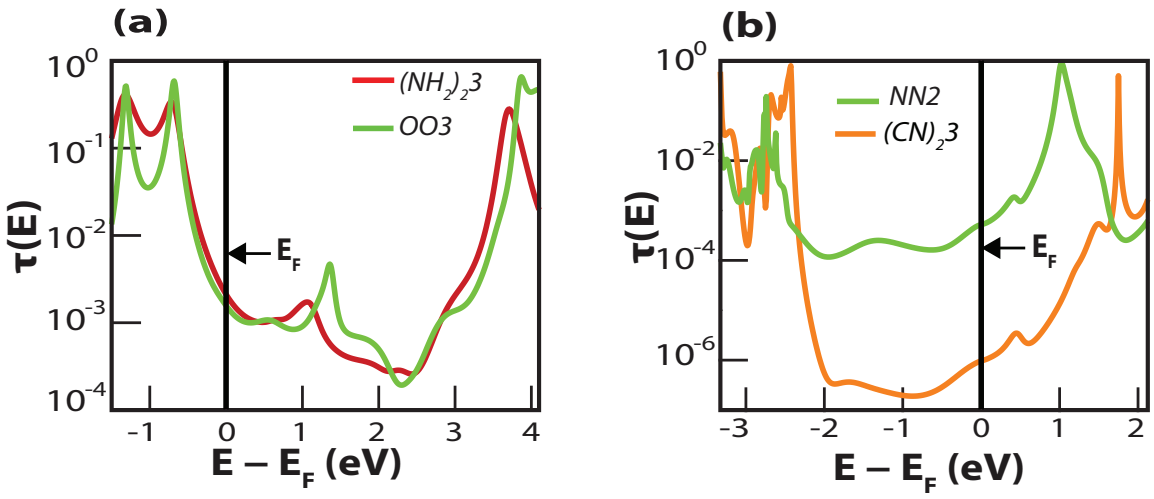

Figure 5.3: (a) (a)Transmission function $tau(E)$ of the MMMJs constructed from $OO3$ and $(NH_2)_23$ molecules exhibiting HOMO dominated (p-type) transport. (b))Transmission function $tau(E)$ of the MMMJs constructed from $(CN)_2\,3$ and $NN2$ molecules exhibiting LUMO dominated (n-type) transport.

of the molecules are higher than those of Au clusters (see Table 5.1) that would result in charge transfer into the molecule. Surprisingly the charge transfer between molecule and Au cluster is almost the same for all three molecules (see Table 5.1). Based on the charge transfer hypothesis, we would expect this to result in a small total-shift and a possible HOMO dominated transport. In fact the computed M-DoS values of these molecules as shown in Figs. 5.4(a)-(b) and 4.3(a) match well with our predictions.

From the figures we can observe that the stabilization effect shifts the M-DOS peaks to lower energies. The shift is stronger for shorter $SS1$ molecule $\left(\Delta\epsilon^H_{SM-IM} = -1.26eV\right)$, $\left(\Delta\epsilon^L_{SM-IM} = -1.58eV\right)$ than the longer $SS3$ molecule $\left(\Delta\epsilon^H_{SM-IM} = -0.77eV\right)$, $\left(\Delta\epsilon^L_{SM-IM} = -1.01eV\right)$. The stabilization shift is due to the physical contact with Au atoms which is mathematically expressed an external perturbing potential V_{Au}. The closer the Au atoms are to the molecule, the stronger is the potential V_{Au} expe-

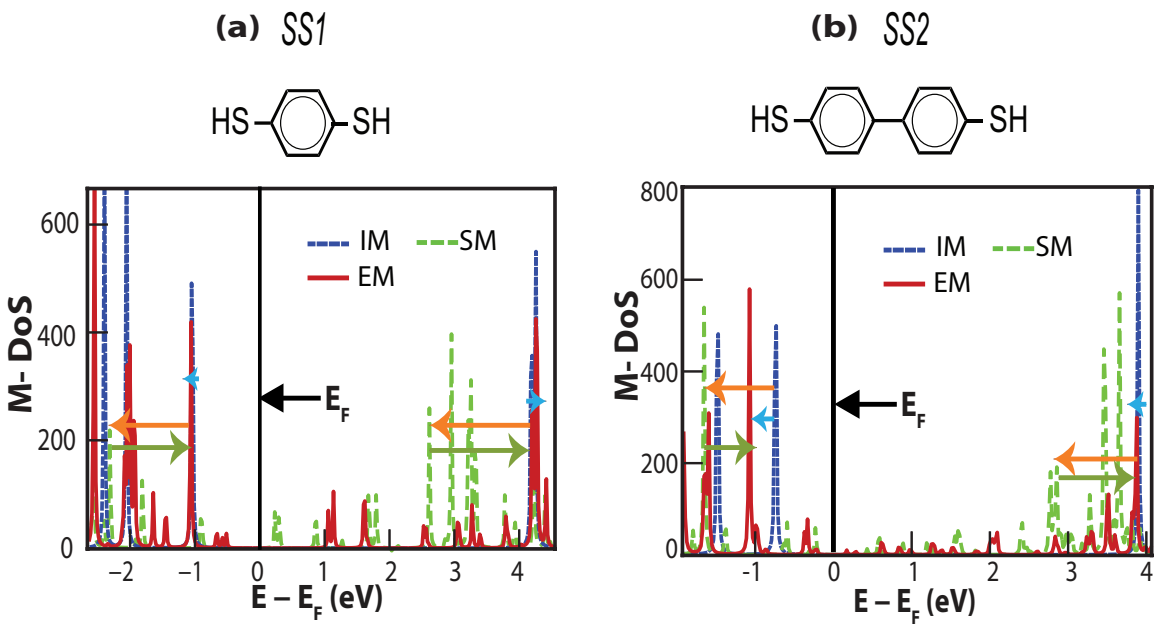

Figure 5.4: (a) M-DoS of $SS1$ molecule in different scenarios (IM, SM and EM systems). (b) M-DoS of $SS2$ molecule in different scenarios. The orange arrow indicates the shift due to stabilization effect. The green arrow indicates the shift due to charge transfer effect and the blue arrow indicates the total-shift of the M-DoS peaks.

rienced by the molecule which results in a larger reorganization. The proximity of Au atoms to the molecule in the computational model can be determined by the distance of the Au cluster centroid to the molecular centroid. As we can observe from Table 5.1, the centroid distance is smaller for shorter molecules in turn resulting in a large stabilization shift.

To analyze the influence of molecular length on the charge transfer effect, we compare the charge transfer values of $SS1$-$SS3$ molecules as shown in Table 5.1. Here we observe that all the dithiol molecules have a net charge gain from the Au cluster. The charge gain increases the e-e interaction in the molecule which in turn shifts (charge transfer effect) the M-DOS peaks to higher energies. Further we also observe that although the amount of charge transferred ΔN is the same for all the

molecules, the shift due to charge transfer is stronger for the shorter $SS1$ molecule than compared to the longer $SS3$ molecule. This phenomenon can be easily explained by a classical dipole moment analysis.

Since the stabilization and charge transfer effects are competing with one another in a charge gaining molecule, it is not possible to predict the total shift of the energy levels as a function of molecular length. However for charge losing molecules, where these effects are complementary, the total shift of the energy levels will be stronger for the shorter molecules. This prediction is valid provided the molecules have the same contact model and same charge transfer values.

5.4 Efficient Computation of the Energy Level Reorganization

The charge transfer hypothesis is effective in qualitatively predicting the extent of reorganization of the FMOs with very little computational cost. However, it does not provide insights into the quantitative aspects of these shifts, which are sensitive to the detailed electronic-structure of the molecular junctions. In prior works, quantitative models based on interface dipoles[14,34,39] have been proposed to study the effect of charge redistribution on the FMOs, and, in particular, have been employed to compute the injection barriers (holes and electrons) in organo-metallic interfaces in the context of light emitting diodes and photovoltaics[23,9]. However, these models were found to be insufficient in accurately predicting quantitative aspects of the reorganization of FMOs in the MMMJs.

To this end, we propose an efficient, iterative approach, allowing for charge transfer, to compute the quantitative reorganization of FMOs. Our starting point is the computation of the electronic-structure of the SM, which quantifies the shift in the density of states (DoS) of the molecule due to the perturbing potential of Au

clusters. Similarly, we compute the shift in the DoS of Au cluster due to the perturbing potential of the molecule. Using the resulting DoS of the molecule and Au cluster, the charge redistribution is determined by imposing a common chemical potential for the molecule and Au clusters such that the total number of electrons on the molecule and Au clusters is fixed. However, upon the charge redistribution, the DoS is perturbed and thus recomputed, and our calculation proceeds as a self-consistent iteration. We use a DIIS mixing scheme[54,24] to accelerate the convergence. We note that, upon the convergence of this self consistent iteration, we recover electronic-structure of the EM. However, as will be demonstrated subsequently, only a few iterations —typically $3-4$ iterations (which correspond to a SCF tolerance of 10^{-4} in electron density)— were needed to compute the location of the FMOs to a reasonable accuracy, as compared to ~ 30 iterations for full SCF convergence (corresponding to a SCF tolerance of 10^{-8}). A flowchart of this computational approach is provided in Fig. 5.5.

We employed the aforementioned approach to estimate the reorganization of FMOs resulting from the combined effects of stabilization and charge transfer. In all our calculations, we only used four iterations in the self-consistent procedure, and denote the resulting state of the molecular system as $\widehat{EM}$. The resulting electronic-structure of $\widehat{EM}$ is used to compute the M-DoS, and estimate the shift of FMOs and the charge transfer between the molecule and the Au clusters. The computed charge transfer, $\widehat{\Delta N} = N_{IM} - N_{\widehat{EM}}$, for all the molecules considered in the present work is reported in Table 5.1. The computed total shift in the energies of FMOs, $\Delta\epsilon^{H/L}_{\widehat{EM}-IM} = \epsilon^{H/L}_{\widehat{EM}} - \epsilon^{H/L}_{IM}$, are reported in Table 5.3. The comparison between the M-DoS of EM and $\widehat{EM}$ are provided in Figs. 5.6 and 5.7. As evident from the results, the computed charge transfer and the shift of FMOs using the proposed

technique are in very good agreement with our calculations using the electronic-structure of EM. Thus, the proposed approach presents a computationally efficient way to quantify the FMO reorganization. Further, since the electronic-structure of an IM and that of the metallic clusters representing the contact electrodes are the sole inputs to the proposed calculation, the present approach can also be used for high-throughput screening calculations to identify combinations of molecules and electrodes with desired transport properties.

Property	$SS1$	$SS2$	$SS3$	$(NC)_2 3$	$OO3$	$(CN)_2 3$	$(NH_2)_2 3$	$NN2$
ϵ^H_{IM}(eV)	-6.25	-5.93	-5.85	-6.56	-5.72	-6.76	-4.93	-7.17
ϵ^L_{IM}(eV)	-1.00	-1.3	-1.42	-2.25	-1.13	-2.45	-0.70	-2.04
ΔN	-0.32	-0.30	-0.28	0.34	-0.12	0.2	0.31	0.25
$\widehat{\Delta N}$	-0.35	-0.34	-0.31	0.35	-0.16	0.19	0.35	0.26
χ(eV)	6.00	5.45	5.23	4.39	5.35	4.59	2.70	4.56
$\lvert C_{Au(L/R)} - C_{Mol} \rvert$ (A°)	11.00	13.13	15.27	18.18	14.28	18.20	14.73	13.26

Table 5.1: Energies of the HOMO (ϵ^H_{IM}) and the LUMO(ϵ^L_{IM}) of IM, charge transfer (ΔN, $\widehat{\Delta N}$), electronegativity (χ) and the distance between the centroid of Au cluster (left/right) and the centroid of molecule ($\left|C_{Au(L/R)} - C_{Mol}\right|$) for all molecules.

M-DoS Shift	$SS1$	$SS2$	$SS3$	$(NC)_2 3$	$OO3$	$(CN)_2 3$	$(NH_2)_2 3$	$NN2$
$\Delta\epsilon^H_{SM-IM}$(eV)	-1.26	-0.92	-0.77	-0.21	-0.86	-0.12	-0.55	-1.55
$\Delta\epsilon^L_{SM-IM}$(eV)	-1.58	-1.12	-1.01	-0.73	-1.40	-0.54	-0.50	-1.35
$\Delta\epsilon^H_{EM-SM}$(eV)	1.27	0.59	0.50	-0.54	0.66	-0.54	-0.43	-0.68
$\Delta\epsilon^L_{EM-SM}$(eV)	1.57	1.10	0.84	-0.18	1.25	-0.28	-0.30	-0.55

Table 5.2: The reorganization of FMOs due to the individual effects of stabilization $\left(\Delta\epsilon^H_{SM-IM}/\ \Delta\epsilon^L_{SM-IM}\right)$ and charge transfer $\left(\Delta\epsilon^H_{EM-SM}/\ \Delta\epsilon^H_{EM-SM}\right)$ for all molecules.

M-DoS Shift	$SS1$	$SS2$	$SS3$	$(NC)_2 3$	$OO3$	$(CN)_2 3$	$(NH_2)_2 3$	$NN2$
$\Delta\epsilon^H_{EM-IM}$(eV)	0.01	-0.33	-0.27	-0.75	-0.20	-0.66	-0.98	-2.23
$\Delta\epsilon^L_{EM-IM}$(eV)	-0.01	-0.02	-0.17	-0.91	-0.15	-0.82	-0.80	-1.90
$\Delta\epsilon^H_{\widehat{EM-IM}}$(eV)	0.06	-0.16	-0.20	-0.75	-0.02	-0.7	-0.95	-2.30
$\Delta\epsilon^L_{\widehat{EM-IM}}$(eV)	-0.03	-0.08	-0.11	-0.91	-0.09	-0.85	-0.75	-1.98

Table 5.3: The overall shift of the FMOs (due to both stabilization and charge transfer) using the full self-consistent calculation (EM) $\left(\Delta\epsilon^H_{EM-IM}\middle/\Delta\epsilon^L_{EM-IM}\right)$, and using the iterative approach ($\widehat{EM}$) $\left(\Delta\epsilon^H_{\widehat{EM-IM}}\middle/\Delta\epsilon^L_{\widehat{EM-IM}}\right)$ for all molecules.

System	**Thermopower**(S) (μV/K)		
	This work	Experiments	Past computations
$OO3$	19.9	-	26.5[5]
$(NC)_2 3$	-3.0	-1.0 ± 0.4[a 69]	-1.6[69]
$(CN)_2 3$	-9.2	-	-6.8[5]
$(NH_2)_2 3$	23.9	6.4 $\pm$0.4[41]	22.5[5],24.3[b 55]
$NN2$	-8.8	$-9.5(4.3)$[c 78]	-7.88[78]

Table 5.4: Thermopower of all the molecular junctions obtained from this work, and comparison with past experimental measurements and computations. [a] The experimental value corresponds to tribenzene monoisocyanide. [b] The computed value neglects the interactions beyond the mean field. [c] The experimental uncertainty is quoted in terms of half-width at half-maximum.

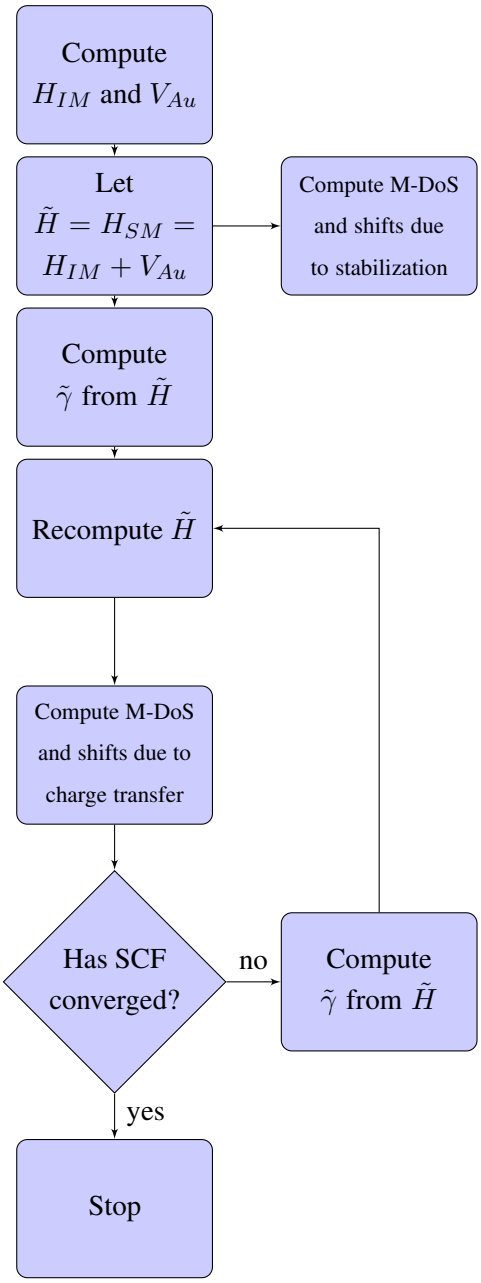

Figure 5.5: Flowchart of the proposed iterative scheme to compute the reorganization of FMOs.

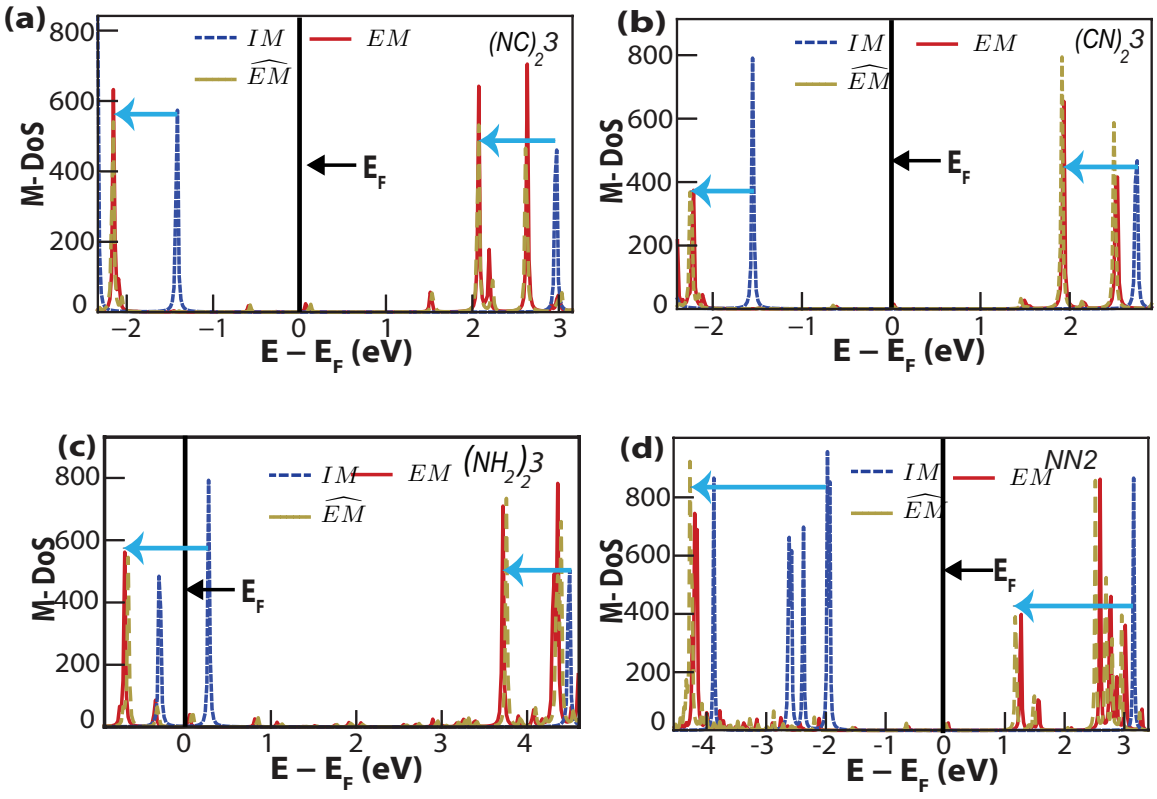

Figure 5.6: Comparison of the M-DoS of the EM and $\widehat{EM}$ for molecules that lose charge (namely $(NC)_2 3$, $(CN)_2 3$, $(NH_2)_2 3$ and $NN2$). As observed from the figure, the peaks in the M-DoS, representing the FMOs of $\widehat{EM}$ are in good agreement with those of EM.

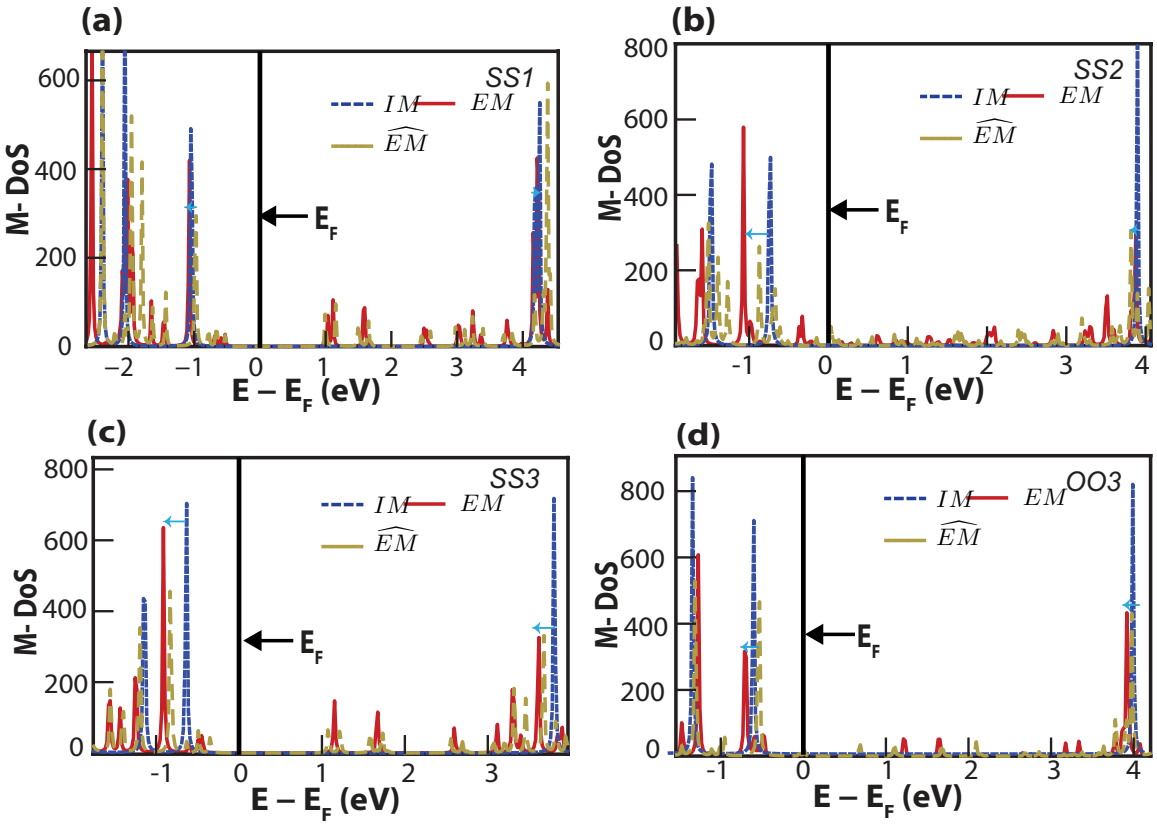

Figure 5.7: Comparison of the M-DoS of the EM and $\widehat{EM}$ for molecules that gain charge (namely $SS1$, $SS2$, $SS3$ and $OO3$). As observed from the figure, the peaks in the M-DoS, representing the FMOs of $\widehat{EM}$ are in agreement with those of EM.

CHAPTER VI

Conclusion

6.1 Summary

To summarize, we had performed carefully designed ab-initio based computational studies to understand the influence of molecular structure on the electronic-structure of metal-molecule-metal heterojunctions (MMMJs) and in turn its thermoelectric properties. As a first step in chapter II, we explain the recent experimental investigations performed by our collaborators on aromatic molecules based MMMJs. These experiments observed that a triphenyl molecule with thiol end-group had a positive thermopower (HOMO dominated or p-type transport) whereas the same molecule with an isocyanide end-group exhibited a negative thermopower (LUMO or n-type transport). Explaining this result by understanding the electronic-structure origins of the end-groups influence on the MMMJ thermopower was the focus of this dissertation.

In the next chapter (chapter III), we explain the Landauer formalism which can systematically explain the electronic transport dominated by quantum mechanical effects. This formalism enables us to calculate the MMMJ transport properties (such as current I_{Tot}, conductance G and thermopower S) from its transmission function

$\tau(E)$. The $\tau(E)$ describes the probability of an electron with energy E to transmit across the molecule. The $\tau(E)$ of MMMJs made up of real molecules and electrode atoms can be computed from the Hamiltonian and the Green's function of the electrodes and that of the extended molecular system.

The Hamiltonian of the computational model was computing at the DFT level by employing an accurate hybrid exchange-correlation functional (B3LYP) and atom-centered basis functions (LANL2DZ). The model that we developed was able to systematically represent the chemical binding between the molecular end-group and the Au atoms. Further, the model was able to remove the surface effects by projecting the Hamiltonian into a smaller subspace. Finally, the model was able to quantitatively predict the thermopower for a wide range of aromatic molecule based MMMJs with very good accuracy.

In chapter IV, we describe the systematic computational analysis to understand how the molecular end-groups influence the MMMJ electronic-structure (particularly the energy level reorganization) and in turn the MMMJ transport properties. An extensive analysis of the electronic-structure employing computational models has enabled us to propose the charge transfer (CT) hypothesis which elucidated this influence. According to the hypothesis, the molecular energy level reorganization is influenced by two important effects: (i) the stabilization of energy levels induced by the physical contact to the Au cluster; (ii) the charge transfer effect due to the chemical interaction between the molecule and the Au atoms to neutralize the chemical potential. The stabilization effect shifts the energy levels to lower energies where the influence of charge transfer effect depends on the direction of charge transfer. In charge gaining molecules, the charge transfer effect pushes the energy levels to higher energies. This results in the stabilization and charge-transfer effect opposing

one another in turn resulting in a small magnitude of total shift (reorganization). However in charge losing molecules, the charge transfer effect pushes the energy levels to further lower energies. This results in the stabilization and charge-transfer effect complementing one another, in turn resulting in a small magnitude of total shift (reorganization). The proposed hypothesis was computationally validated by independently quantifying the influence of stabilization and charge transfer effects on the energy level reorganization. This delineation provided a convincing validation to the CT hypothesis.

Finally in chapter V, we test the generality of the CT hypothesis by using the hypothesis to predict the total shift of energy levels for various aromatic molecule based MMMJs. In all these cases, the hypothesis was able to predict the nature of total shift of FMOs and in turn the nature of transport. Although the CT hypothesis is effective in qualitatively predicting the magnitude of the energy level reorganization, the quantitative reorganization can only be obtained by performing expensive DFT calculations on the extended molecule (EM) system. To this end, we proposed an efficient, iterative approach, that can quantitatively compute the reorganization of molecular energy levels at a fraction of the original computational cost. This quantitative prediction enables us to accurately predict the nature of transport (HOMO or LUMO dominated) and in turn the sign of the thermopower.

6.2 Future Work

6.2.1 High Throughput Analysis

Since the structure of aromatic molecules can be easily modified, it is possible to create a huge set of aromatic molecules by modifying their geometry and chem-

ical composition. Each of these molecules have a unique electronic-structure and a unique HOMO and LUMO energy level. Analyzing such a large collection of molecules to understand their electronic-structure and in turn its influence on the MMMJ thermopower soon becomes prohibitively expensive in a conventional DFT approach. An alternative computationally efficient approach that was proposed in chapter V requires only a fraction of the conventional DFT cost to quantitatively predict the reorganization. Hence this approach can be potentially used as a high throughput screening process to quantitatively predict the total shift of the FMOs and their energetic separation from the MMMJ E_F for a large set of molecules. The molecules whose HOMO or LUMO energy level lies very close to the E_F could then be subjected to further computational and experimental analysis. This approach would not only reduce the computational cost but they would also enable us to target and work with a small sub-set of molecules with the required properties.

6.2.2 Managing Power and Efficiency Requirement

Although alignment of the molecular energy levels as close as possible to the hetero-junction Fermi energy E_F would enable us to obtain very high power factor $\left(S^2\sigma\right)$ and in turn efficiency, a thermoelectric device cannot have practical application if it cannot provide a good output power. Heterojunctions in which the molecules are weakly coupled $(\tau(E) \Rightarrow \delta(E - E_1))$, one could show that the efficiency of the system could reach Carnot efficiency (η_C)[21] in the limit of lattice thermal conductivity (k_{latt}) going to zero. The same system approaches Curzon-Ahlborn efficiency[15,21] at maximum power output. However such weakly coupled system are not of great practical interest due their extremely small power output.

Tightly coupled molecular heterojunctions can have good power output. Un-

fortunately, such tightly coupled heterojunctions suffer from poor efficiency due to the counterflow of cold charge carriers arising from the tail of the transmission function $\tau(E)$. Karlstrom *et.al*[35] argue that non symmetric $\tau(E)$ can enable us to simultaneously have high power output and efficiency. Further, they also provide heuristic argument that such $\tau(E)$ can be realized in real heterojunctions by selecting molecules with almost degenerate frontier energy levels. Amongst these degenerate energy levels, only one of those energy levels being tightly coupled to the electrode atoms resulting in non symmetric $\tau(E)$.

The arguments provided in Karlstrom *et.al*[35] can be systematically extended by developing optimization algorithms that can rigorously describe the nature of $\tau(E)$ for given power and efficiency requirements. Using these theoretical $\tau(E)$ along with the aforementioned high throughput analysis could potentially enable us in identifying real heterojunctions whose transport properties satisfy the required power and efficiency constraints.

6.2.3 Quantitative Prediction of Conductance

As demonstrated in this work the current Green's function approach in the Landauer formalism of transport is able to quantitatively predict the thermopower of MMMJs. However unfortunately this approach is not accurate enough to quantitatively predict the conductance (G) of the MMMJs. In the transport community, this failure is mainly attributed to the inaccuracies of the density functional theory (DFT). Unfortunately the current approach of employing LCAO basis set does not allow us to systematically validate this assumption to ensure that the inaccuracies can be directly attributed to the DFT approximation. However this systematic validation can be achieved through a finite element (FE) based DFT approach. In this

approach, one can use a finite element basis set (comprising of polynomial functions) to solve the Kohn-Sham equations. The advantages of using a finite element basis set is that one can systematically increase the number of basis functions (by reducing the mesh size and increasing the polynomial order) to observe convergence of the ground-state electron density. Further, finite element basis set also enables us to consider arbitrary boundary conditions (for DFT – both homogeneous Dirichlet and periodic boundary conditions). Finally, the finite element basis set would enable us to write massively parallel programs which would enable us to simulate MMMJs with a large number of metal (Au) atoms to accurately capture the chemical interaction between the molecule and metal atoms. Finite element based Kohn-Sham DFT codes have been developed by our collaborators[44] which has been used to compute the ground-state electron density of thousands of metal atoms[44]. In future, it would be worthwhile to explore using finite element based KS-DFT approach to systematically control the modeling and basis set errors to observe convergence of the MMMJ electronic-structure and in turn its conductance. This systematic control of numerical and modeling errors would enable us to unambiguously identify the source of the errors in predicting MMMJ conductance— i.e., do the model/basis-set assumptions have a dominant contribution or if it is a fundamental limitation of DFT level approximation. Answering this question unambiguously is crucial in order to develop computational models that can quantitatively predict the conductance and in turn the power factor, which is an important step towards realizing a nano-scale thermoelectric device.

APPENDICES

APPENDIX A

Transport Characterization through Dominant Conduction Orbital

In this Appendix, we characterize the transport mechanism of aromatic molecules by comparing the orbitals of the molecules in an isolated environment (IM) and those of the molecules in contact with Au electrode atoms (MMMJs or its computational representation–open quantum system OQS). Three molecules are considered for transport characterization namely the triphenyl dihydroxyl $OO3$, triphenyl dinitrile $(CN)_2\,3$ and triphenyl diamine $(NH_2)_2\,3$. The transmission function $\tau(E)$ computed for metal-molecule-metal heterojunctions (MMMJs) based on these molecules show that in case of $OO3$ and $(NH_2)_2\,3$, the HOMO transmission peak is closer to the MMMJ E_F. However in case of $(CN)_2\,3$ based MMMJ, the LUMO transmission peak is closer to the MMMJ E_F.

We characterize the electronic structure of $OO3$ and $(NH_2)_2\,3$ by analyzing the electronic structure of the open quantum system (the computational model that is representative of MMMJ) at the energy corresponding to the HOMO transmission peak. The electronic structure analysis is performed by spectrally decomposing the

transmission matrix at the energies of interest. The process of analyzing the electronic structure of the open quantum system is described in detail elsewhere[50]. In both the HOMO dominated molecular heterojunctions considered here, a single eigenchannel, referred to as the dominant conduction orbital (DCO), contributes to more than 99% of transport. The DCOs of the $OO3$ and $(NH_2)_2\,3$ based MMMJs calculated at their respective transmission peak energies are shown in Fig. A.1. It can be observed from Fig. A.1 that these DCO's exhibit π bonding, very closely resembling the HOMO molecular orbitals of their respective isolated molecular systems (see Fig. A.1).

The electronic structure of the $(CN)_2\,3$ based open quantum system (MMMJ) was similarly analyzed at the energy corresponding the LUMO transmission peak. The DCOs of this MMMJ (see Fig. A.2) contributing to more than 99.5% of transport exhibit the π bonding closely resembling the LUMO molecular orbital of the $(CN)_2\,3$ isolated molecule as shown in Fig. A.2.

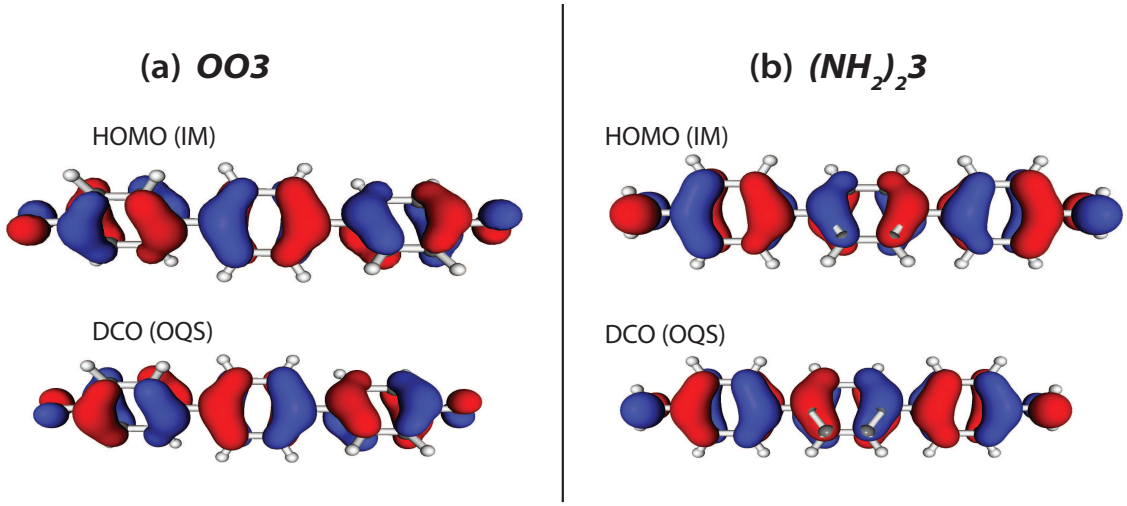

Figure A.1: ((a) Plots comparing the HOMO orbital of triphenyl dihydroxyl $OO3$ molecule in an isolated environment and the DCO of the same molecule in the presence of metal electrodes (MMMJs) at the HOMO transmission peak energies. (b) Plots comparing the HOMO orbital of triphenyl diamine $(NH_2)_2\,3$ molecule in an isolated environment and the DCO of the same molecule in the presence of metal electrodes (MMMJs) at the HOMO transmission peak energies.

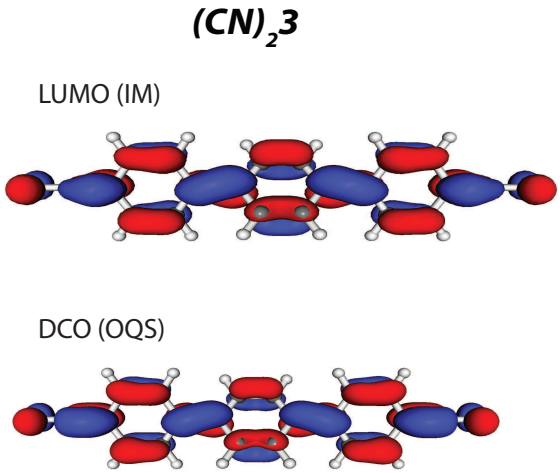

Figure A.2: (Plots comparing the LUMO orbital of the triphenyl dinitrile $(CN)_2\,3$ molecule in an isolated environment and the DCO of the same molecule in the presence of metal electrodes (MMMJs) at the LUMO transmission peak energies.

APPENDIX B

Comparing Energy Level Reorganization in EM and OQS Systems

Chapter IV, explained how the reorganization of the energy levels of a molecule in contact with the metal (Au) electrode atoms can be computed by comparing the M-DoS of the molecule in an isolated enviornment (*aka* isolated molecule, IM), in presence of a finite Au cluster (*aka* extended molecule, EM) and when the extended molecule is brough into contact with the semi-infinite electrode through the self-energy operators $\hat{\Sigma}_{L/R}$ (*aka* open quantum system, OQS). The M-DoS comparison of triphenyl dithiol $SS3$ and triphenyl diisocyanide $(NC)_2\,3$ based systems (see Fig. 4.1) showed that the energy level reorganization (observed through the shift of M-DoS peaks) was completely captured by the extended molecule (EM). In this appendix, we show that this observation was true for other aromatic molecule based MMMJs where the molecule is brought into contact with Au electrode atoms.

Similar to the analysis explained in Chapter IV, we calculate the M-DoS of triphenyl dihydroxyl $OO3$, triphenyl dinitrile $(NC)_2\,3$ and triphenyl diamine $(NH_2)_2\,3$ in three different scenarios namely the IM, EM and open quantum systems. The

computed M-DoS values for these molecules are shown in Fig. B.1. It can be observed from Fig. B.1 that in case $(NC)_2\,3$ and $(NH_2)_2\,3$ molecules, the molecules have a higher electronegativity χ compared to the Au clusters (see Table 5.1). Hence, these molecules lose electronic charge $\Delta N > 0$ to the Au atoms (see Table 5.1). As a result, the energy levels (characterized by M-DoS peaks) of these molecules experience a large total-shift to lower energies.

On the other hand, the χ value for $OO3$ molecule is higher than the Au cluster, which results in a charge gain $\Delta N < 0$ by these molecules from Au atoms (see Table 5.1). The charge gain results in a competing stabilization and charge transfer effect which results in a small total-shift of the energy levels characterized by its M-DoS peaks. Finally, similar to $SS3$ and $(NC)_2\,3$ molecules analyzed in chapter IV, the shift in the M-DoS is captured in its entirety by the extended molecule. This analysis suggests that our methodology of employing the electronic structure (M-DoS) of the extended molecule in chapters IV and V is a valid assumption.

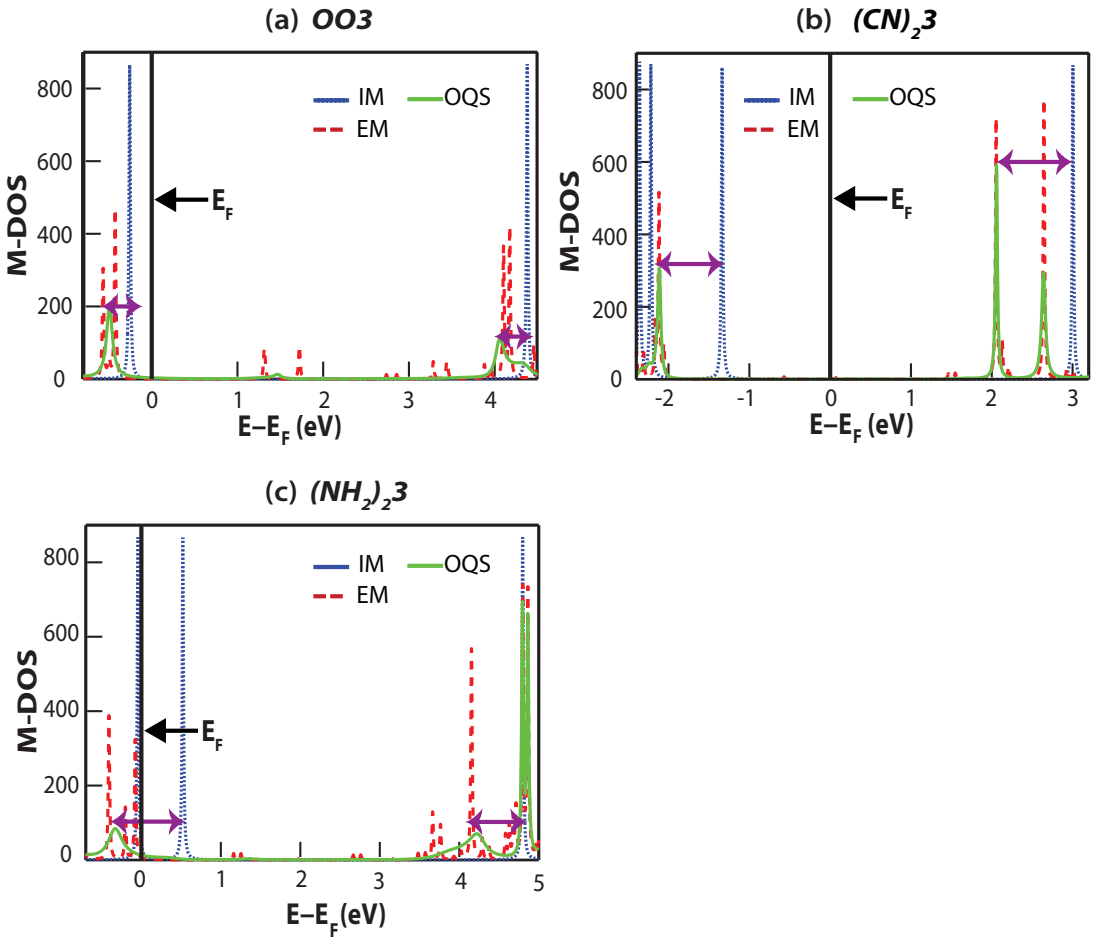

Figure B.1: (a) M-DoS of triphenyl dihydroxyl $OO3$ molecule in different scenarios (namely isolated molecule IM, extended molecule EM and open quantum system OQS). (b) M-DoS of triphenyl dinitrile $(CN)_2\,3$ molecule in different scenarios. (c) M-DoS of triphenyl diamine $(NH_2)_2\,3$ molecule in different scenarios. The M-DOS of the IM, EM and open quantum system are denoted by blue-dotted line, red-dashed line and green-continuous curves respectively. The purple arrows indicate the magnitude of the M-DOS shift.

BIBLIOGRAPHY

BIBLIOGRAPHY

[1] U.S Energy Information Administration. Annual energy review 2011. Technical Report DOE/EIA-0384(2011).

[2] Neil W Ashcroft and N David Mermin. Solid state phys. Saunders, Philadelphia, 1976.

[3] Arieh Aviram and Mark A Ratner. Molecular rectifiers. Chemical Physics Letters, 29(2):277–283, 1974.

[4] Kanhayalal Baheti, Jonathan A. Malen, Peter Doak, Pramod Reddy, Sung-Yeon Jang, T. Don Tilley, Arun Majumdar, and Rachel A. Segalman. Probing the chemistry of molecular heterojunctions using thermoelectricity. Nano Lett., 8(2):715–719, 2008.

[5] Janakiraman Balachandran, Pramod Reddy, Barry D Dunietz, and Vikram Gavini. End-group-induced charge transfer in molecular junctions: Effect on electronic-structure and thermopower. J. Phys. Chem. Lett., 3(15):1962–1967, 2012.

[6] A.D. Becke. Density-functional thermochemistry. iii. the role of exact exchange. J. Chem. Phys., 98(1):5648–5652, 1993.

[7] A.D. Becke. A new mixing of hartree-fock and local density-functional theories. J. Chem. Phys., 98(2):1372–1377, 1993.

[8] Jeremy M Beebe, BongSoo Kim, C Daniel Frisbie, and James G Kushmerick. Measuring relative barrier heights in molecular electronic junctions with transition voltage spectroscopy. Acs Nano, 2(5):827–832, 2008.

[9] M. G. Betti, A. Kanjilal, C. Mariani, H. Vázquez, Y. J. Dappe, J. Ortega, and F. Flores. Barrier formation at organic interfaces in a cu(100)-benzenethiolate-pentacene heterostructure. Phys. Rev. Lett., 100:027601, Jan 2008.

[10] CM Bhandari and DM Rowe. Boundary scattering of phonons. Journal of Physics C: Solid State Physics, 11(9):1787, 1978.

[11] Th Caillat, J-P Fleurial, and A Borshchevsky. Preparation and thermoelectric properties of semiconducting zn¡ sub¿ 4¡/sub¿ sb¡ sub¿ 3¡/sub¿. Journal of Physics and Chemistry of Solids, 58(7):1119–1125, 1997.

[12] Herbert B Callen. The application of onsager's reciprocal relations to thermoelectric, thermomagnetic, and galvanomagnetic effects. Physical Review, 73(11):1349, 1948.

[13] M. Christensen, G. Jeffrey Snyder, and B.B. Iversen. High temperature thermoelectric properties of czochralski-pulled ba8ga16ge30. In Thermoelectrics, 2006. ICT '06. 25th International Conference on, pages 40–43, Aug 2006.

[14] Xavier Crispin, Victor Geskin, Annica Crispin, Jrme Cornil, Roberto Lazzaroni, William R. Salaneck, and Jean-Luc Bredas. Characterization of the interface dipole at organic/metal interfaces. J. Am. Chem. Soc., 124(27):8131–8141, 2002.

[15] FL Curzon and B Ahlborn. Efficiency of a carnot engine at maximum power output. American Journal of Physics, 43(1):22–24, 1975.

[16] Supriyo Datta. Nanoscale device modeling: The green's function method. Superlattice. Microst., 28(4):253–278, 2000.

[17] Supriyo Datta. Quantum transport: atom to transistor. Cambridge University Press, 2005.

[18] M. Di Ventra. Electrical transport in nanoscale systems. Cambridge: Cambridge University Press, 2008.

[19] ZH Dughaish. Lead telluride as a thermoelectric material for thermoelectric power generation. Physica B: Condensed Matter, 322(1):205–223, 2002.

[20] Vincent B. Engelkes, Jeremy M. Beebe, and C. Daniel Frisbie. Length-dependent transport in molecular junctions based on sams of alkanethiols and alkanedithiols: Effect of metal work function and applied bias on tunneling efficiency and contact resistance. J. Am. Chem. Soc., 126(43):14287–14296, 2004.

[21] Massimiliano Esposito, Katja Lindenberg, and Christian Van den Broeck. Thermoelectric efficiency at maximum power in a quantum dot. EPL (Europhysics Letters), 85(6):60010, 2009.

[22] Mike Finnis. Interatomic forces in condensed matter, volume 1. Oxford University Press, 2003.

[23] F. Flores, J. Ortega, and H. Vazquez. Modelling energy level alignment at organic interfaces and density functional theory. Phys. Chem. Chem. Phys., 11:8658–8675, 2009.

[24] M. J. Frisch, G. W. Trucks, H. B. Schlegel, G. E. Scuseria, M. A. Robb, J. R. Cheeseman, G. Scalmani, V. Barone, B. Mennucci, G. A. Petersson, and *et al*. Gaussian 09 Revision D.01, 2009.

[25] HJ Goldsmid and JW Sharp. Estimation of the thermal band gap of a semiconductor from seebeck measurements. Journal of electronic materials, 28(7):869–872, 1999.

[26] David H Griffel. Applied functional analysis. Courier Dover Publications, 2012.

[27] P.J. Hay and W.R. Wadt. Ab initio effective core potentials for molecular calculations. potentials for k to au including the outermost core orbitals. J. Chem. Phys., 82:299, 1985.

[28] P.J. Hay and W.R. Wadt. *Ab initio* effective core potentials for molecular calculations. potentials for the transition metal atoms sc to hg. J. Chem. Phys., 82(1):270–283, 1985.

[29] Khang Hoang, Keyur Desai, and S. D. Mahanti. Charge ordering and self-assembled nanostructures in a fcc coulomb lattice gas. Phys. Rev. B, 72:064102, Aug 2005.

[30] P. Hohenberg and W. Kohn. Inhomogeneous electron gas. Phys. Rev., 136:B864–B871, Nov 1964.

[31] Kuei Fang Hsu, Sim Loo, Fu Guo, Wei Chen, Jeffrey S Dyck, Ctirad Uher, Tim Hogan, EK Polychroniadis, and Mercouri G Kanatzidis. Cubic agpbmsbte2+ m: Bulk thermoelectric materials with high figure of merit. Science, 303(5659):818–821, 2004.

[32] TE Humphrey and H Linke. Reversible thermoelectric nanomaterials. Physical review letters, 94(9):096601, 2005.

[33] Abram Fedorovich Ioffe. Semiconductor thermoelements and thermoelectric cooling. Infosearch London, 1957.

[34] Hisao Ishii, Kiyoshi Sugiyama, Eisuke Ito, and Kazuhiko Seki. Energy level alignment and interfacial electronic structures at organic/metal and organic/organic interfaces. Adv. Mater., 11(8):605–625, 1999.

[35] Olov Karlström, Heiner Linke, Gunnar Karlström, and Andreas Wacker. Increasing thermoelectric performance using coherent transport. Physical Review B, 84(11):113415, 2011.

[36] San-Huang Ke, Weitao Yang, Stefano Curtarolo, and Harold U. Baranger. Thermopower of molecular junctions: An *Ab initio* study. Nano Lett., 9(3):1011–1014, 2009.

[37] W. Kohn and L. J. Sham. Self-consistent equations including exchange and correlation effects. Phys. Rev., 140:A1133–A1138, Nov 1965.

[38] Rolf Landauer. Spatial variation of currents and fields due to localized scatterers in metallic conduction. IBM Journal of Research and Development, 1(3):223–231, 1957.

[39] Francois Léonard and J. Tersoff. Role of fermi-level pinning in nanotube schottky diodes. Phys. Rev. Lett., 84:4693–4696, May 2000.

[40] GD Mahan and JO Sofo. The best thermoelectric. Proceedings of the National Academy of Sciences, 93(15):7436–7439, 1996.

[41] Jonathan A. Malen, Peter Doak, Kanhayalal Baheti, T. Don Tilley, Rachel A. Segalman, and Arun Majumdar. Identifying the length dependence of orbital alignment and contact coupling in molecular heterojunctions. Nano Lett., 9(3):1164–1169, 2009.

[42] B Mann, H Kuhn, and LV Szentpaly. Tunnelling through fatty acid monolayers and its relevance to photographic sensitization. Chemical Physics Letters, 8(1):82–84, 1971.

[43] Artem Mishchenko, Linda A. Zotti, David Vonlanthen, Marius Burkle, Fabian Pauly, Juan Carlos Cuevas, Marcel Mayor, and Thomas Wandlowski. Single-molecule junctions based on nitrile-terminated biphenyls: A promising new anchoring group. J. Am. Chem. Soc., 133(2):184–187, 2011.

[44] Phani Motamarri, Michael R Nowak, Kenneth Leiter, Jaroslaw Knap, and Vikram Gavini. Higher-order adaptive finite-element methods for kohn–sham density functional theory. Journal of Computational Physics, 253:308–343, 2013.

[45] R.S Mulliken. A new electroaffinity scale; together with data on valence states and on valence ionization potentials and electron affinities. J. Chem. Phys., 2(11):782–793, 1934.

[46] Abraham Nitzan and Mark A. Ratner. Electron transport in molecular wire junctions. Science, 300(5624):1384–1389, 2003.

[47] Intergovernmental Panel on Climate Change. Fifth assessment report: Climate change 2013- the physical science basis. Technical report.

[48] Jiwoong Park, Abhay N Pasupathy, Jonas I Goldsmith, Connie Chang, Yuval Yaish, Jason R Petta, Marie Rinkoski, James P Sethna, Héctor D Abruña, Paul L McEuen, et al. Coulomb blockade and the kondo effect in single-atom transistors. Nature, 417(6890):722–725, 2002.

[49] RG Parr and W Yang. Dft of atoms and molecules, 1989.

[50] Magnus Paulsson and Mads Brandbyge. Transmission eigenchannels from nonequilibrium green's functions. Phys. Rev. B, 76:115117, Sep 2007.

[51] Magnus Paulsson and Supriyo Datta. Thermoelectric effect in molecular electronics. Phys. Rev. B, 67:241403, Jun 2003.

[52] F. Pauly, J. K. Viljas, and J. C. Cuevas. Length-dependent conductance and thermopower in single-molecule junctions of dithiolated oligophenylene derivatives: A density functional study. Phys. Rev. B, 78:035315, Jul 2008.

[53] Guowen Peng, Mikkel Strange, Kristian S. Thygesen, and Manos Mavrikakis. Conductance of conjugated molecular wires: Length dependence, anchoring groups, and band alignment. J. Phys. Chem. C, 113(49):20967–20973, 2009.

[54] Peter Pulay. Improved scf convergence acceleration. J. Comput. Chem., 3(4):556–560, 1982.

[55] Su Ying Quek, Hyoung Joon Choi, Steven G. Louie, and Jeffrey B. Neaton. Thermopower of amine-gold-linked aromatic molecular junctions from first principles. ACS Nano, 5(1):551–557, 2011.

[56] Pramod Reddy, Sung-Yeon Jang, Rachel A. Segalman, and Arun Majumdar. Thermoelectricity in molecular junctions. Science, 315(5818):1568–1571, 2007.

[57] Pramod Sangi Reddy. Transport of Charge and Energy in Metal-molecule-metal Junctions. PhD thesis, 2007.

[58] A.E. Reed, R.B. Weinstock, and F. Weinhold. Natural population analysis. J. Chem. Phys., 83(2):735–746, 1985.

[59] Mark A Reed, C Zhou, CJ Muller, TP Burgin, and JM Tour. Conductance of a molecular junction. Science, 278(5336):252–254, 1997.

[60] David Michael Rowe. CRC handbook of thermoelectrics. CRC press, 1995.

[61] M P Lopez Sancho, J M Lopez Sancho, J M L Sancho, and J Rubio. Highly convergent schemes for the calculation of bulk and surface green functions. J. Phys. F: Met. Phys., 15(4):851, 1985.

[62] Y. Shao, L. Fusti-Molnar, Y. Jung, J. Kussmann, C. Ochsenfeld, S. T. Brown, A. T. B. Gilbert, L. V. Slipchenko, S. V. Levchenko, D. P. O'Neill, and *et al.* Advances in methods and algorithms in a modern quantum chemistry program package. Phys. Chem. Chem. Phys., 8(27):3172–3191, 2006.

[63] Q Shen, L Chen, T Goto, T Hirai, J Yang, GP Meisner, and C Uher. Effects of partial substitution of ni by pd on the thermoelectric properties of zrnisn-based half-heusler compounds. Applied Physics Letters, 79(25):4165–4167, 2001.

[64] Emanuel Andrew Skrabek and Donald Smith Trimmer. Thermoelectric device including an alloy of gete and agsbte as the p-type element, March 23 1976. US Patent 3,945,855.

[65] Joseph R Sootsman, Duck Young Chung, and Mercouri G Kanatzidis. New and old concepts in thermoelectric materials. Angewandte Chemie International Edition, 48(46):8616–8639, 2009.

[66] Joseph R Sootsman, Robert J Pcionek, Huijun Kong, Ctirad Uher, and Mercouri G Kanatzidis. Strong reduction of thermal conductivity in nanostructured pbte prepared by matrix encapsulation. Chemistry of materials, 18(21):4993–4995, 2006.

[67] R. Stadler and K. W. Jacobsen. Fermi level alignment in molecular nanojunctions and its relation to charge transfer. Phys. Rev. B, 74:161405, Oct 2006.

[68] Aaron Tan, Janakiraman Balachandran, Barry D. Dunietz, Sung-Yeon Jang, Vikram Gavini, and Pramod Reddy. Length dependence of frontier orbital alignment in aromatic molecular junctions. Appl. Phys. Lett., 101(24):243107, 2012.

[69] Aaron Tan, Janakiraman Balachandran, Seid Sadat, Vikram Gavini, Barry D. Dunietz, Sung-Yeon Jang, and Pramod Reddy. Effect of length and contact chemistry on the electronic structure and thermoelectric properties of molecular junctions. J. Am. Chem. Soc., 133(23):8838–8841, 2011.

[70] Aaron Tan, Seid Sadat, and Pramod Reddy. Measurement of thermopower and current-voltage characteristics of molecular junctions to identify orbital alignment. Appl. Phys. Lett., 96(1):013110, 2010.

[71] Xinfeng Tang, Qingjie Zhang, Lidong Chen, Takashi Goto, and Toshio Hirai. Synthesis and thermoelectric properties of p-type-and n-type-filled skutterudite rymxco4- xsb12 (r: Ce, ba, y; m: Fe, ni). Journal of Applied Physics, 97(9):093712, 2005.

[72] W. Tian, S. Datta, S. Hong, R. Reifenberger, J.I. Henderson, and C.P. Kubiak. Conductance spectra of molecular wires. J. Chem. Phys., 109(7):2874–2882, 1998.

[73] H. Vázquez, Y.J. Dappe, J. Ortega, and F. Flores. A unified model for metal/organic interfaces: Idis, 'pillow' effect and molecular permanent dipoles. Appl. Surf. Sci., 254(1):378–382, 2007.

[74] L. Venkataraman, J.E. Klare, C. Nuckolls, M.S. Hybertsen, and M.L. Steigerwald. Dependence of single-molecule junction conductance on molecular conformation. Nature, 442:24, 2006.

[75] Christopher J Vineis, Ali Shakouri, Arun Majumdar, and Mercouri G Kanatzidis. Nanostructured thermoelectrics: big efficiency gains from small features. Advanced Materials, 22(36):3970–3980, 2010.

[76] W.R. Wadt and P.J. Hay. *Ab initio* effective core potentials for molecular calculations. potentials for main group elements na to bi. J. Chem. Phys., 82:284, 1985.

[77] J. R. Widawsky, W. Chen, H. Vazquez, T. Kim, R. Breslow, M. S. Hybertsen, and L. Venkataraman. Length-dependent thermopower of highly conducting au–c bonded single molecule junctions. Nano Lett., 13(6):2889–2894, 2013.

[78] Jonathan R. Widawsky, Pierre Darancet, Jeffrey B. Neaton, and Latha Venkataraman. Simultaneous determination of conductance and thermopower of single molecule junctions. Nano Lett., 12(1):354–358, 2012.

[79] Bernd Wölfing, Christian Kloc, Jens Teubner, and Ernst Bucher. High performance thermoelectric tl 9 bite 6 with an extremely low thermal conductivity. Physical review letters, 86(19):4350, 2001.

[80] Bingqian Xu and Nongjian J. Tao. Measurement of single-molecule resistance by repeated formation of molecular junctions. Science, 301(5637):1221–1223, 2003.

[81] Y. Xue, S. Datta, and M.A. Ratner. Charge transfer and band lineup in molecular electronic devices: A chemical and numerical interpretation. J. Chem. Phys., 115(9):4292–4299, 2001.

[82] Yongqiang Xue, Supriyo Datta, and Mark A. Ratner. First-principles based matrix green's function approach to molecular electronic devices: General formalism. Chem. Phys., 281(2-3):151–170, 2002.

[83] Yongqiang Xue and Mark A. Ratner. End group effect on electrical transport through individual molecules: A microscopic study. Phys. Rev. B, 69:085403, Feb 2004.

[84] XB Zhao, XH Ji, YH Zhang, TJ Zhu, JP Tu, and XB Zhang. Bismuth telluride nanotubes and the effects on the thermoelectric properties of nanotube-containing nanocomposites. Applied Physics Letters, 86(6):062111, 2005.